

Tribodynamic analysis of high-speed rolling element bearings in flexible multi-body environments

by
Harry Questa

Wolfson School of Mechanical, Electrical, and Manufacturing
Engineering
Loughborough University

A Doctoral Thesis submitted in partial fulfillment of the requirements for
the award of Doctor of Philosophy of Loughborough University

February 2024

Acknowledgements

I would like to sincerely thank my primary supervisor, Dr Mahdi Mohammadpour, for going above and beyond to provide guidance, support and encouragement throughout this project. His efforts and expertise have helped greatly to progress this work and my understanding of the technical aspects of this field. Thanks also go to my secondary supervisors, Professor Stephanos Theodossiades and Professor Colin Garner. Their technical expertise and guidance have ensured both depth and breadth to the final presented thesis.

I would also like to thank my industrial supervisors, Dr Stephen Bewsher and Dr. Günter Offner for their continued provision of technical expertise and guidance, as well providing access to the necessary resources to conduct this research. On a more personal level, I would like to also extend thanks to Martin Sopouch for facilitating and supporting my move to Austria to begin a full time position at AVL. Whilst this certainly introduced challenges regarding thesis completion, it has undoubtedly been the best decision of my life.

My final thanks go to family and friends for their continued support throughout this endeavour. Thank you to those that have encouraged me to complete this work despite the new and sometimes exciting challenges that have arisen throughout the PhD. There is a life outside of work and study; I am grateful to those that have reminded me of this.

This thesis has been a constant when most of my life has changed quite dramatically over the past few years. Perhaps I will miss it. Perhaps not.

Abstract

Roller bearings are critical components in hybrid and electric vehicle powertrains. They are often performance limiting, and introduce NVH (Noise, Vibration and Harshness), tribological and wear challenges. The high-speed and varying load conditions of modern electric powertrains necessitates accurate modelling of the bearings to ensure satisfactory system performance and durability. Furthermore, with a push towards achieving zero-prototype development, the use of advanced simulation tools to accurately predict their behaviour at both component and system level is becoming more prevalent.

Roller bearings are critical components of these motors. Current dynamic analyses that assume dry contacts are not valid in high-speed applications due to the role of elastohydrodynamic (EHL) lubricant film. Under light load and high speed, the EHL contacts of these bearings change their tribological behaviour, affecting parameters such as thermal performance, wear, sub-surface stress and frictional power loss. Hence, a combination of dynamics and contact mechanics is required for accurate performance and durability modelling. Furthermore, dynamic analyses that assume rigid bearing races do not accurately capture contact conditions between the roller and race, limiting the accuracy of the models in predicting the above parameters. There is a paucity of experimental or numerical tribo-dynamic work for predicting high-speed bearing behaviour.

Table of contents

List of figures	xi
List of tables	xiii
Nomenclature	xiv
List of Abbreviations	xix
Publications	xxi
1 Introduction	1
1.1 Numerical EHL Model	3
1.1.1 Numerical EHL Model	3
1.1.2 Finite Difference Formulation	5
2 Literature Review	7
2.0.1 Quasi-static Bearing Models	7
2.0.2 Contact Load and Deflection Calculation	8
2.0.3 Dynamic Bearing Models	10
2.0.4 Lubricated Dynamic Bearing Models	10
3 Investigating the Effect of Lubrication on the Tribodynamic Behaviour of High-Speed Roller Bearings	13
3.1 Overall Workflow	13
3.1.1 Experimental Test Rig	17
3.1.2 Instrumentation	17
3.1.3 Signal Processing	18
3.1.4 Contact Mechanics at the Roller Race Conjunction	20
3.1.5 Implicit Tribological Model	22
3.1.6 Friction Calculations	23
3.2 Numerical EHL Model	25

3.2.1	Reynold's Equation	25
3.2.2	Finite Difference Formulation	28
3.2.3	Effect of pressure on lubricant viscosity	29
3.2.4	Effect of pressure on lubricant density	30
3.2.5	Effect of temperature on viscosity	30
3.2.6	1D EHL Solution Methodology	31
3.2.7	Numerical EHL Model Validation	33
3.2.8	Experimental Result Verification	33
3.3	Results and Discussion	36
3.3.1	Film thickness and load across speed sweep	37
3.3.2	Friction	38
3.3.3	EHL Regimes	38
3.3.4	Dry vs Lubricated Tribodynamic Model	39
3.3.5	Numerical EHL Results	41
3.4	Conclusions	43
4	Modelling Lubricated Bearings in a Flexible Multi-Body Dynamic Environment	47
4.1	Preface	47
4.2	Introduction	48
4.3	Methodology	50
4.4	System Level Flexible Model	50
4.4.1	Lubricated Component Level Model	54
4.4.2	Representative Excitation Methodology	59
4.5	Results and Discussion	60
4.5.1	Conclusions	67
5	Artificial Neural Networks for EHL Film Thickness Predictions	69
5.1	Abstract	69
5.2	Introduction	70
5.3	Artificial Neural Network Fundamentals	72
5.3.1	Numerical EHL Methodology	73
5.3.2	Artificial Neural Network Methodology	73
5.3.3	ANN Training Process	73
5.4	Machine Learning Methodologies	76
5.5	Results and Discussion	83
5.6	Conclusions	88
5.7	Conclusions	88

6 Implicit Bearing EHL Film Thickness Predictions Using an Artificial Neural Network at System Level	91
7 Conclusions	93
References	95
Appendix A MFEIT Reconstruction Images	107

List of figures

1.1	Global Car Sales by Fuel Source Through 2030.	2
3.1	Methodology Overview.	14
3.2	Cylindrical roller bearing in equilibrium position.	15
3.3	Mutual separation and convergence of inner and outer races.	16
3.4	EHL film thickness and pressure distribution at contact.	17
3.5	Experimental rig schematic.	18
3.6	Accelerometer locations on test bracket.	19
3.7	Laser vibrometer locations on shaft.	19
3.8	Validation of dimensionless pressure distribution, present model (solid), Masjedi and Khonsari (dashed).	33
3.9	Validation of dimensionless film thickness distribution, present model (solid), Masjedi and Khonsari (dashed)	34
3.10	Bearing bore displacement frequency spectra.	36
3.11	Shaft displacement frequency spectra.	36
3.12	Contact load and film thickness - Outer race.	37
3.13	Film and load - EHL to hydrodynamic regime.	38
3.14	Viscous and boundary friction at the outer race contact.	39
3.15	EHL and hydrodynamic conditions during roller operation. Key: IR = Iso-viscous Rigid, VR = Viscous Rigid, VE = Viscous Elastic, IE = Iso-viscous Elastic.	40
3.16	Contact load difference between dry and lubricated model.	41
3.17	Dry and lubricated model load difference: a) 3 050 rpm, b) 14 135 rpm, c) 14 855 rpm.	42
3.18	Selected points for the numerical EHL model.	43
3.19	EHL pressure and film thickness distributions: a) Node 1, b) Node 2, c) Node 3, d) Node 4, e) Node 5, f) Node 6	44
4.1	Flowchart of models.	51

4.2	System level model schematic.	52
4.3	Bearing schematic.	54
4.4	Dry vs lubricated roller-race contact.	55
4.5	Contact level validation.	57
4.6	PMSM torque profile and maximum and minimum torque fluctuation. .	60
4.7	Rolling element contact stiffness - Dry vs lubricated maximum values. .	62
4.8	Rolling element contact force - Dry vs lubricated percentage increase. .	63
4.9	Inner race stiffness - Dry vs lubricated operating envelope.	64
4.10	Inner race displacement - Dry vs lubricated operating envelope.	64
4.11	Inner race acceleration - Dry vs lubricated operating envelope.	65
4.12	Rolling element contact stiffness - Dry vs lubricated minimum values. .	65
4.13	Film thickness vs contact force 21 000 rpm.	66
4.14	Film thickness vs contact force 12 500 rpm.	66
5.1	Greenwood informed training data vs Marian et al. [1].	78
5.2	Individual rolling element input values to ANN : a) Contact load, b) Contact entrainment velocity, c) Contact reduced radius	84
5.3	10 – [14 – 14 – 14]3 – 1 using Hyperbolic Tangent activation function : a) 600 points, b) 1000 points, c) 2000 points, d) 5000 points	87
5.4	ANN, numerical and analytical central film thickness comparisons.	88

List of tables

3.1	Surface Topography Data	25
3.2	Bearing Specification	34
3.3	Lubricant and Material Properties	35
3.4	Extrapolated film formulae and numerical model central film thickness comparison	44
4.1	Cylindrical Roller Bearing Specification	59
4.2	Bearing Rheological Properties	59
4.3	Pinion Geometry	61
4.4	Gear Geometry	61
5.1	Range of ANN film thickness calculation parameters	79
5.2	Roller Bearing Parameters	82
5.3	Operating Conditions	82
5.4	R^2 performance of ANN structures using 600 data points and a LogSig activation function	85
5.5	R^2 performance of ANN structures using 600 data points and a Tanh activation function	85
5.6	R^2 performance of ANN structures using 600 data points and a Tanh activation function	85
5.7	Training time of ANN structures with LogSig activation function and 600 data points	86
5.8	Training time of ANN structures with LogSig activation function and 1000 data points	86
5.9	Training time of ANN structures with LogSig activation function and 2000 data points	86
5.10	Training time of ANN structures with LogSig activation function and 5000 data points	86

Nomenclature

A	Jacobian matrix AND Cross-sectional area
A^\dagger	Pseudo-inverse Jacobian matrix
B	Susceptance
\mathbf{B}	Magnetic Flux
C	Capacitance
C_m	Measured capacitance
c	Specific capacitance
c^*	Complex permittivity
\mathbf{D}	Electric displacement
\mathbf{E}	Electric field
E_l	The area in contact with electrode l on $\partial\Omega$
\mathbf{H}	Magnetic field strength
f_{nj}	Weighting value for tissue at j th element at FEM node n
G	Conductance
G_m	Measured conductance
H^1	A Hilbert space
\mathbf{I} I	Current
\mathbf{I}_l	Current at electrode l
i	The imaginary number AND Frequency index
\mathbf{J}	Electric current density
\mathbf{J}_c	Conduction current density
\mathbf{J}_s	Source current density
j	Boundary current density AND Tissue index
K	Magnitude of the wavenumber vector

L	Total number of electrodes AND Lead inductance
l	Electrode numeration AND Negative log-likelihood AND Length AND Electrode channel
N	Number of current sources AND Number of measurements
n	FEM node element index
\mathbf{n}	The unit vector of the normal to surface $\partial\Omega$
R	Resistance
r	Correlation coefficient
S	A surface
T	Total number of tissues
t	Time
t_j	Tissue number at j
V	Voltage
V_l	Voltage at electrode l
V_{fi}	Voltage at frequency i
$V_{f_{ref}}$	Voltage at the reference frequency
v	A set of test functions
X	Reactance
\mathbf{Y}	Admittance
Z	Impedance
z	Impedivity
z_l	Contact impedance between electrode l and the tissue on E_l
β	Susceptivity
Γ	Total boundary of $\partial\Omega$ that is in contact with an electrode
Γ'	$\partial\Omega$ not in contact with an electrode
γ	Admittivity
γ_l	Boundary admittivity on E_l
δ	Loss angle
$\partial\Omega$	The surface area of volume Ω
ϵ	Electrical permittivity
ϵ_r	Relative permittivity

ϵ_0	Permittivity of free space
ϵ'	Real permittivity
ϵ''	Imaginary permittivity
ϵ_r''	Out of phase loss factor
Λ	Forward transformation map
λ	Characteristic spatial wavelength
μ	Magnetic permittivity
ρ'	Real resistivity
ρ''	Imaginary resistivity
ρ	Resistivity
σ σ	Electrical Conductivity
σ_{ij}	Conductivity of tissue j at frequency i
σ_n	Conductivity of tissue at FEM node n
σ^{tj}	Conductivity of tissue at j th element
τ	Regularisation parameter
ϕ	Scalar electric potential
Ψ	Regularising function
Ω	A volume
ω	Angular frequency
ω_i	Angular frequency at i th element
ΔT	Temperature difference
ΔV	Voltage difference
ΔV_{FD_i}	Frequency difference voltage at frequency i with respect to the reference frequency
ΔV_{FDA_i}	Frequency difference voltage at frequency i with respect to frequency $i - 1$
ΔV_{WFDA_i}	Weighted frequency difference adjacent voltage at frequency i with respect to frequency $i - 1$
$\Delta\sigma$	Conductivity difference
$\tan \delta$	Dissipation factor

List of Abbreviations

ADC	Analogue to Digital Converter
ACT	Adaptive Current Tomography
APT	Applied Potential Tomography
CEM	Complete Electrode Model
CSF	Cerebrospinal Fluid
CT	Computerised Tomography
DAC	Digital to Analogue Converter
DDS	Direct Digital Synthesis
EEG	Electroencephalogram
ECG	Electrocardiogram
EIT	Electrical impedance Tomography
FA	Full Array Electrode Configuration
FDA	Frequency Difference Algorithm
FEM	Finite Element Method
GREIT	Graz Reconstruction Algorithm for Electrical Impedance Tomography
SA	Semi-Array Electrode Configuration
HA	Hemi-Array Electrode Configuration
HCT	Haematocrit
LHS	Left Hand Side
MFEIT	Multifrequency Electrical Impedance Tomography
MRI	Magnetic Resonance Imaging
PTD	Percentage Thickness Dipolë

RHS	Right Hand Side
SA	Semi-Array Electrode Configuration
SNR	Signal to Noise Ratio
WFD	Weighted Frequency Difference
WFDA	Weighted Frequency Difference Adjacent
VGA	Variable Gain Amplifier

Publications

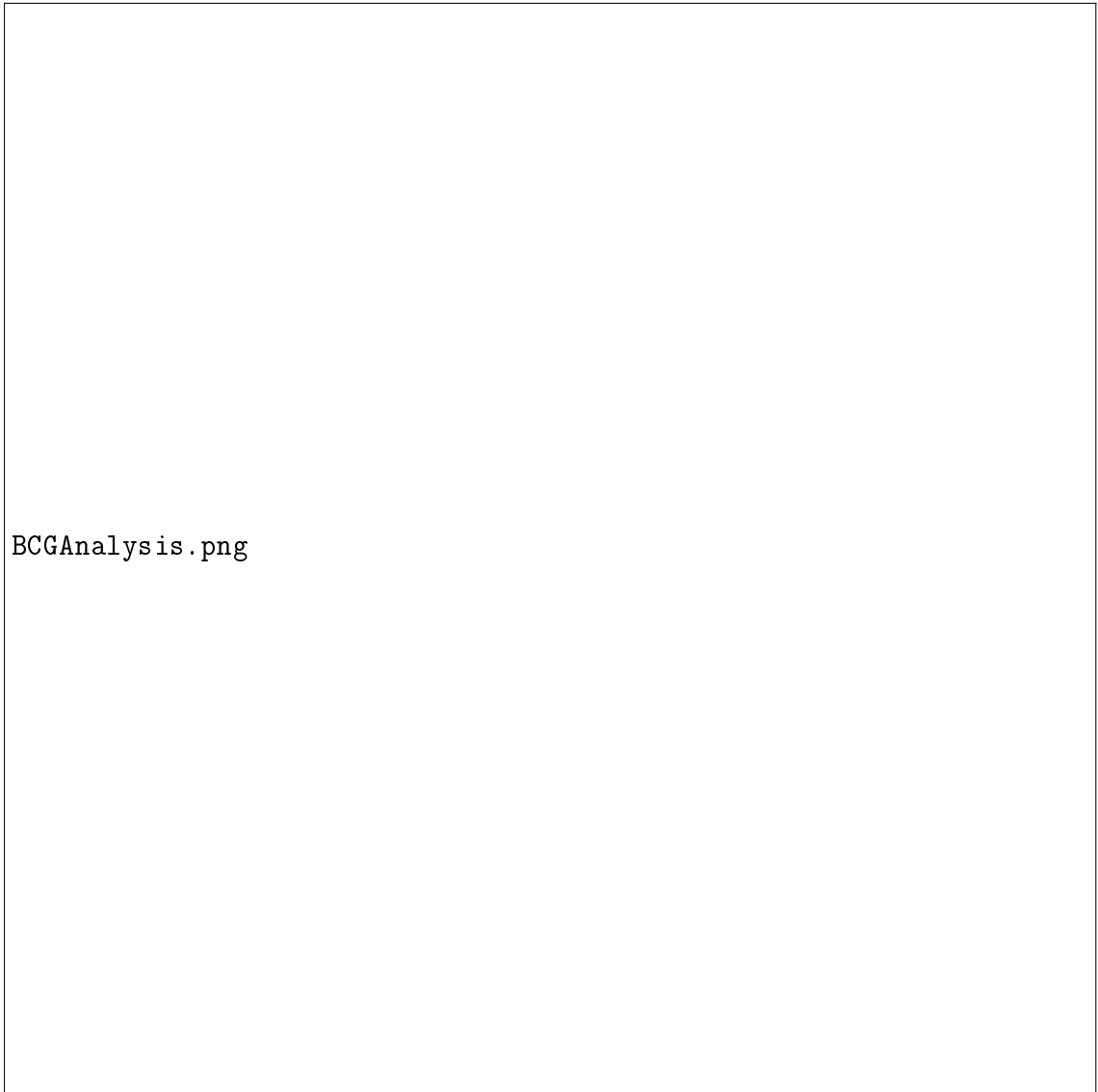
The results of this thesis are partially summarised in the following paper:

- (i) Williams, T., Bouazza-Marouf, K., Zecca, M., and Green, A.L., *Analysis of the validity of the mathematical assumptions of electrical impedance tomography for human head tissues*, Biomed. Phys. Eng. Express **7**, 025011 (2021).

Chapter 1

Introduction

The automotive industry is currently transitioning into the next phase of powertrain technology. As automotive manufacturers are forced to meet tightening fleet-wide emissions regulations, the electrified vehicle market share will increase. Early adoption barriers will begin to reduce as non-ICE (internal combustion engine) vehicle sales are incentivised. Coupled with improvements in technology and a shift in customer attitudes, electric and hybrid electric vehicles are estimated to have a global market share of 48% by 2030 [2].



BCGAnalysis.png

Figure 1.1 Global Car Sales by Fuel Source Through 2030.

The use of ultra-high speed and low load motors introduces new challenges regarding NVH (Noise, Vibration and Harshness) and the tribology of interacting conjunctions. The compact, lightweight and efficient motors operate under significantly different working conditions and are subject to different underlying physics; such as regime of lubrication, dynamic response and magneto-mechanical interactions. This style of powertrain architecture therefore involves high-speed bearing operation in both the motor and transmission.

With a trend towards cost saving zero-prototype development, the use of simulation tools in modern powertrain development is also growing. Significant cost reductions can be achieved using commercial flexible multi-body dynamic solvers to replicate system level operation of these vehicles. Multi-system vehicle powertrain concepts

are pushing complexity of simulation models and this requires accurate and robust component level understanding. Associated performance characteristics of the bearings such as friction and wear, thermal stability and generated vibration and noise must be accurately modelled at the development stage to ensure full system success [3].

1.1 Numerical EHL Model

1.1.1 Numerical EHL Model

Reynold's equation [4] is the governing equation of fluid film lubrication theory. For Newtonian fluids it can be derived from the full Navier-Stokes equations making the following assumptions, primarily the neglection of inertial forces and only retaining viscous forces on the lubricant [5]:

1. Body forces are negligible (mass of film is negligible)
2. Pressure is constant through the lubricant film (z -direction) due to thin film (dimensions of the region of pressure are typically 100 times the central film thickness).
3. No slip at boundaries
4. Lubricant flow is laminar (low Reynolds number)
5. Inertia and surface tension forces are negligible compared with viscous forces (working fluid has low mass and low acceleration)
6. Shear stress and velocity gradients are only significant across the lubricant film
7. The lubricant behaves as a Newtonian fluid
8. Lubricant viscosity in constant across the film
9. The lubricant boundary surfaces are parallel or at a small angle with respect to each other

Reynolds equation is a second order, non-linear partial differential equation. It is made up of the pressure induced terms (Poiseuille flow) and the boundary velocity-induced term (Couette flow).

For the line contact problem, such as that at the conjunction between a cylindrical roller and race, dimensions in the side-leakage direction, y , are much bigger than the direction of entraining motion, x . Pressure in y direction is assumed constant due to the

negligible gradient, and the contact can be analysed in 1-dimension. The assumption is valid in the contact apart from small regions near the edge where the roller profile changes. A simplified 1-dimensional version of Reynolds equation can therefore be used:

$$\frac{\partial}{\partial x} \left[\frac{\rho h^3}{6\eta} \left(\frac{\partial p}{\partial x} \right) - \rho h u \right] = 2 \frac{\partial(\rho h)}{\partial t} \quad (1.1)$$

To solve Reynolds equation numerically, it must first be discretized and then solved using the finite-difference method. The following procedure explains this discretization.

Due to the steady state nature of the investigations, with the absence of shock loading, the transient squeeze term can be removed:

$$\frac{\partial}{\partial x} \left[\frac{\rho h^3}{6\eta} \left(\frac{\partial p}{\partial x} \right) - \rho h u \right] = 0 \quad (1.2)$$

Due to the many orders of magnitude differences between lubricant film thickness (μm) and pressures (GPa), the numerical solution often becomes unstable. Dimensionless parameters are therefore defined to remove this instability. These are as follows:

$$\begin{aligned} U &= \frac{u}{u_{av}} & \partial x &= a \partial X \\ X &= \frac{x}{a} & \partial \rho &= \rho_0 \partial \bar{\rho} \\ \bar{\rho} &= \frac{\rho}{\rho_0} & \partial \eta &= \eta_0 \partial \bar{\eta} \\ \bar{\eta} &= \frac{\eta}{\eta_0} & \partial h &= \frac{a^2}{R_{zx}} \partial H \\ H &= \frac{h R_x}{a^2} & \partial p &= p_h \partial P \\ P &= \frac{p}{p_h} \\ W^* &= \frac{w}{E_r R_{zx} L} \end{aligned} \quad (1.3)$$

Terms in the simplified Reynolds equation are replaced with dimensionless parameters. Similar terms are then grouped and rearranged to give the final form:

$$\frac{\partial}{\partial X} \left[\frac{\bar{\rho} H^3}{6\bar{\eta}} \left(\frac{\partial P}{\partial X} \right) \right] = \Psi \left[\frac{\partial}{\partial X} \bar{\rho} H U \right] \quad (1.4)$$

where

$$\Psi = \frac{12 u_{av} R_{zx}^2 \eta_0}{p_h} \quad (1.5)$$

Grouping terms for simplicity

$$M = \frac{\bar{\rho}H^3}{6\bar{\eta}} \quad (1.6)$$

$$Q = \bar{\rho}H \quad (1.7)$$

Making substitutions

$$\frac{\partial}{\partial X} \left[M \left(\frac{\partial P}{\partial X} \right) \right] = \Psi \frac{\partial}{\partial X} [QU] \quad (1.8)$$

$$\left[M \frac{\partial^2 P}{\partial X^2} + \left(\frac{\partial M}{\partial X} \right) \frac{\partial P}{\partial X} \right] = \Psi \left[U \frac{\partial Q}{\partial X} + Q \frac{\partial U}{\partial X} \right] \quad (1.9)$$

The final term is removed, as velocity, U , is independent of x when no stretching of the surfaces occurs. This is then differentiated to give:

$$\frac{\partial M}{\partial X} = \frac{\partial}{\partial X} \left[\frac{\bar{\rho}H^3}{6\bar{\eta}} \right] = \frac{H^2}{2\bar{\eta}} \left[\left(\frac{H}{3} \right) \frac{\partial P}{\partial X} + \bar{\rho} \frac{\partial H}{\partial X} - \left(\frac{\bar{\rho}H}{2\bar{\eta}} \right) \frac{\partial \bar{\eta}}{\partial X} \right] \quad (1.10)$$

and

$$\frac{\partial Q}{\partial X} = \frac{\partial}{\partial X} [\bar{\rho}H] = H \frac{\partial \bar{\rho}}{\partial X} + \bar{\rho} \frac{\partial H}{\partial X} \quad (1.11)$$

Substituting into Equation 1.9 gives the following:

$$\frac{\bar{\rho}H^3}{6\bar{\eta}} \frac{\partial^2 P}{\partial X^2} + \frac{H^2}{2\bar{\eta}} \left[\frac{H}{3} \frac{\partial \bar{\rho}}{\partial X} + \bar{\rho} \frac{\partial H}{\partial X} - \frac{\bar{\rho}H}{2\bar{\eta}} \frac{\partial \bar{\eta}}{\partial X} \right] \frac{\partial P}{\partial X} - \Psi U \left[H \frac{\partial \bar{\rho}}{\partial X} + \bar{\rho} \frac{\partial H}{\partial X} \right] = 0 \quad (1.12)$$

$$\frac{\partial^2 P}{\partial X^2} + \frac{3}{\bar{\rho}H} \left[\frac{H}{3} \frac{\partial \bar{\rho}}{\partial X} + \bar{\rho} \frac{\partial H}{\partial X} - \frac{\bar{\rho}H}{2\bar{\eta}} \frac{\partial \bar{\eta}}{\partial X} \right] \frac{\partial P}{\partial X} - \frac{6\bar{\eta}}{\bar{\rho}H^3} \Psi U \left[H \frac{\partial \bar{\rho}}{\partial X} + \bar{\rho} \frac{\partial H}{\partial X} \right] = 0 \quad (1.13)$$

The final form of the equation is therefore:

$$\frac{\partial^2 P}{\partial X^2} + \left[\frac{1}{\bar{\rho}} \frac{\partial \bar{\rho}}{\partial X} + \frac{3}{H} \frac{\partial H}{\partial X} - \frac{3}{2\bar{\eta}} \frac{\partial \bar{\eta}}{\partial X} \right] \frac{\partial P}{\partial X} - \frac{6\bar{\eta}}{H^2} \left[\frac{1}{\bar{\rho}} \frac{\partial \bar{\rho}}{\partial X} + \frac{1}{H} \frac{\partial H}{\partial X} \right] \Psi U = 0 \quad (1.14)$$

1.1.2 Finite Difference Formulation

For finite difference formulation, the central difference formula based on Taylor series expansion [6] is used. The second derivative of pressure using second order central discretization for the spatial domain is therefore:

Chapter 2

Literature Review

To model the behaviour of rolling element bearings under conditions in electrified powertrains, component level models are required. At the core of these models is the dynamic bearing model.

Prior to the 1960's, bearing studies were primarily conducted experimentally. Empirical formulations were derived to model their performance in early work by Stribeck [7] and Lundberg and Palmgren [8] [9] amongst others. As computer technology improved post-1960, modelling theory and application grew rapidly, pioneered largely by the work of Jones [10] and Harris [11]. In the pursuit of highly efficient and reliable bearings, modelling and the need for accurate representation of the physical phenomena has become important. It is not possible to conduct experimental testing for the large array of design and operational parameters that bearings are required for, therefore experimentally validated numerical analysis is employed.

2.0.1 Quasi-static Bearing Models

Early models predicting load distribution in the rolling elements can calculate bearing stiffness and fatigue life with relative accuracy. These were primarily quasi-static and based on force equilibrium. Studies of static ball bearings under simple radial loading were performed by Stribeck [7] and improved upon by Palmgren [9] for the case of nominal internal clearance. Static models computing radial and axial loads based on a load distribution factor and the angular position of the roller were found using Sjovall's integration model [12], however this was only applicable if the ratio of radial to axial loads is within a particular range. Rumbarger [13] developed a model using Sjovall's integral method for purely axial loading of thrust bearings, capable of calculating moment load due to axial load eccentricity.

It was the work of Jones [10] and his general theory for load deflection analysis of bearings that extended the capability of these models. His work accounted for centrifugal and gyroscopic loading, and unlike previous models, the inner bearing race had 5 degrees of freedom (DOFs); three translational and two rotational displacements that correspond to the external forces in all three cartesian coordinates and moments applied about two. Bearing equilibrium is obtained at each rolling element by observing the load and corresponding motion of the elements. Jones also included the individual stiffness at the contact between rolling elements and raceways, using the Hertzian contact load-deflection relationship to obtain roller load based on contact deflection. This technique could be applied to both ball and roller bearings by varying the exponent of localised deflection.

Jones' model was considered limited due to the assumption that misalignment effects on the elements are negligible. Harris [11] improved on it by introducing the slicing method along the length of the rollers. This enabled determination of the load distribution along the contact in roller bearings. This method, known as the Jones-Harris method, was then applicable for highly loaded conditions and able to compute misaligned cases. Vector and matrix methods to analytically solve the quasi-static problem based on the work of Jones and Harris were then presented for tapered roller bearing cases by Andréason [14] and Liu [15]. de Mul et al. [16] developed a model for ball and roller bearing equilibrium and stiffness matrix calculations which has the advantage of having load-deflection equations in matrix form, therefore implementation of this model is simpler.

Additional functionality has been added to these models such as the effects of thermal expansion on the load-deflection analysis [17]. Numerical models for heat generation based on frictional torque and 3-dimensional transfer through contacting elements was used to account for the expansion. It was found that expansion increased the bearing stiffness and thus natural frequency of the shaft-spindle system due to greater interference of the roller race contact. The authors also investigated the effect of ring expansion due to centrifugal force at high speeds [18] and found that natural frequency of the spindle decreased at higher rotational speeds – of particular note for high speed automotive applications.

2.0.2 Contact Load and Deflection Calculation

The contact between rolling elements and raceways and the subsequent load and deformation generated at this contact is regarded as one of the most important issues in rolling-element bearing modelling. For a ball bearing, classical Hertzian theory is

used to calculate the load-deformation relationship. However, the line contact is more complex.

There exist three methods to determine this relationship for the line contact in roller bearings: the slicing technique, 3D contact method and the alternative slicing technique. The slicing technique [14] divides the roller-race contact region into a finite number of slices, with the total contact forces calculated from the summation of forces of each individual slice. Various formulae have been developed to perform this calculation, all yielding very similar results. A drawback of this method is that the load on each slice does not influence the surrounding slices as they are treated independently. This means that pressure concentrations such as edge stresses on the contact are not captured. The 3D contact method uses the Boussinesq half-space force-displacement relationships and flexibility method of structural analysis. The contact pressure distribution and normal approach between the bodies is found using an iterative scheme, making this a time-consuming method. Kabus et al. [19] addressed this in their 6-dof quasi-static time-domain bearing model by pre-processing a series of contacts at different centreline approaches and roller tilt angles, then interpolating these results in the actual simulations. This negated the need to solve the iterative scheme at each time step. This allowed for bearing misalignment, roller centrifugal forces, flange contact and roller tilt moments to be analysed.

Teutsch and Sauer [20] improved on the slicing technique with their alternative slicing method. Using a matrix of weighted influence coefficients, the effects of force on the deflection of neighbouring slices was captured. It is not too dissimilar in concept to the 3D contact method but with improved computation times. de Mul et al. [16] compared the slicing technique with their more complex non-Hertzian model and concluded that the simplicity and accuracy of the slicing method yielded accurate and faster results. Harris and Kotzalas [21] also concluded that the slicing technique, whilst unable to reflect edge stress concentrations, provides a suitably accurate load-displacement result as stresses are only distributed over a small area. For the purpose of load equilibrium, these stresses can be neglected. Misalignment or loading on roller ends is not captured using this technique, therefore for fatigue life estimates this may produce non-conservative results; for this, the approach by Kabus et al. should be used. In general, the slicing technique is the most widely used, owing to its simplicity, speed, and sufficient accuracy.

2.0.3 Dynamic Bearing Models

Quasi-static bearing models that solve force equilibrium within the bearing are only applicable under steady state operating conditions. Transient operating conditions such as acceleration or deceleration of the bearing requires dynamic modelling, particularly important for high-speed applications. In dynamic bearing models, a system of differential equations based on Newton's second law of motion are used. This allows for a time-varying input force such as eccentric rotor unbalances or fluctuating loading conditions present in transmissions. Static equilibrium solutions such as those presented are used within these models to calculate load-deflection and individual element loading.

Hitherto, a multitude of models predicting bearing dynamics have been posed for roller bearings. These investigate the dynamic effect of geometrical and topographical parameters such as surface waviness, surface defects, and the variable compliance affect. This variable compliance effect is caused by time-varying stiffness variations off the inner and outer race bearing contact as rollers change their orbital position and pass through the loaded region. Even with perfect bearing geometry free from any defects, vibration will still occur due to this [61].

Simplified 2 degree of freedom models [52] consider purely in-plane motion of rolling elements in the radial and lateral directions of the bearings for investigation of frequency response to defects [?] and the varying compliance effect [53]. Time varying forces on cutting tool spindles and the effects on radial loading assuming no axial thrust loads or vibration can also be investigated in 2 DOF [23]. These models increase in complexity up to 5-DOF to observe moment loading and centrifugal effects [54] [30]. Most of these models assume the bearing rollers and races are rigid bodies. All these analyses also assume a dry contact between rolling elements and races which was assumed valid under the elastohydrodynamic regime of lubrication. The fluid film behaves as an amorphous, incompressible solid and generated pressures conform closely to a Hertzian distribution in the loaded region. This, however, neglects the effect of the lubricant film thickness in the contact mechanics and thus underestimates the contact deflection and hence load. Furthermore, the assumption of rigid rollers and races which is widely used amongst bearing dynamic models to simplify the computation is often not representative of the physical phenomena of modern shaft-bearing systems.

2.0.4 Lubricated Dynamic Bearing Models

To fully numerically analyse a complement of rolling elements at each step of dynamic analysis, accounting for lubricant film thickness at the contact, is a time-consuming limitation. Historically the analysis of rolling element bearings has been decoupled

into two stages. The first stage is a classic dry Hertzian-contact analysis of the roller-raceway contact due to the cyclic variation in geometric bearing centre [?]. The displacement of the bearing centre is obtained through solving equations of motion and roller load is obtained using the Hertzian load-deflection relationship. Extrapolated film thickness equations use the transient load yielded from dry analysis in a second stage study to find central film thickness. This approach does not implicitly consider the effect of the lubricant film on the prevailing bearing motion and load, which is hence underestimated. To overcome these shortcomings, quasi-static analyses employing film thickness formulae in conjunction with Hertzian contact mechanics are required.

Rahnejat and Gohar [59] employed these formulae to account for film thickness on the load share of an individual roller within the bearing complement. This coupled a two-dimensional dynamic model for a radial deep groove ball bearing with extrapolated film formulae implicitly. More reasonable bearing vibration amplitudes resulted than de-coupled analyses which were only suitable for spectral contributions and unable to produce accurate magnitudes. This work was later extended to a 5-dof model by Aini et al. [60] which included axial thrust effects and moment loading in a shaft-bearing system. The analytical film thickness formulae used do not offer the capabilities of a full numerical solution such as the modelling of inlet starvation at high speeds. They do, however, offer a much faster solution when implicitly coupled with dynamic bearing analysis.

Film shape and the elastohydrodynamic pressure profile at the contact could not be calculated in these studies, preventing more detailed analysis such as thermal and sub-surface stress analysis. To determine tribological contact conditions, Mohammadpour et al. [28] utilised a full numerical elastohydrodynamic analysis explicitly. Load values on an individual roller at each instantaneous position of the orbit were obtained from the implicit tribodynamic analysis and used within the numerical model. The stiffness and damping of the EHL film is neglected due to its rigid-like stiffness which is several orders of magnitude higher than the Hertzian contact [31] [32].

These lubricated dynamic models were performed for low shaft rotational speed. In Mohammadpour's analysis, input shaft speeds of 209 rad/s resulted in much slower entrainment velocities than in EV case studies. The rollers and races were also considered rigid in these investigations. Thus far, tribo-dynamic models have not been found that model the bearing races as flexible bodies or at high speeds.

Chapter 3

Investigating the Effect of Lubrication on the Tribodynamic Behaviour of High-Speed Roller Bearings

Prior to the development of the 6 DOF dynamic model, a high-speed experimental test rig was instrumented to obtain boundary conditions for subsequent tribological models. This work was performed to ascertain what type of models need to be developed in the tribology domain without the need for a dynamic model. The requirement for lubricated rather than dry contact models, regimes of lubrication and workflows such as implicit or explicit modelling have been investigated.

3.1 Overall Workflow

To obtain the film thickness at the roller-race contact, the load on each roller must be calculated implicitly based on the contact deflection. This is obtained conventionally from a dynamic model by solving the equations of motion, but these are currently lacking the required in-depth physics such as system flexibility, flexibility of races and thermal effects [22] [23] [24] [25].

To circumvent the need for a complex flexible dynamic model and to capture real behaviour of a bearing under test, displacement of the bearing centre and hence contact deflection is captured from experimental test results.

An experimental test rig is used to obtain the relative displacement between the inner and outer bearing races. Then, using the Hertzian load-deflection relationship and accounting for the lubricant film thickness, load on an individual roller is found at each instantaneous position around the bearing centre through a speed sweep of

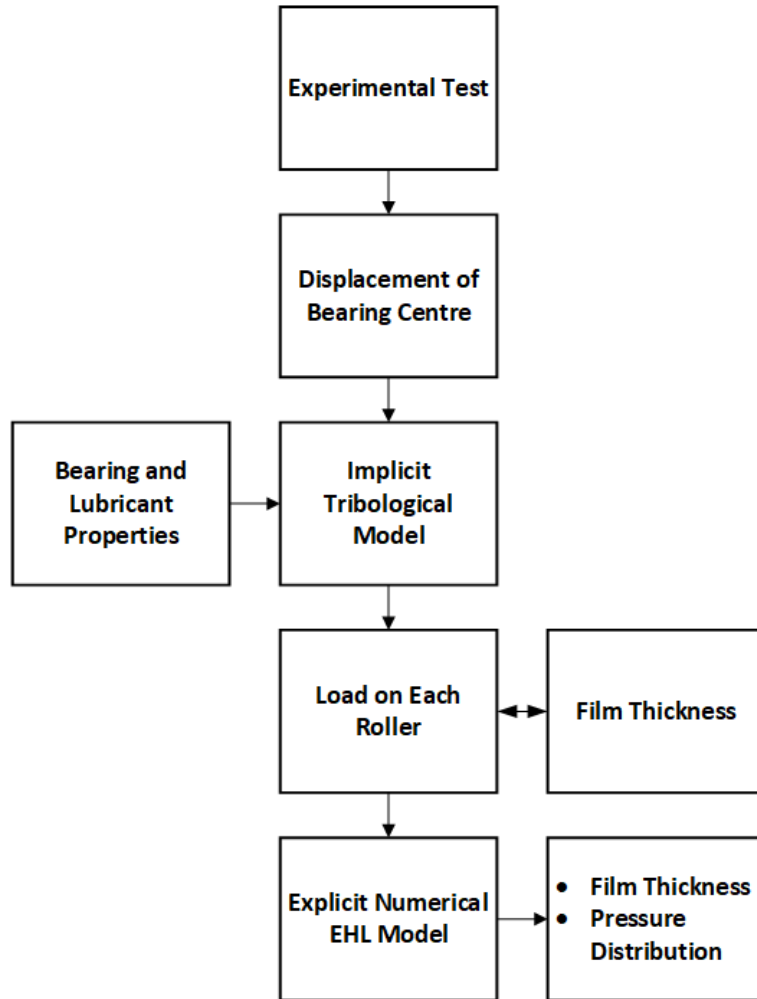


Figure 3.1 Methodology Overview.

0 – 15 000 rpm. An implicit analytical tribological model is used which calculates the film thickness at the contact. This loop is iterated to account for the tribodynamic coupling. After the experimentally informed implicit tribodynamic model is solved, load and speed values at specific rotational velocities are used within an explicit numerical EHL model to calculate film thickness and pressure distribution across the contact. The flow diagram in 3.1 illustrates the methodology used. Interactions between each stage will be explained in subsequent sections.

The rollers within a bearing carry an instantaneous share of the overall applied load [26]. Deviation of the supported shaft centre from its nominal geometric centre results in a loaded region of the bearing. In the conjunction between the bearing roller and race, the non-conformal nature of contact generates very high pressures when under load. This causes local surface deformation and an increase in lubricant viscosity, resulting in EHL film formation [5] [27]. Emerging clearances in unloaded regions of the bearing results, which can cause the roller-to-race contact to deviate from the EHL regime towards

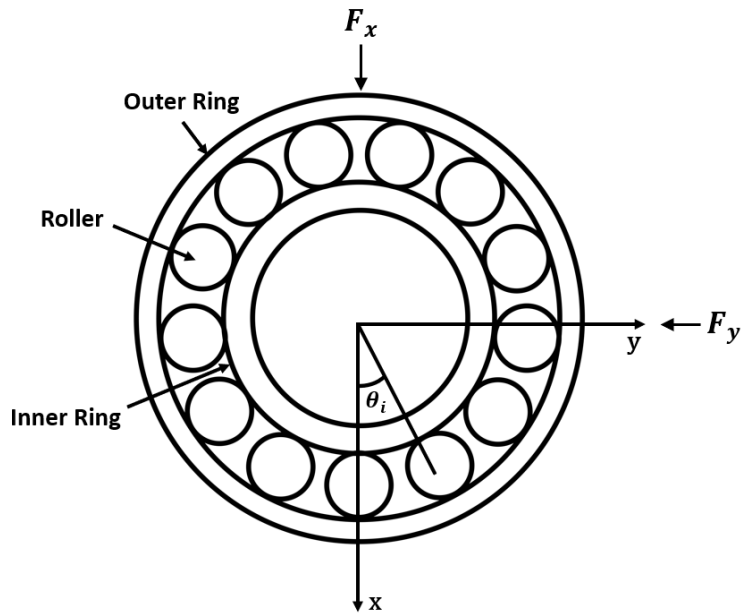


Figure 3.2 Cylindrical roller bearing in equilibrium position.

the hydrodynamic regime, result in sliding and roller-cage collisions [28]. Hence, the contact may go through different regimes of lubrication throughout its rotation [29].

Figure 3.2 shows the cylindrical roller bearing (CRB) in equilibrium position with zero preload or design clearance. Under zero applied radial load, F_0 , the initial deformation, δ_o , and radial clearance, C_0 , between rollers and races are both zero. Due to external force application and system dynamics, an instantaneous radial load, F , will displace the inner bearing race from its equilibrium state (Δx and Δy). By analysing an individual roller at its instantaneous angular position, θ_i , the resultant displacement of the bearing centre can be used to find deflection at the roller-race contact, δ_i . These contact deformations will result in contact forces, W_i , which act to keep the rollers and races in dynamic equilibrium. The above interpretation is valid considering rigid inner and outer races.

Figure 3.3 presents the case whereby an instantaneous force is applied to the inner race. This causes deflection of the rollers in the loaded region and clearance around the rollers in the unloaded region. The value of the total deflection, δ_i at the inner and outer race corresponds to the component of displacement of the bearing centre at the instantaneous position of that particular roller. In the current study, this value was experimentally measured from the test rig and is used quasi-statically as the boundary condition for the tribological model. It should be noted that in-plane two degrees of freedom motion are analysed in this study which is a valid assumption under dominant radial loading with secondary horizontal motion from the full system dynamics. Misalignment along the

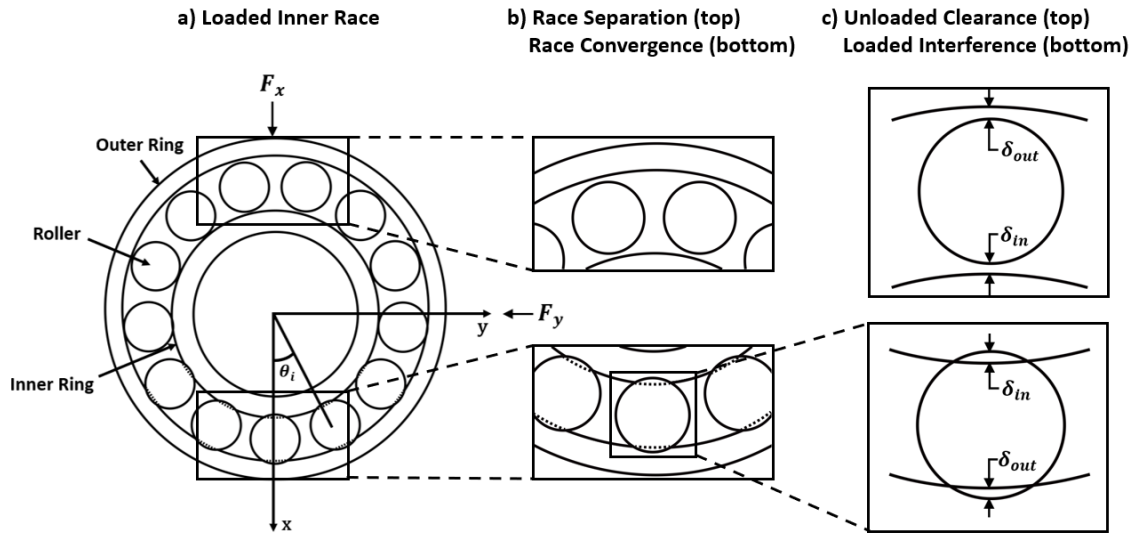


Figure 3.3 Mutual separation and convergence of inner and outer races.

length of the rollers is not considered due to the high stiffness of the shaft and bracket, hence a 1-dimensional analysis for EHL is sufficient [30].

In the loaded region, the Hertzian load-deflection relationship is used to obtain the resulting instantaneous load on the roller. This value is then used implicitly within an analytical tribological model to calculate contact film thickness for an individual roller as it passes through different angular positions during a speed sweep. An extrapolated film thickness formula is used for this purpose. The calculated film thickness imposes additional deformation at the contact points which itself changes the calculated load. Hence, an iterative approach is required between the force calculation and implicit tribological model. In this part of the workflow, the stiffness and damping of the EHL film is neglected due to its rigid-like stiffness, which is several orders of magnitude higher than the Hertzian contact [31] [32] !!!USE LATEST REFERENCES FROM TRIBODYNAMIC PAPER.

For in-depth tribological investigations, the numerical solution of the fluid film is essential. This provides the pressure, film thickness and shear distributions in the contact to study the durability and frictional efficiency of the system. In the current study, the load on the roller and contact kinematics obtained from the implicit bearing model is used explicitly in a 1-dimensional elastohydrodynamic model to obtain film thickness and pressure distribution at the contact for specific loading periods through the speed sweep, as is shown in Figure 3.4. This explicit approach significantly improves the computational efficiency of the model and in principle, maintains the accuracy since only the central value of the film is required in the load calculation.

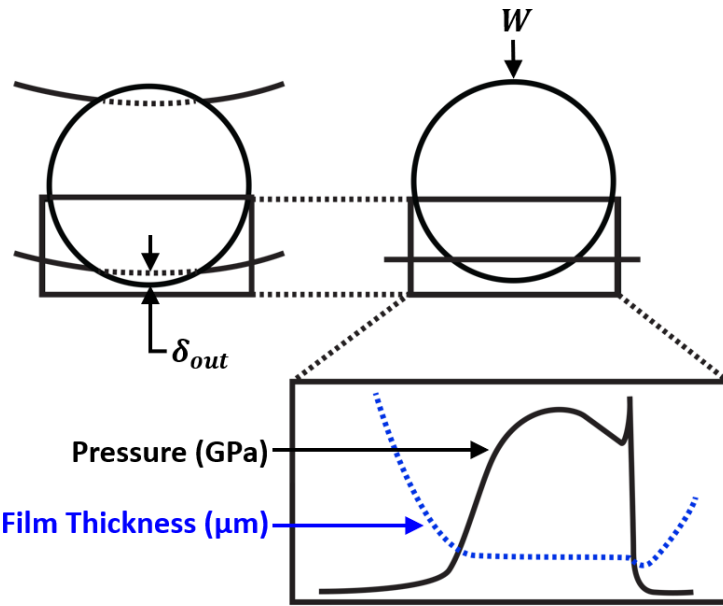


Figure 3.4 EHL film thickness and pressure distribution at contact.

3.1.1 Experimental Test Rig

The displacement of the bearing centre governs the conditions at the contact and was found experimentally using a high-speed bearing test rig, originally reported by Walker et al. [33]. A 5 kW AC synchronous motor, capable of speeds up to 32 000 rpm was coupled to a steel shaft that is supported by two bearing brackets. Radial force was transferred to inner bearing race via the shaft using a hinge/arm mechanism and a load application device on the shaft. Displacement data were obtained from an instrumented bearing bracket. Figure 3.5 shows a schematic of the rig.

The motor control unit was connected to a voltage input, transmitted via an NI cDAQ-9178 USB chassis for optimum resolution of the input voltage. A MATLAB script controlled the voltage ramp over a specified time-period and thus the spindle acceleration. In this study, a transient speed sweep was performed from 0 – 15 000 rpm in a 4 s period, with 750 N of static radial load applied to the shaft. The bearing under test was a single row cylindrical roller bearing, NU 205 ECP, located in an aluminium test bracket that had an extruded bore for instrumentation.

3.1.2 Instrumentation

The outer surface of the bearing bore was instrumented with two Type 4383 single-axis piezo-electric charge accelerometers, with a frequency range of 0.1 – 8.5 kHz and sensitivity of 3.16 pC/ms². These measured acceleration of the bracket's bore,

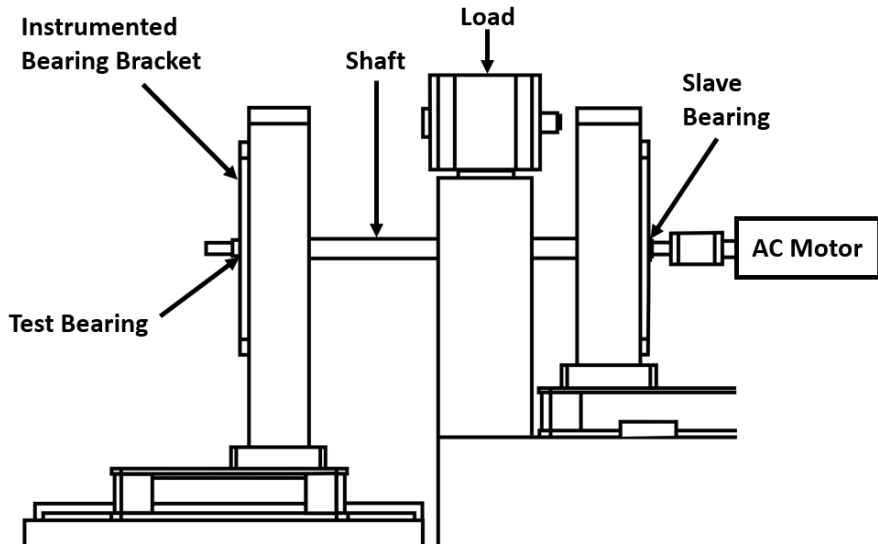


Figure 3.5 Experimental rig schematic.

corresponding to the outer race of the bearing (Figure 3.6). Two single beam laser vibrometers measured the displacement of the shaft at the edge of the bearing which corresponds to the displacement of the inner race of the bearing (Figure 3.7). A dual-beam vibrometer was used to measure the rotational speed of the shaft. All laser vibrometers had a frequency range of 0 – 10 kHz and maximum speed of 20 000 rpm.

A program in MATLAB controlled the speed of the shaft through a ramped voltage input. Data was simultaneously acquired from the accelerometers and laser vibrometers through synchronised input channels at a sampling rate of 100 kHz. Simultaneous control and data acquisition ensure accurate results between different instrumentation locations.

3.1.3 Signal Processing

The bearing race displacements were obtained from the instrumented bearing using time-domain data from the accelerometers and laser vibrometers. The laser vibrometer directly provided displacement data, whereas the accelerometer data required post-processing of acceleration data. To ascertain the displacement of the bearing bore and thus outer bearing race, the accelerometer results were integrated twice:

$$v_{out}(t) = v_{0,out} + \int_0^t a_{out} dt \quad (3.1)$$

$$x_{out}(t) = x_{0,out} + \int_0^t v_{out} dt \quad (3.2)$$

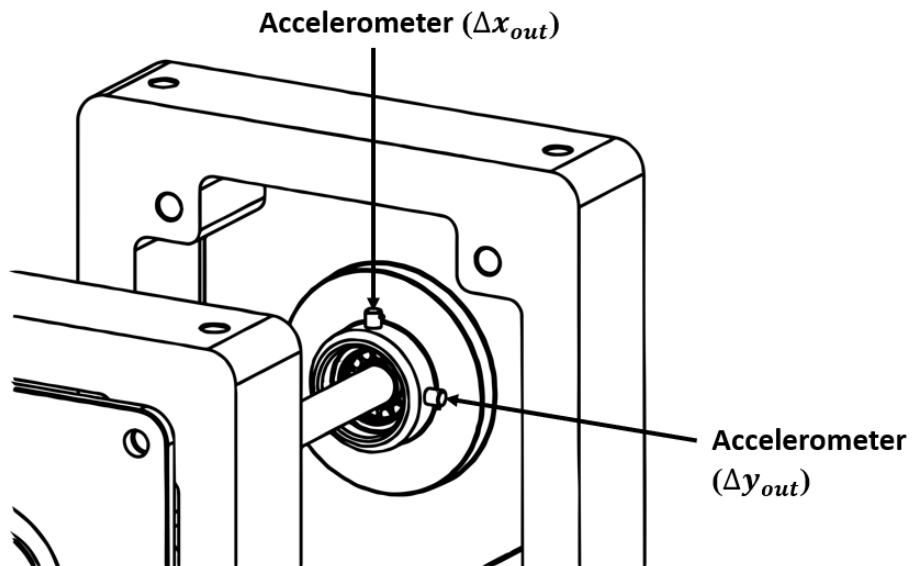


Figure 3.6 Accelerometer locations on test bracket.

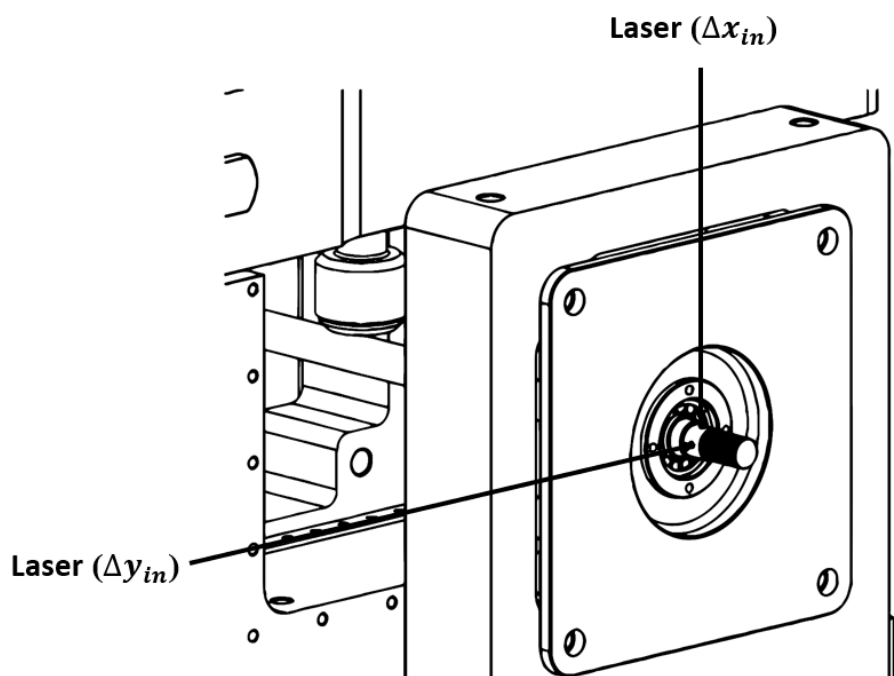


Figure 3.7 Laser vibrometer locations on shaft.

As this double integration amplifies non-linearities in the original signal, it requires pre-processing [34]. Low frequency drift is removed from the unfiltered time-domain data by applying a linear fit to the data and then removing the trend from it.

To extract the frequency content of the speed ramp, waterfall plots were generated using the accelerometer and laser vibrometer data. Short-time fast-Fourier transform (STFFT) was used, with data windows of six shaft rotations at each 100 rpm increment. The resulting signal was then filtered using a Butterworth bandpass filter for a frequency range of 70 - 10 000 Hz to remove the high amplitude low frequency noise that was inherent to the equipment setup. The filter used 3 dB of passband ripple and 7 dB attenuation in the stopbands, which were set at 35 - 12 500 Hz. The relative displacement of the bearing centre could then be obtained from the relative displacement between the shaft (measured using the single beam laser vibrometer) and bearing bore:

$$\Delta x = \Delta x_{in} - \Delta x_{out} \quad (3.3)$$

$$\Delta y = \Delta y_{in} - \Delta y_{out} \quad (3.4)$$

where Δx_{in} and Δx_{out} correspond to the displacements of the shaft and bearing bore respectively.

3.1.4 Contact Mechanics at the Roller Race Conjunction

The contact between roller and race is modelled as an elastic deformation between an equivalent finite length elastic cylinder and rigid plate. This assumption is realistic under the conditions of an EHL contact. The contact force on an individual roller at each instantaneous position, W_i , is obtained from the Hertzian load-deflection relationship:

$$W_i = k\delta_i^n \quad (3.5)$$

where k is the Hertzian contact stiffness non-linearity between a rolling element and the inner or outer raceway groove. For the case of rolling element bearings, the exponent of localised deflection, n , is equal to 10/9 [11]. The contact deflection of a roller relative to the race, δ_i , is due to the normal dynamic motion (i.e. the local mutual convergence) of the inner and outer bearing races, contribution of lubricant film thickness and any additional clearance or interference fit [28]. This is expressed as:

$$\delta_i = 2(h_{c,i} - C) + x\cos(\theta_i) + y\sin(\theta_i) \quad (3.6)$$

where C is the local radial clearance, and x and y are the displacement components of the inner bearing race from its geometric centre. This normal approach between both races is the sum of the total deformation of the rollers and both races [35], hence:

$$\delta_i = \delta_{i,in} + \delta_{i,out} \quad (3.7)$$

The equilibrium of forces in a system of stiffnesses in series is therefore:

$$W_i = W_{i,out} = W_{i,in} \quad (3.8)$$

To find the individual deflection of each contact due to differences in contact stiffness, the following relationship is used:

$$\delta_{i,in}^n k_i = \delta_{i,out}^n k_{out} \quad (3.9)$$

The deflection value at each contact based on the total deflection and relationship between contact stiffness is then found from Equations 3.7 and 3.9 to give:

$$\delta_{i,out} = \frac{\delta_i}{\left(\frac{k_{out}}{k_{in}}\right)^{\frac{1}{n}} + 1} \quad (3.10)$$

The normal stiffness of the inner and outer races differs due to their geometry. To calculate the stiffness at each contact, the following equation is used:

$$\delta = \frac{F}{\pi E_r L} \left[\ln \left(\frac{4\pi E_r R_{zx} L}{F} \right) - 1 \right] \quad (3.11)$$

The deflection for a range of loads is calculated based on the geometry and material properties at the inner and outer race contacts. This non-linear relationship is numerically obtained and then curve fitted and represented by a power function in the form $F = a\delta^b$, with $b = 10/9$ and a representing the contact stiffness. Individual contact stiffness and deflection at the inner and outer race contacts is then found. The overall contact stiffness, $K_{i,total}$, is given by:

$$K_{i,total} = \frac{1}{\left(\frac{1}{K_{i,in}}\right) + \left(\frac{1}{K_{i,out}}\right)} \quad (3.12)$$

where $K_{i,in}$ and $K_{i,out}$ are the stiffnesses of the inner and outer race contacts respectively.

3.1.5 Implicit Tribological Model

A stepwise solution was performed on an individual roller as it passes through each angular position. The roller bearing and bracket tolerances are such that the internal clearance is $0\mu m$ between roller and race. This means that in an unloaded state, there is no deflection of elements or raceway. It also means that displacement in positive x-y corresponds to the same total magnitude of deflection of roller and race contact. For each time step, the bearing is first assumed to be in equilibrium position, and film thickness is assumed to be $0\mu m$. The deflection of the bearing is calculated under these conditions and is therefore a function of the relative displacement between inner and outer bearing races. With deflection at the time step calculated, the resultant lubricant regime and subsequent analytical solutions can be performed based on the following three conditions:

1. $\delta = 0$ indicates a film of $0 \mu m$ and no load.
2. $\delta < 0$ indicates complete separation of the roller and race. In this instance, the lubricant is assumed to fill the separation gap, with the film thickness value equalling the magnitude of the separation:

$$h_i = |\delta_i| \quad (3.13)$$

Under this condition, the lubrication is in the hydrodynamic regime. The hydrodynamic lubricant reaction load was derived by Rahnejat [36], and is given by:

$$W_i = \frac{2bu_i\eta_0 R_{zx}}{h_i} \quad (3.14)$$

where b is the half length of the contact, u is the speed of lubricant entrainment into the contact, η_0 is the lubricant viscosity, R_{zx} is the reduced radius of the roller and race and h is lubricant film thickness.

3. $\delta > 0$ indicates deflection at the roller-race contact. This means that contact pressure is sufficiently high for the lubrication regime to be elastohydrodynamic. For the elastohydrodynamic regime, an iterative process is performed to solve film thickness. This is due to the contribution of EHL film towards deformation and consequently the load in the contact.

The cylindrical roller and race contacts are modelled by an equivalent rigid roller against a semi-infinite elastic half space of equivalent elastic modulus, E_r . The

extrapolated central film thickness for a line contact is therefore obtained [37] from:

$$h_c = R_{zx} \left[3.06 G^{*0.56} U^{*0.69} W^{*-0.1} \right] \quad (3.15)$$

where the following dimensionless parameters are used:

$$G^* = \alpha E_r \quad (3.16)$$

$$U^* = \frac{u \eta_0}{R_{zx} E_r} \quad (3.17)$$

$$W^* = \frac{W}{L E_r R_{zx}} \quad (3.18)$$

where R is the reduced radius of the contact, L is the length of the roller and u is the speed of entraining motion into the contact and W is the contact load. Assuming pure rolling, the speed of entraining motion is given by:

$$u_i = \frac{1}{2} (\omega_{c,i} - \omega_{ri,i}) r_{in} \quad (3.19)$$

An iterative process is used to calculate load on the roller based on total deflection including lubricant film (Equation 3.6). At each time step where an EHL film is present, the following convergence criteria must be met before the next time step is calculated:

$$\frac{h_i^n - h_i^{n-1}}{h_i^{n-1}} \leq 0.01 \quad (3.20)$$

3.1.6 Friction Calculations

Frictional power is a crucial factor for characterising their performance. Under modern high-speed conditions, it is important to also understand the frictional behaviour of the system. Roller bearings often operate within the mixed elastohydrodynamic regime of lubrication. Friction is generated by a combination of viscous shear of the lubricant and asperity interactions. Total friction at the mixed-EHL contact is a combination of the boundary friction, f_b , and hydrodynamic or viscous friction, f_v :

$$f = f_v + f_b \quad (3.21)$$

Boundary friction is a function of asperity contact pressure, calculated using the Greenwood and Tripp model in this paper [38]:

$$f_b = \tau_0 A_a + \zeta W_a \quad (3.22)$$

where τ_0 is the Eyring shear stress of lubricant and ζ is the pressure coefficient for shear strength of asperities, obtained from asperity level friction measurement. Asperity load, W_a , and area occupied by asperities within the apparent contact A_a are obtained as below, assuming a Gaussian distribution of asperity peak counts:

$$W_a = \frac{16\sqrt{2}}{15} \pi (\zeta \kappa \sigma)^2 \sqrt{\frac{\sigma}{\kappa}} E_r A_a F_{5/2}(\lambda) \quad (3.23)$$

and

$$A_a = \pi^2 (\zeta \kappa \sigma)^2 A F_2(\lambda) \quad (3.24)$$

where $\lambda = \frac{h}{\sigma}$ is the Stribeck parameter and $F_{5/2}(\lambda)$ and $F_2(\lambda)$ are statistical functions obtained from numerical integration of the Gaussian distribution of asperities.

Viscous Friction due to shearing of the lubricant film in the EHL contact is found using the below experimentally validated formulae [39]:

$$f_v = \mu W \quad (3.25)$$

where

$$\mu = 0.87 \alpha \tau_0 + 1.74 \frac{\tau_0}{\bar{p}} \ln \left[\frac{1.2}{\tau_0 h} \left(\frac{2K\eta_0}{1+9.6\xi} \right)^{\frac{1}{2}} \right] \quad (3.26)$$

where \bar{p} is the average pressure at the apparent contact, K is the lubricant thermal conductivity and ξ is given by:

$$\xi = \frac{4}{\pi} \frac{K}{h/R_{zx}} \left(\frac{\bar{p}}{E_r R_{zx} K \rho' c' u} \right)^{\frac{1}{2}} \quad (3.27)$$

where K' , ρ' and C' are respectively the thermal conductivity, density, and specific heat capacity of the contacting solid.

To inform the boundary friction model, surface topography data are required. An Al-Icona InfiniteFocus Variation Microscope with a $\times 10$ objective was used for topography measurements to calculate the roughness parameter, $n\sigma\beta$. This had a vertical resolution of 30 nm and sampling point separation of 176.9 nm in the $y - z$ plane of the roller and 1 nm in x . An area of 530 by 588 μm was captured. Data was processed using Vision65

Table 3.1 Surface Topography Data

Parameter	Value
Root-mean-square height	0.197 μm
Density of peaks	0.00116 1/ $(\mu\text{m})^2$
Arithmetic mean peak curvature	0.180 1/ μm

Map Premium, where the profile of the radius of the roller was removed. The measured parameters are presented in Table 3.1

3.2 Numerical EHL Model

Whilst the analytical solution used in the implicit tribological model provides central film thickness, the film thickness and pressure distributions can only be obtained explicitly through the full solution of Reynolds equation in conjunction with rheological and elastic field models. In a line contact, where contact dimensions in the side-leakage direction (y_c) are much larger than the direction of entraining motion (x_c), pressure in y_c direction is assumed constant due to the negligible gradient and the contact can be analysed in one dimension. This assumption is valid in the contact apart from small regions near the edge. Reynolds equation is used to calculate contact pressures.

3.2.1 Reynold's Equation

Reynold's equation [4] is the governing equation of fluid film lubrication theory. For Newtonian fluids it can be derived from the full Navier-Stokes equations making the following assumptions, primarily the neglection of inertial forces and only retaining viscous forces on the lubricant [5]:

1. Body forces are negligible (mass of film is negligible)
2. Pressure is constant through the lubricant film (z-direction) due to thin film (dimensions of the region of pressure are typically 100 times the central film thickness).
3. No slip at boundaries
4. Lubricant flow is laminar (low Reynolds number)

5. Inertia and surface tension forces are negligible compared with viscous forces (working fluid has low mass and low acceleration)
6. Shear stress and velocity gradients are only significant across the lubricant film
7. The lubricant behaves as a Newtonian fluid
8. Lubricant viscosity is constant across the film
9. The lubricant boundary surfaces are parallel or at a small angle with respect to each other

Reynolds equation is a second order, non-linear partial differential equation. It is made up of the pressure induced terms (Poiseuille flow) and the boundary velocity-induced term (Couette flow).

For the line contact problem, such as that at the conjunction between a cylindrical roller and race, dimensions in the side-leakage direction, y , are much bigger than the direction of entraining motion, x . Pressure in y direction is assumed constant due to the negligible gradient, and the contact can be analysed in 1-dimension. The assumption is valid in the contact apart from small regions near the edge where the roller profile changes. A simplified 1-dimensional version of Reynolds equation can therefore be used:

$$\frac{\partial}{\partial x} \left[\frac{\rho h^3}{6\eta} \left(\frac{\partial p}{\partial x} \right) - \rho h u \right] = 2 \frac{\partial(\rho h)}{\partial t} \quad (3.28)$$

To solve Reynolds equation numerically, it must first be discretized and then solved using the finite-difference method. The following procedure explains this discretization.

Due to the steady state nature of the investigations, with the absence of shock loading, the transient squeeze term can be removed:

$$\frac{\partial}{\partial x} \left[\frac{\rho h^3}{6\eta} \left(\frac{\partial p}{\partial x} \right) - \rho h u \right] = 0 \quad (3.29)$$

Due to the many orders of magnitude differences between lubricant film thickness (μm) and pressures (GPa), the numerical solution often becomes unstable. Dimensionless parameters are therefore defined to remove this instability. These are as follows:

$$\begin{aligned}
U &= \frac{u}{u_{av}} & \partial x &= a \partial X \\
X &= \frac{x}{a} & \partial \rho &= \rho_0 \partial \bar{\rho} \\
\bar{\rho} &= \frac{\rho}{\rho_0} & \partial \eta &= \eta_0 \partial \bar{\eta} \\
\bar{\eta} &= \frac{\eta}{\eta_0} & \partial h &= \frac{a^2}{R_{zx}} \partial H \\
H &= \frac{h R_x}{a^2} & \partial p &= p_h \partial P \\
P &= \frac{p}{p_h} \\
W^* &= \frac{w}{E_r R_{zx} L}
\end{aligned} \tag{3.30}$$

Terms in the simplified Reynolds equation are replaced with dimensionless parameters. Similar terms are then grouped and rearranged to give the final form:

$$\frac{\partial}{\partial X} \left[\frac{\bar{\rho} H^3}{6\bar{\eta}} \left(\frac{\partial P}{\partial X} \right) \right] = \Psi \left[\frac{\partial}{\partial X} \bar{\rho} H U \right] \tag{3.31}$$

where

$$\Psi = \frac{12 u_{av} R_{zx}^2 \eta_0}{p_h} \tag{3.32}$$

Grouping terms for simplicity

$$M = \frac{\bar{\rho} H^3}{6\bar{\eta}} \tag{3.33}$$

$$Q = \bar{\rho} H \tag{3.34}$$

Making substitutions

$$\frac{\partial}{\partial X} \left[M \left(\frac{\partial P}{\partial X} \right) \right] = \Psi \frac{\partial}{\partial X} [Q U] \tag{3.35}$$

$$\left[M \frac{\partial^2 P}{\partial X^2} + \left(\frac{\partial M}{\partial X} \right) \frac{\partial P}{\partial X} \right] = \Psi \left[U \frac{\partial Q}{\partial X} + Q \frac{\partial U}{\partial X} \right] \tag{3.36}$$

The final term is removed, as velocity, U , is independent of x when no stretching of the surfaces occurs. This is then differentiated to give:

$$\frac{\partial M}{\partial X} = \frac{\partial}{\partial X} \left[\frac{\bar{\rho} H^3}{6\bar{\eta}} \right] = \frac{H^2}{2\bar{\eta}} \left[\left(\frac{H}{3} \right) \frac{\partial P}{\partial X} + \bar{\rho} \frac{\partial H}{\partial X} - \left(\frac{\bar{\rho} H}{2\bar{\eta}} \right) \frac{\partial \bar{\eta}}{\partial X} \right] \tag{3.37}$$

and

$$\frac{\partial Q}{\partial X} = \frac{\partial}{\partial X} [\bar{\rho} H] = H \frac{\partial \bar{\rho}}{\partial X} + \bar{\rho} \frac{\partial H}{\partial X} \quad (3.38)$$

Substituting into Equation 3.36 gives the following:

$$\frac{\bar{\rho} H^3}{6\bar{\eta}} \frac{\partial^2 P}{\partial X^2} + \frac{H^2}{2\bar{\eta}} \left[\frac{H}{3} \frac{\partial \bar{\rho}}{\partial X} + \bar{\rho} \frac{\partial H}{\partial X} - \frac{\bar{\rho} H}{2\bar{\eta}} \frac{\partial \bar{\eta}}{\partial X} \right] \frac{\partial P}{\partial X} - \Psi U \left[H \frac{\partial \bar{\rho}}{\partial X} + \bar{\rho} \frac{\partial H}{\partial X} \right] = 0 \quad (3.39)$$

$$\frac{\partial^2 P}{\partial X^2} + \frac{3}{\bar{\rho} H} \left[\frac{H}{3} \frac{\partial \bar{\rho}}{\partial X} + \bar{\rho} \frac{\partial H}{\partial X} - \frac{\bar{\rho} H}{2\bar{\eta}} \frac{\partial \bar{\eta}}{\partial X} \right] \frac{\partial P}{\partial X} - \frac{6\bar{\eta}}{\bar{\rho} H^3} \Psi U \left[H \frac{\partial \bar{\rho}}{\partial X} + \bar{\rho} \frac{\partial H}{\partial X} \right] = 0 \quad (3.40)$$

The final form of the equation is therefore:

$$\frac{\partial^2 P}{\partial X^2} + \left[\frac{1}{\bar{\rho}} \frac{\partial \bar{\rho}}{\partial X} + \frac{3}{H} \frac{\partial H}{\partial X} - \frac{3}{2\bar{\eta}} \frac{\partial \bar{\eta}}{\partial X} \right] \frac{\partial P}{\partial X} - \frac{6\bar{\eta}}{H^2} \left[\frac{1}{\bar{\rho}} \frac{\partial \bar{\rho}}{\partial X} + \frac{1}{H} \frac{\partial H}{\partial X} \right] \Psi U = 0 \quad (3.41)$$

3.2.2 Finite Difference Formulation

For finite difference formulation, the central difference formula based on Taylor series expansion [6] is used. The second derivative of pressure using second order central discretization for the spatial domain is therefore:

$$\frac{\partial^2 P}{\partial X^2} = \frac{P_{i-1} - 2P_i + P_{i+1}}{\Delta X^2} \quad (3.42)$$

and the first derivative is given by:

$$\frac{\partial P}{\partial X} = \frac{P_{i+1} - P_{i-1}}{2\Delta X} \quad (3.43)$$

Replacing terms in the final form of discretized Reynold equation:

$$\frac{P_{i-1} - 2P_i + P_{i+1}}{\Delta X^2} + \left[\frac{1}{\bar{\rho}} \frac{\partial \bar{\rho}}{\partial X} + \frac{3}{H} \frac{\partial H}{\partial X} - \frac{3}{2\bar{\eta}} \frac{\partial \bar{\eta}}{\partial X} \right] \frac{P_{i+1} - P_{i-1}}{2\Delta X} - \frac{6\bar{\eta}}{H^2} \left[\frac{1}{\bar{\rho}} \frac{\partial \bar{\rho}}{\partial X} + \frac{1}{H} \frac{\partial H}{\partial X} \right] \Psi U = 0 \quad (3.44)$$

$$\frac{P_{i-1} + P_{i+1}}{\Delta X^2} + \left[\frac{1}{\bar{\rho}} \frac{\partial \bar{\rho}}{\partial X} + \frac{3}{H} \frac{\partial H}{\partial X} - \frac{3}{2\bar{\eta}} \frac{\partial \bar{\eta}}{\partial X} \right] \frac{P_{i+1} - P_{i-1}}{2\Delta X} - \frac{6\bar{\eta}}{H^2} \left[\frac{1}{\bar{\rho}} \frac{\partial \bar{\rho}}{\partial X} + \frac{1}{H} \frac{\partial H}{\partial X} \right] \Psi U = \frac{2P_i}{\Delta X^2} \quad (3.45)$$

Pressure at each node point can then be represented by:

$$P_i = \frac{\frac{P_{i-1}+P_{i+1}}{\Delta X^2} + \left[\frac{1}{\bar{\rho}} \frac{\partial \bar{\rho}}{\partial X} + \frac{3}{H} \frac{\partial H}{\partial X} - \frac{3}{2\bar{\eta}} \frac{\partial \bar{\eta}}{\partial X} \right] \frac{P_{i+1}-P_{i-1}}{2\Delta X} - \frac{6\bar{\eta}}{H^2} \left[\frac{1}{\bar{\rho}} \frac{\partial \bar{\rho}}{\partial X} + \frac{1}{H} \frac{\partial H}{\partial X} \right] \Psi U}{2 \left(\frac{1}{\Delta X^2} \right)} \quad (3.46)$$

Simplified to

$$P_i = \frac{P_{xx} + P_x - E}{2 \left(\frac{1}{\Delta X^2} \right)} \quad (3.47)$$

where

$$P_{xx} = \frac{P_{i-1} + P_{i+1}}{\Delta X^2} \quad (3.48)$$

$$P_x = \frac{P_{i+1} - P_{i-1}}{2\Delta X} \left[\frac{1}{\bar{\rho}} \frac{\partial \bar{\rho}}{\partial X} + \frac{3}{H} \frac{\partial H}{\partial X} - \frac{3}{2\bar{\eta}} \frac{\partial \bar{\eta}}{\partial X} \right] \quad (3.49)$$

$$E = \frac{6\bar{\eta}}{H^2} \left[\frac{1}{\bar{\rho}} \frac{\partial \bar{\rho}}{\partial X} + \frac{1}{H} \frac{\partial H}{\partial X} \right] \Psi U \quad (3.50)$$

3.2.3 Effect of pressure on lubricant viscosity

EHL temperatures are typically in the region of 0.5-4 GPa. The resultant behaviour of the viscosity at these pressures is instrumental in forming the EHL film and must be accounted for. The Barus law [40] determines viscosity increase with pressure assuming constant ambient temperature:

$$\eta = \eta_0 \exp(\alpha p) \quad (3.51)$$

where η is the lubricant viscosity at gauge pressure, p , η_0 is the viscosity at $p = 0$, and α is the pressure-viscosity coefficient (m^2/N) and is specific to the lubricant. This relationship does not account for the change in α with temperature and pressure [41], becoming inaccurate above 0.5 GPa.

A more comprehensive relationship which simultaneously includes the effects of temperature and pressure was one proposed by Roelands [42] and developed by Houpert [43]. Roelands law is therefore accurate at higher contact pressures:

$$\eta = \eta_0 \exp(\alpha^* p) \quad (3.52)$$

The Roelands pressure-viscosity coefficient, α^* , is a function of both p and θ , with θ_0 being the reference or ambient temperature, for example at the inlet:

$$\alpha^* p = [\ln(\eta_0 + 9.67)] \left\{ \left(\frac{\theta - 138}{\theta_0 - 138} \right)^{-S_0} \left[\left(1 + \frac{p}{p_0} \right)^{Z_0} - 1 \right] \right\} \quad (3.53)$$

where

$$z_0 = \frac{\alpha}{5.1 \times 10^{-9} [\ln(\eta_0) + 9.67]} \quad (3.54)$$

and

$$S_0 = \frac{\beta (\theta_0 - 138)}{\ln(\eta_0) + 9.67} \quad (3.55)$$

The oil constants Z_0 and S_0 are independent of both pressure and temperature, and Z_0 can be typically taken as 0.68 for computational purposes.

3.2.4 Effect of pressure on lubricant density

For accurate film EHL film shape calculations, the effect that pressure has on the lubricant density must be considered. The most common equation for this is the widely used Dowson and Higginson model [44]:

$$\rho = \rho_0 \left(1 + \frac{0.6 \times 10^{-9} p}{1 + 1.7 \times 10^{-9} p} \right) \quad (3.56)$$

where ρ_0 is the lubricant atmospheric pressure. Further modifications can be made to account for the effects of temperature:

$$\rho = \rho_0 \left(1 + \frac{0.6 \times 10^{-9} p}{1 + 1.7 \times 10^{-9} p} \right) [1 - 0.65 \times 10^{-3} (\theta - \theta_0)] \quad (3.57)$$

3.2.5 Effect of temperature on viscosity

Most EHL work assumes constant temperature of the contact and that viscosity and density are dependent on pressure only. Standard experiments have been performed to assess effect of temperature on viscosity. Results have previously been curve fit by Crouch and Cameron [45], with the most simple fit due to Reynolds:

$$\eta = \eta_s \exp(-\beta \Delta \theta) \quad (3.58)$$

where η_s is the viscosity of the lubricant at temperature θ_s , η is the viscosity at representative temperature, θ , and $\Delta\theta$ represents the temperature difference between the two. β is the thermoviscous constant and is lubricant specific. This relationship is only valid for small temperature rises of the lubricant. A more accurate and widely used equation is the expression from Vogel:

$$\eta = K \exp \left(\frac{b}{\theta + c} \right) \quad (3.59)$$

with the three constants dependant on the lubricant, obtained from knowing three pairs of values for θ and η .

3.2.6 1D EHL Solution Methodology

The methodology for the 1D EHL solution used within this thesis is as follows.

Reynolds equation is used to calculate contact pressures. Assuming a thin film of Newtonian lubricant in a line contact, the following form is used and discretized in the manner shown previously:

$$\frac{\partial}{\partial X} \left[\frac{\bar{\rho} H^3}{6\bar{\eta}} \left(\frac{\partial P}{\partial X} \right) \right] = \Psi \left[\frac{\partial}{\partial X} \bar{\rho} H U \right] \quad (3.60)$$

where X is the direction of entraining motion into the contact. Squeeze film motion is neglected for this analysis. The pressure-density relationship in the compressible model is modelled using Dowson-Higginson [44] (3.56). The Roelands [42] model (3.52) is used for the pressure-viscosity relationship.

Pressure distribution is obtained from the variations in film thickness at the contact, which is defined as below:

$$h = h_0 + \frac{x^2}{2R_{zx}} - \frac{2}{\pi E_r} \int_{x_{c,in}}^{x_{c,out}} p \ln(x-x')^2 dx' \quad (3.61)$$

where h_0 is the central film thickness, the second term represents an idealised film thickness parabola, with the final term representing the localised contact deflection. Central film thickness is first estimated using:

$$h_0 = R_{zx} 3.06 G^{*0.56} U^{*0.69} W^{*-0.1} \quad (3.62)$$

$$G^* = \alpha E_r \quad (3.63)$$

$$U^* = \frac{u\eta_0}{R_{zx}E_r} \quad (3.64)$$

$$W^* = \frac{w}{LE_rR_{zx}} \quad (3.65)$$

Below, the method of solution for the numerical EHL model is provided:

1. Input the load value obtained from the implicit tribological model for an instantaneous position as well as contact kinematics from experimental conditions.
2. An initial estimation of lubricant film thickness, h_0 is made.
3. Inlet and outlet distances are set to $-4.5a$ to $1.5a$ based on the contact half width calculation. This sets up the computational domain, and assumes fully flooded inlet conditions.
4. Pressure distribution and film thickness are obtained through simultaneous solutions of equations 3.60 to 3.62 using the dimensionless parameters defined in 3.30. The Newton-Raphson iterative scheme is used for speed and robustness of convergence [46]. Pressure convergence criterion is required for the iterative solution:

$$\text{Err}_{\text{pressure}} = \frac{\sum_{i=1}^n |p_{\text{new}} - p_{\text{old}}|}{\sum_{i=1}^n p_{\text{old}}} \leq \varepsilon_p \quad (3.66)$$

where $\varepsilon_p = 1 \times 10^{-5}$.

Under-relaxation is applied between successive iterations where the criterion is not met:

$$p_{\text{new}} = (1 - \gamma)p_{\text{old}} + \gamma p_{\text{new}} \quad (3.67)$$

where the under-relaxation factor is typically $0.01 \leq \gamma \leq 0.8$

5. Hydrodynamic reaction load is calculated using the integration of pressure over the computational domain:

$$W_h = L \int pdx \quad (3.68)$$

The total reaction from the hydrodynamic load should be equal to the total load share on the roller, W_i , obtained from the explicit tribological model. The following convergence criterion is applied:

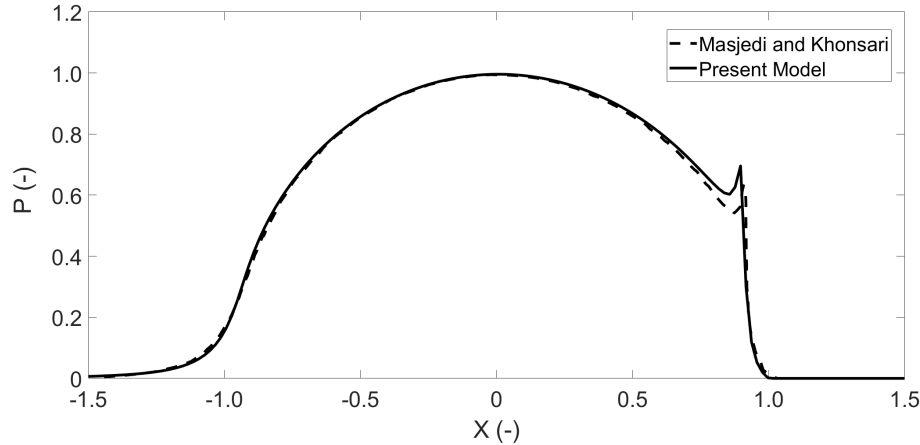


Figure 3.8 Validation of dimensionless pressure distribution, present model (solid), Masjedi and Khonsari (dashed).

$$\frac{|W_i - W_h|}{W_i} \leq \varepsilon_W \quad (3.69)$$

where $\varepsilon_W = 0.001$

3.2.7 Numerical EHL Model Validation

!!ADD FURTHER VALIDATION WALKER!!

Conjunction level validation of the numerical method for solving the EHL film thickness and pressure distributions was performed using the work of Masjedi and Khonsari [47]. These were validated against their smooth surface plots with no asperity pressure contribution. The dimensionless input parameters were $W^* = 1 \times 10^{-4}$, $U^* = 1 \times 10^{-11}$ and $G^* = 4500$. The results shown in Figure 3.8 and Figure 3.9 show a good agreement between the model used in the study and the work of Masjedi and Khonsari for the dimensionless pressure, P , and dimensionless film thickness, H , respectively.

3.2.8 Experimental Result Verification

The experimental results obtained from the presented rig were verified against analytically calculated frequency contents. This was to ensure the correct post processing of data for the input to numerical models. The bearing and lubricant data properties are given in Table 3.2 and Table 3.3 respectively which were also used in simulations.

Primary frequencies in the system due to the interaction of the rolling elements, races and the shaft could then be verified. These frequencies were calculated analytically, with f_{bpi} and f_{bpo} representing the ball pass frequencies of the inner and outer race respectively and f_{shaft} being the rotational frequency of the shaft:

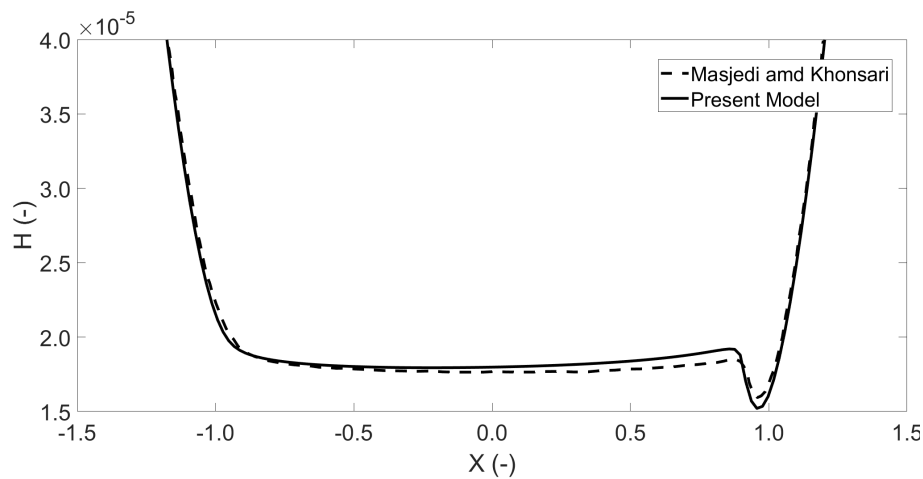


Figure 3.9 Validation of dimensionless film thickness distribution, present model (solid),
Masjedi and Khonsari (dashed)

Table 3.2 Bearing Specification

Parameter	Value
Inner Race Bore	25 mm
Inner Race Diameter	31.5 mm
Outer Race Diameter	46.5 mm
Roller Diameter	7.5 mm
Roller Length	9 mm
Number of Rollers	12
External Load	740 N
Radial Interference	0 μ m

Table 3.3 Lubricant and Material Properties

Parameter	Value
Pressure Viscosity Coefficient (α)	$2.1 \times 10^{-8} \text{ Pa}^{-1}$
Atmospheric lubricant dynamic viscosity	0.08 Pa.s
Lubricant inlet density (ρ_0)	$833.8 \text{ kg} \cdot \text{m}^{-3}$
Eyring stress (τ_0)	2 MPa
Shear strength of asperities (ζ)	0.3
Thermal conductivity of fluid	$1600 \text{ W} \cdot \text{m}^{-1} \cdot \text{K}^{-1}$
Modulus of elasticity of contacting solids	210 GPa
Poisson's ratio of contacting solids	0.3
Density of contacting solids	$7850 \text{ kg} \cdot \text{m}^{-3}$
Thermal conductivity of contacting solids	$46 \text{ W} \cdot \text{m}^{-1} \cdot \text{K}^{-1}$
Specific heat capacity of contacting solids	$470 \text{ J} \cdot \text{kg}^{-1} \cdot \text{K}^{-1}$

$$f_{bpi} = \frac{\omega_s}{2\pi} \frac{N}{2} \left(1 - \frac{D_r}{D_p} \right) \quad (3.70)$$

$$f_{bpo} = \frac{\omega_s}{2\pi} \frac{N}{2} \left(1 + \frac{D_r}{D_p} \right) \quad (3.71)$$

$$f_{\text{shaft}} = \frac{\omega_s}{2\pi} \quad (3.72)$$

At 14 000 rpm, the theoretical inner and outer race frequencies are calculated to be 1669 Hz and 1131 Hz respectively, with the experimental results being 1611 Hz and 1131 Hz. The first order shaft rotational frequency from the experiment was 232 Hz compared to theoretical calculation of 233 Hz. The above frequencies can be seen clearly in Figure 7, which shows the bearing bore displacement spectra, and Figure 8 which represents the shaft displacement spectra. The verification frequencies are identical in both, confirming that the bearing motion is accurately measured by the experimental methodology. It is observed that at certain speeds, the ball pass frequency of the outer race has a larger contribution than the inner race. This is particularly highlighted at 12 000 - 14 000 rpm. These regional effects are contributed by modal behaviour of the bracket and the bed. The critical speed of the unloaded shaft, where lateral bending

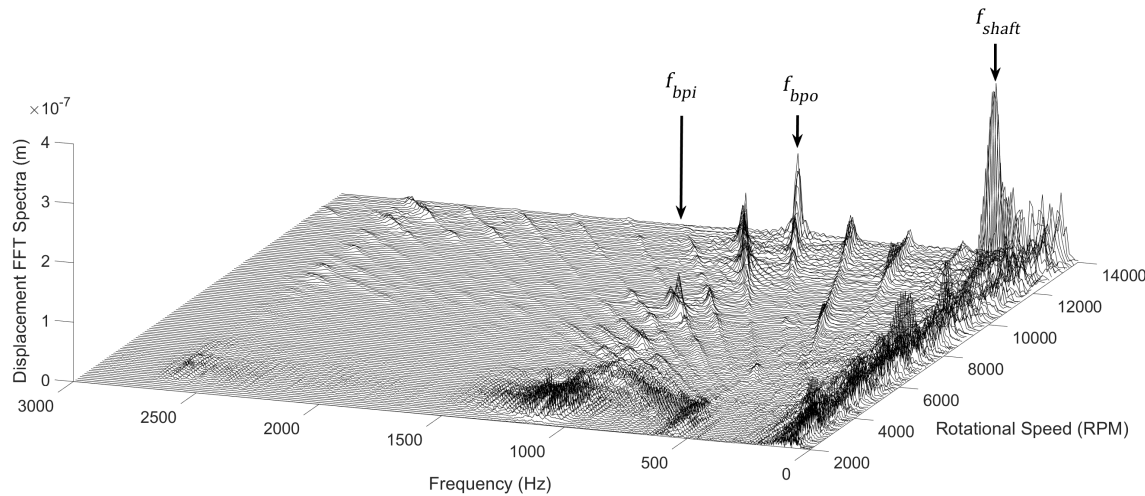


Figure 3.10 Bearing bore displacement frequency spectra.

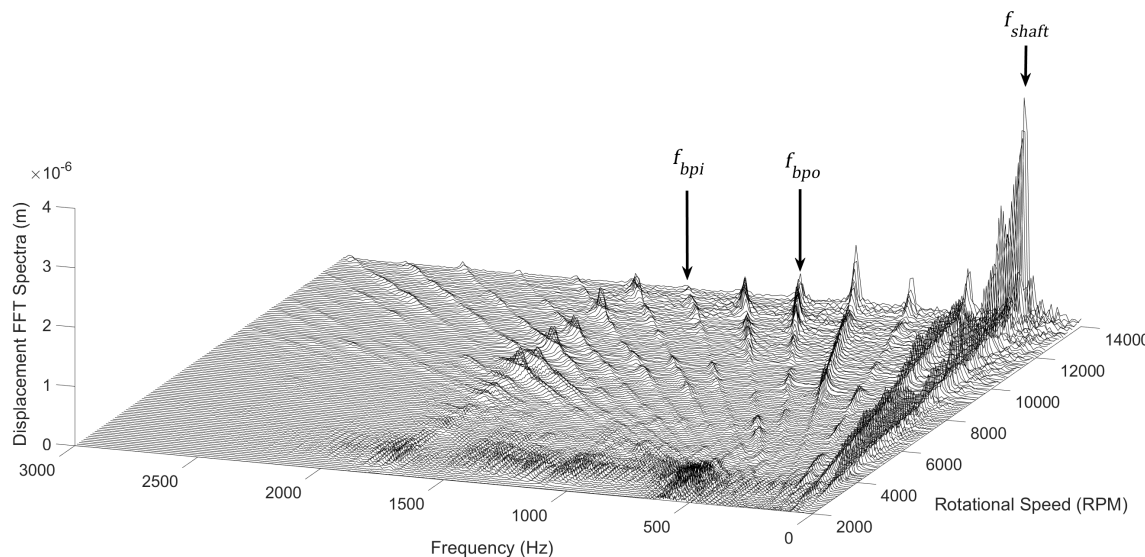


Figure 3.11 Shaft displacement frequency spectra.

frequency of the shaft is equal to the rotation frequency [48], occurs at 12 660 rpm and 211 Hz.

3.3 Results and Discussion

This section presents the results of the numerical tribological models. The kinematic data from the experimental test rig are used as the boundary conditions to the implicit and explicit models.

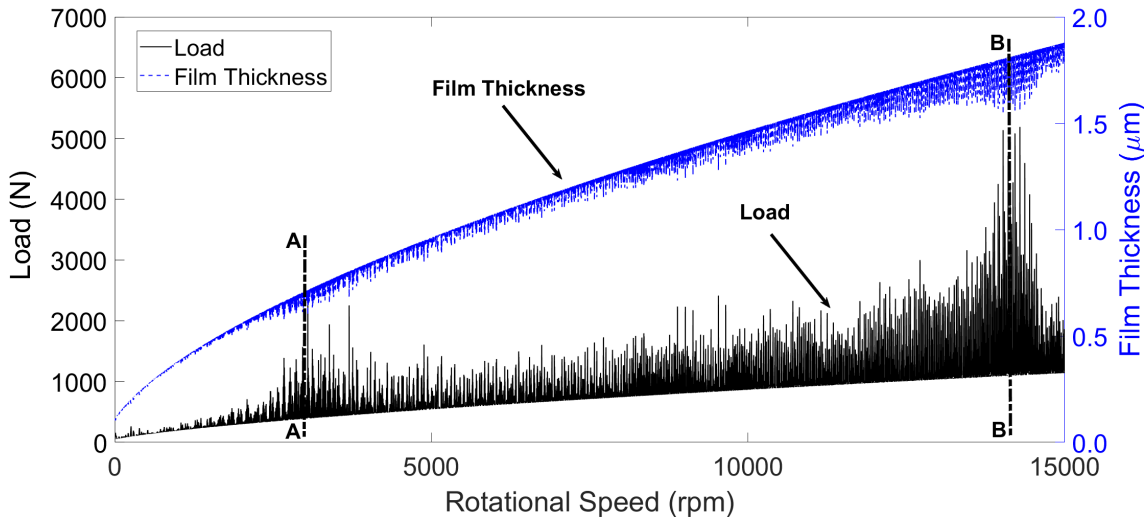


Figure 3.12 Contact load and film thickness - Outer race.

3.3.1 Film thickness and load across speed sweep

The variation in EHL film thickness and roller contact load across the speed sweep from 0 - 15 000 *rpm* at the outer race contact are shown in Figure 3.12. Only the EHL regions are shown, where loads are significant enough to cause contact deformation. The upper limit of the film is where the roller and races diverge and approach the hydrodynamic regime where the film is hence governed by the entraining motion of lubricant into the contact. The lubricant film, as seen from the film thickness equation, is more affected by the speed of entraining motion rather than the load. This explains the increasing film thickness values in Figure 3.12 despite increasing load. The film thickness is increased from 0.1 to 1.9 μm across the speed sweep, revealing a significant increase that can affect the tribodynamic behaviour of the bearing, as explained in following sections. From the tribological model, it is possible to observe the transition between mixed-EHL to the purely hydrodynamic regime as the roller passes in and out of the loaded region of the bearing. Full system and rotor dynamics also contribute to the total load on the roller, with periods of resonance at 3 000 *rpm* and 14 000 *rpm* marked as *A* and *B* respectively in Figure 3.12.

Figure 3.13 presents an interval of the speed sweep where the effect of the EHL load on reducing the film thickness under oscillating conditions can be observed and the hydrodynamic film growth as the roller is unloaded. It is possible to see the effect of the resonant frequency at 1765 *Hz* superimposed on the lower fundamental train frequency within the loaded region as the inner and outer rings converge and diverge. The results in Figure 3.13 confirm the significant effect of dynamic behaviour as well as multi-regime nature of the lubrication due to dynamic effects.

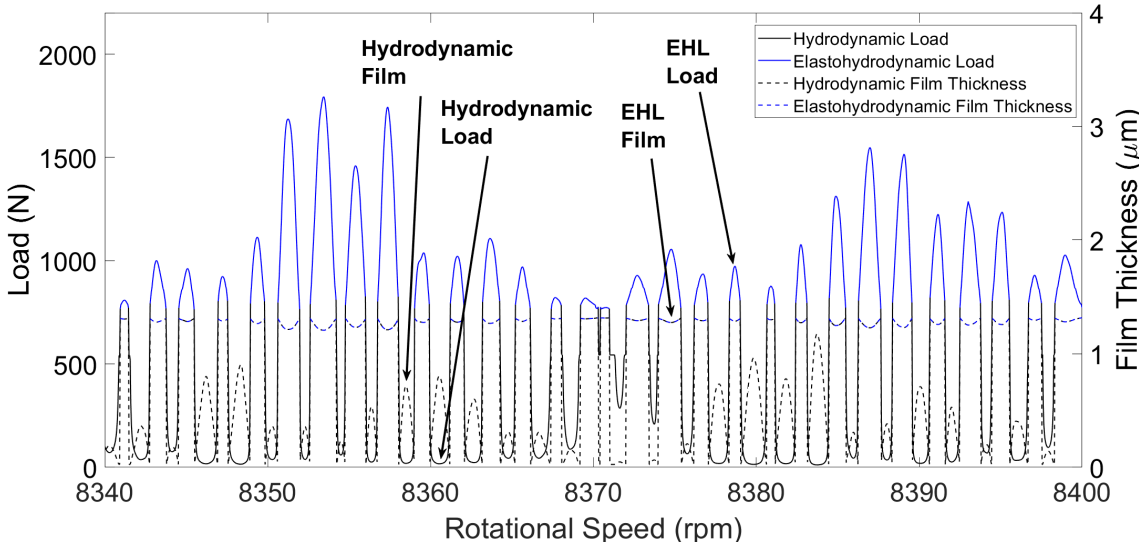


Figure 3.13 Film and load - EHL to hydrodynamic regime.

3.3.2 Friction

Focussing on data from the EHL regime, boundary and viscous friction through the speed sweep can be analysed. Figure 3.14 shows the boundary and viscous friction across the speed sweep. As the film thickness increases with speed, the separation of the contacting surfaces increases, reducing the boundary interaction of asperities. The resonant period at 14 000 *rpm* reduces the film height, increasing the likelihood of asperity interaction in that region and hence boundary friction and potential for wear. In general, the boundary friction reduces towards higher rotational and entrainment velocities. This does not, however, account for lubricant inlet starvation at high speeds or roller sliding. Viscous friction increases with higher speed and hence the shear as expected. Although the film thickness also increases at higher speeds which may reduce the amount of shear, the effect of increasing speed is more dominant. The peak values occurring again at a resonance speed of 14 000 *rpm* where the highest loads and smallest film occurs.

3.3.3 EHL Regimes

As has been demonstrated in the results analysis, the contact conditions deviate from the elastohydrodynamic regime of lubrication into the hydrodynamic regime throughout the roller orbital motion. These conditions can be verified by presenting the results on the Greenwood chart for fluid regimes of lubrication. The charts display the physical effects instrumental to EHL formation under isothermal conditions: viscosity rise due to

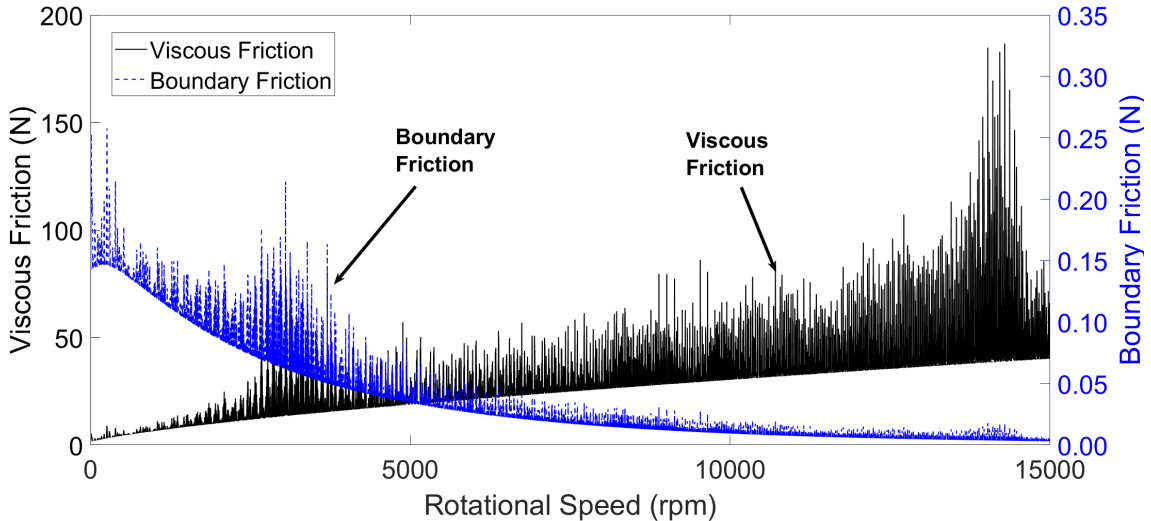


Figure 3.14 Viscous and boundary friction at the outer race contact.

pressure and elastic deformation of the surface. These two effects are quantified by two dimensionless parameters, G_e and G_v , as defined below [5]:

$$G_e = \frac{W^*}{U^{*1/2}} \quad (3.73)$$

$$G_v = \frac{W^{*3/2} G^*}{U^{*1/2}} \quad (3.74)$$

Four regions exist and the boundaries of these regions are defined by the geometry of contacting bodies, material, and lubricant properties. As is shown in Figure 3.15, the outer roller-race contact conditions move between the viscous elastic and iso-viscous rigid regimes, representing EHL and hydrodynamic respectively. The viscous elastic regime signifies the EHL regime of lubrication where contact pressures are such that elastic deformation of the surfaces and viscosity rise due to pressure increase is significant. The iso-viscous rigid regime occurs when the magnitude of elastic deformation is insignificant, and the contact pressures are low enough that viscosity rise is negligible, i.e. hydrodynamic lubrication [49]. The boundary between the two also corresponds well with the distinction being made between hydrodynamic and EHL in this methodology, presented by the black and blue regions of the plot.

3.3.4 Dry vs Lubricated Tribodynamic Model

Previously presented results confirmed the significance of considering tribodynamic coupling on the tribological predictions. The aim of this section is to assess the significance of this coupling on dynamics via affecting contact load and stiffness values. The surface

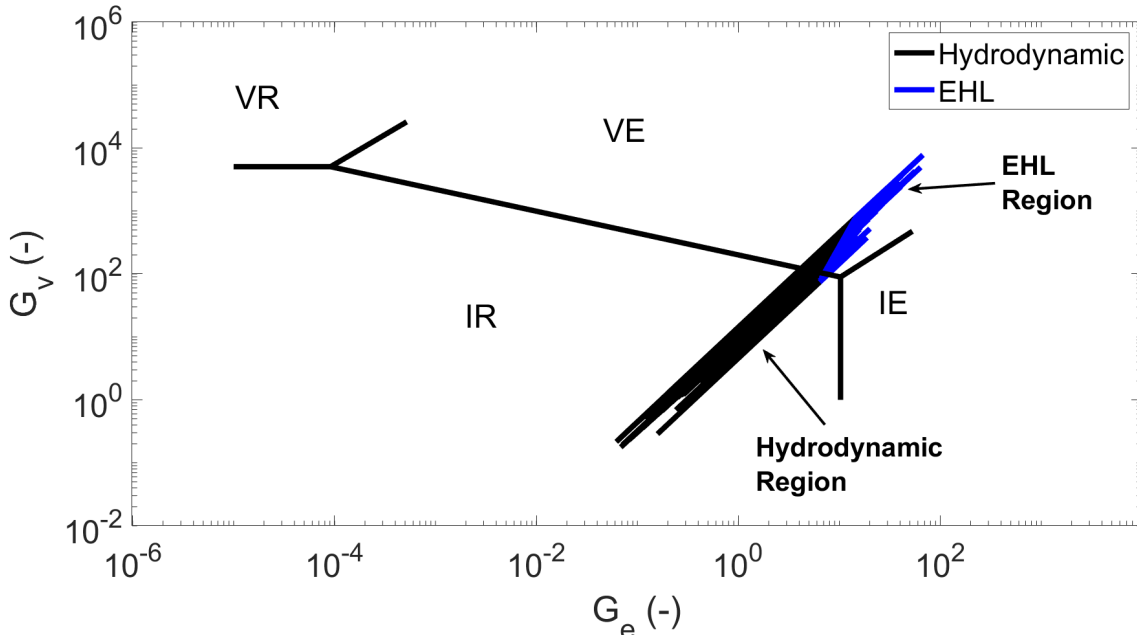


Figure 3.15 EHL and hydrodynamic conditions during roller operation. Key: IR = Iso-viscous Rigid, VR = Viscous Rigid, VE = Viscous Elastic, IE = Iso-viscous Elastic.

deformation at the EHL contact is further exacerbated by the presence of the lubricant film. Since the contact load and contact stiffness are governed by this deformation, neglecting the film leads to an underestimation of the total load at the roller-race contact. At higher speeds, such as those present in modern electrified powertrains, the growth of the lubricant film due to the increased entraining motion into the conjunction cannot be neglected – as is shown in Figure 3.12 with a film growth from 0.1 to $1.9 \mu\text{m}$. The implicit tribological model was run for two cases, including and negating lubricant film thickness in the deformation obtained from Equation 3.6. The difference in magnitude at each time step is computed, and the increase in load magnitude between a dry and lubricated model is calculated. For EHL loads, the magnitude of the load difference through the speed sweep is plotted in Figure 3.16.

There is an increasing load difference across the speed sweep, with fluctuations arising from the dynamics of the system. It is clear that neglecting lubricant film thickness leads to significant underestimation of the contact load, hence inaccurate dynamics as well as tribological calculations. This effect gains more significance at higher speeds which highlights the necessity of considering tribodynamic coupling for high-speed conditions in electrified powertrains. To fully understand the requirement for a lubricated bearing model, the percentage difference between both cases is presented at three different rotational speed snapshots of $3\,050 \text{ rpm}$, $14\,135 \text{ rpm}$, and $14\,855 \text{ rpm}$ in Figure 3.17. At low speeds and relatively low dynamic load, the addition of the

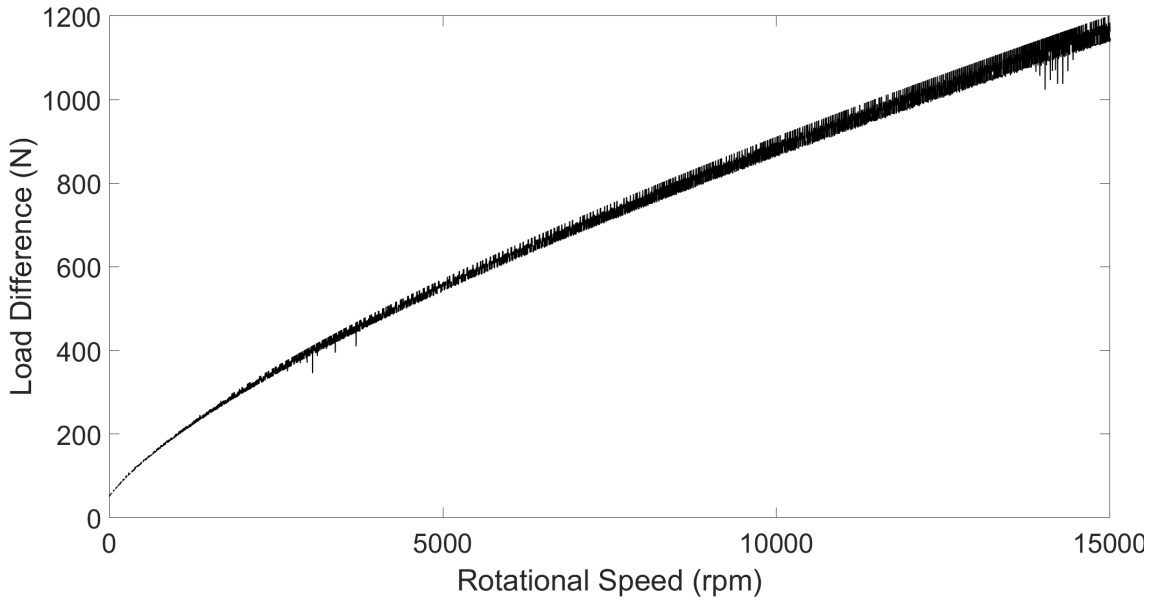


Figure 3.16 Contact load difference between dry and lubricated model.

film contributes to a 14.8% greater load prediction than a dry model, showing that the film inclusion has a significant contribution even at low rotational speeds. At shaft speeds of 14 135 rpm, the first order resonance in the system, as shown in the frequency plots, creates high dynamic loading. At peak load, the growth of the film is still present, however, the high contact deformation is close to the magnitude of the film growth, hence the difference between dry and lubricated model reaches 25.1%. As the system passes through this resonant region and the overall dynamic load is reduced, the percentage load difference reaches values as high as 149% as the effect of the film growth at high speeds exceeds that of the surface deformation.

At high speeds in periods of resonance, the magnitude of the bearing load dominates, and the effect of the increasing film thickness with speed diminishes in regions of resonance. The percentage difference between the dry and lubricated model is lower as the external force and corresponding surface deformation prevails the effect of the film. However, at high speeds outside of this period of resonance, the film thickness is of the same order as the deformation and the percentage difference between the two models is much greater.

3.3.5 Numerical EHL Results

Full numerical simulation is required to obtain detailed pressure and film thickness distributions. These distributions reveal the realistic pressure and film values at the contact for in depth durability, efficiency and thermal analysis. At 8 350 rpm, focussing

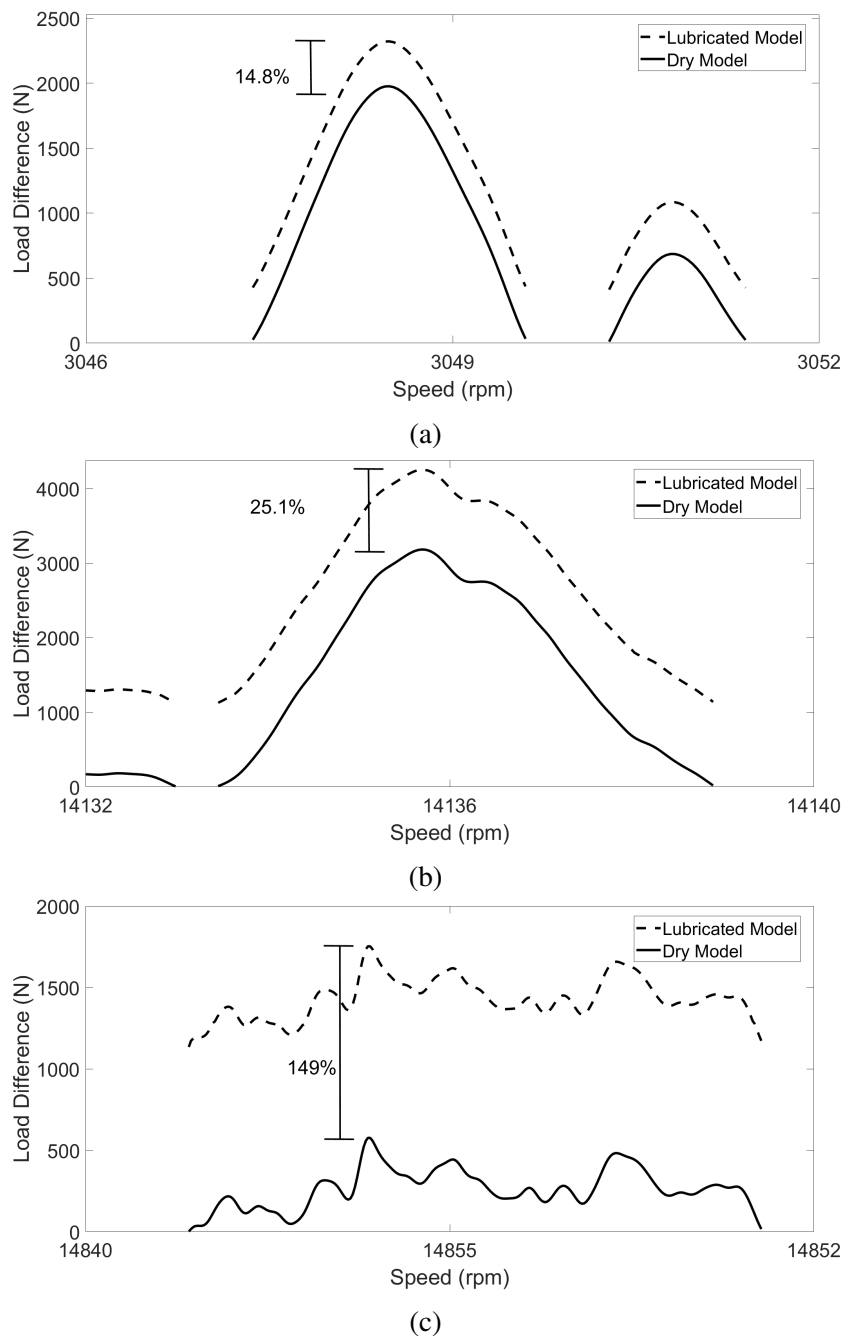


Figure 3.17 Dry and lubricated model load difference: a) 3 050 rpm, b) 14 135 rpm, c) 14 855 rpm.

on one roller orbit, the selected points for EHL numerical analysis are shown in Figure 3.18. These load values are found from the implicit tribological model when the roller enters the loaded region of the bearing. The corresponding points on the bearing circumference are also shown.

The load values are passed explicitly to the numerical EHL model along with entrainment velocity, lubricant and solid properties. From the nodes presented, the

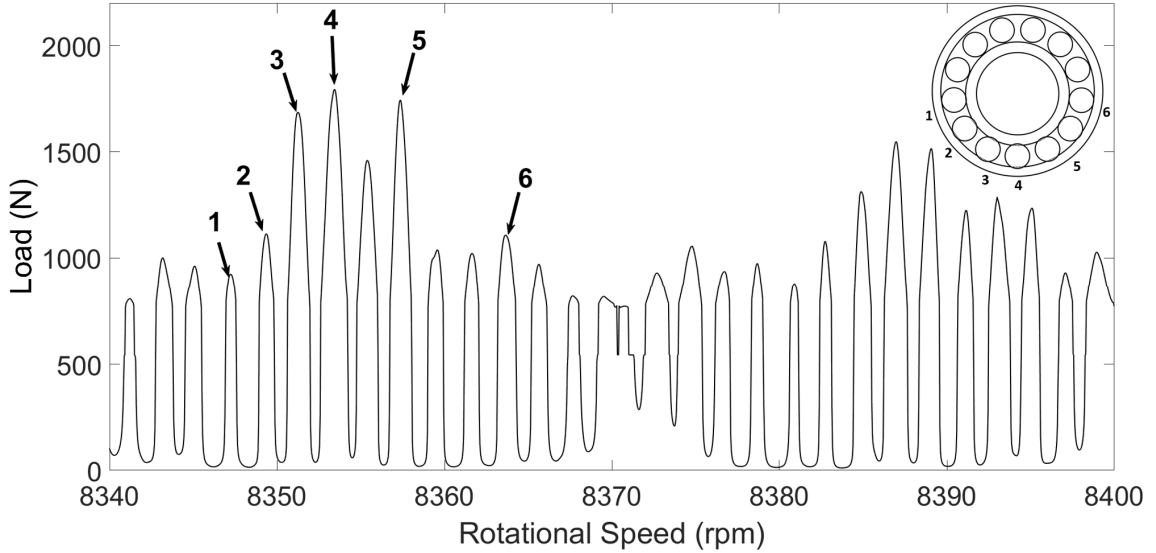


Figure 3.18 Selected points for the numerical EHL model.

pressure distribution and film thickness across the contact are obtained. These are presented in Figure 18.

In each of these plots, it is possible again to see the central film thickness drop as the roller enters, then exits the loaded region. These central film values are represented by circles in Figure 18. Agreement between the extrapolated film formulae and the numerical model for calculating central film values are presented in Table 3.4. This confirms the validity of using extrapolated film thickness equation in the implicit tribological model. It is shown that the central nodes which correspond to the higher loads in the loaded region have the lowest percentage difference in comparison to the lightly loaded nodes at the outer edges.

3.4 Conclusions

A new methodology comprising experiments and numerical modelling has been developed to allow component and conjunction level tribo-dynamic analysis of a roller bearing under speeds and loading conditions previously not reported. The experimental data contain the physics of the dynamics and tribology within the bearing, negating the need for a simplified and computationally intensive dynamic bearing model. The tribological conditions at the contact between an individual roller and raceways are numerically analysed. All possible lubrication regimes, including mixed-EHL and hydrodynamic, are considered as the roller passes through loaded and unloaded regions.

The presented research investigates a new range of working conditions under high speeds, representative of modern electrified powertrains. This study helps to understand

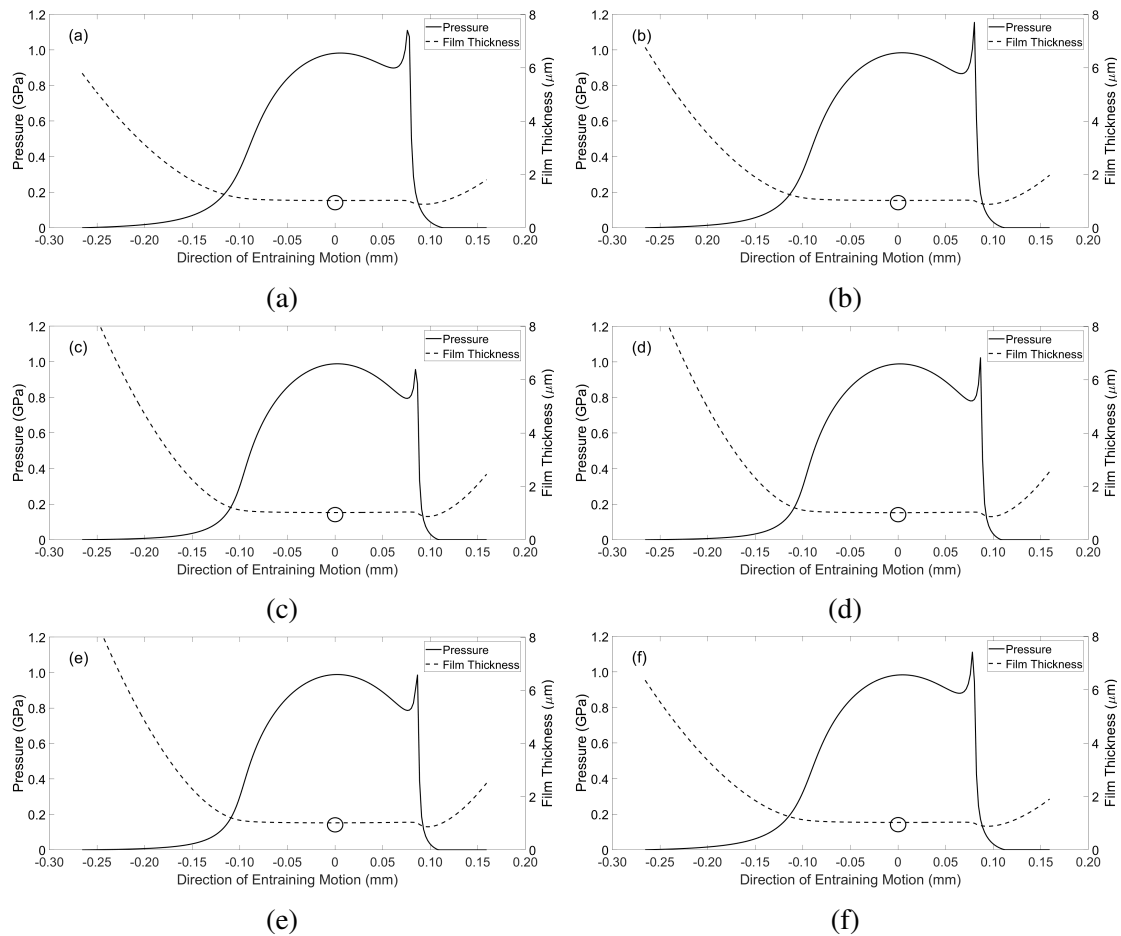


Figure 3.19 EHL pressure and film thickness distributions: a) Node 1, b) Node 2, c) Node 3, d) Node 4, e) Node 5, f) Node 6

Table 3.4 Extrapolated film formulae and numerical model central film thickness comparison

Node	Extrapolated Formulae Central Film Thickness (μm)	Numerical Model Central Film Thickness (μm)	Percentage Difference (%)
1	1.142	1.026	11.3
2	1.122	1.025	9.46
3	1.075	1.019	5.49
4	1.068	1.016	5.11
5	1.072	1.018	5.30
6	1.122	1.025	9.46

the prevailing regimes of lubrication as well as range of tribological quantities. Additionally, the interaction of tribological behaviour with dynamics of the system is investigated. The deeper and comprehensive understanding of these matters will support objective development of electrified powertrains in the future towards higher efficiency, durability and NVH refinement. The acquired knowledge and understanding will also support future developments of predictive tools by understanding the interaction of tribology and dynamics and the significance of considering this multi-physics interaction. The following conclusions can be made based on presented results:

1. The contact experiences an order of magnitude increase in film thickness across the speed sweep. This highlights the necessity of implicitly including the lubricant film in any predictive tribo-dynamic model; an approach that is not reported on in open literature for high-speed dynamic roller bearing analysis.
2. A comparison between the dry and lubricated contact model further reinforces the need to include the lubricant film in high-speed roller bearing analysis, with percentage differences in load between both models up to 149% at 15 000 rpm. Neglecting this film by using the common dry Hertzian approach would lead to an underestimation of the total load at the roller-race contact.
3. At higher speeds, such as those present in modern electric powertrains, it is shown that the growth of the lubricant film must be included implicitly within the dynamic bearing analysis.
4. The load values obtained from the lubricated tribological model have been used explicitly within a 1-dimensional EHL model to calculate the pressure distribution and film thickness across the contact. The workflow of using an explicit EHL model based on the analytical tribological contact mechanics is valid, with good agreement between central film thickness values for both.
5. The explicit EHL approach significantly improves the computational efficiency of the model whilst maintaining accuracy, since only the central value of the film is required in the load calculation. This can be implicitly coupled to broaden the scope of the analysis that is being performed.

Chapter 4

Modelling Lubricated Bearings in a Flexible Multi-Body Dynamic Environment

4.1 Preface

This chapter presents a new flexible dynamic model for drive systems comprising lubricated bearings operating under conditions representative of electrified vehicle powertrains. The multi-physics approach importantly accounts for the tribological phenomena at the roller–race conjunction and models their effect on shaft-bearing system dynamics. This is achieved by embedding a non-linear lubricated bearing model within a flexible system level model; this is something which has not, to the authors' knowledge, been reported on hitherto. The elastohydrodynamic (EHL) film is shown to increase contact deflection, leading to increased contact forces and total bearing stiffness as rotational speeds increase. Results show that for a 68 Nm hub motor operating up to 21 000 rpm, the input bearing EHL film reaches a thickness of 4.15 μm . The lubricant entrainment increases the roller–race contact deflection, causing the contact stiffness to increase non-linearly with speed. The contribution of the lubricant film leads to a 16.6% greater bearing stiffness at 21 000 rpm when compared to conventional dry bearing modelling methods used in current multi-body dynamic software. This new methodology leads to more accurate dynamic response of high-speed systems necessary for the next generation of electrified vehicles.

4.2 Introduction

Simulating electrified powertrains using flexible multi-body dynamic (FMBD) models can enable substantial cost and time savings for automotive manufacturers due to a reduced need for physical prototyping. With increasing complexity and operational speeds of these systems, the accuracy at the component level is of major importance. Bearings are crucial structural components and their dynamic response significantly affects the behaviour of the interconnected structures.

Modern electrified motors and transmissions operate at considerably higher speeds and lower loads than conventional powertrains [50]. This leads to much higher lubricant entrainment velocities at the roller–race conjunction of the bearings. Consequently, the elastohydrodynamic (EHL) film thickness can be of the same order of magnitude and often exceed that of the contact deformation predicted by dry Hertzian assumptions; hence, non-lubricated analyses are no longer valid. The operating conditions of roller bearings in modern electric vehicle (EV) powertrains require dynamic modelling to capture system transients such as time-varying input forces, acceleration and eccentricity. Early quasi-static bearing models [7] [9] [10] [11], are only applicable under steady-state operating conditions; however, the static equilibrium solutions [14] [15] [51] are of use to calculate load-deflection and individual element loading within dynamic models. Simplified 2-degree of freedom dynamic models [52] consider the purely in-plane motion of the rolling elements in the radial and lateral directions of the bearings for the investigation of the frequency response to defects [22], the varying compliance effect [53] and the radial loading affects [23]. These models increase in complexity up to 5 degrees of freedom (DOF) to observe moment loading and centrifugal effects [54] [30]. These analyses assumed a dry contact between the rolling elements and races, which was considered to be valid at lower speeds and high loads. This, however, neglects the effect of the lubricant film thickness in the contact mechanics and thus underestimates the contact deflection and hence the load.

Based on the experimental and numerical findings [55] [56] [57], the EHL film can be shown to increase the bearing stiffness, which continues to rise non-linearly with speed. It is therefore clear that the lubricant film in roller bearings operating at high speeds must be implicitly included in dynamic analyses.

As stated by Bizarre et al. [58], there are few studies in the open literature that combine the stiffness and damping of an EHL contact with classical bearing dynamics. Early lubricated bearing models use extrapolated formulae to provide a relationship between the load share and film thickness at each element's contact with the bearing raceways [59]. Aini et al. [60] implemented the extrapolated film approach from the

work of Rahnejat and Gohar [59] into a five-DOF bearing equilibrium model. The work computes the deformation at each roller–race contact, combining the EHL film thickness with the elastic deformation of the contacting solids. The force–displacement relationship is shown to follow a non-linear trend. Mohammadpour et al. [28] employed a similar implicit tribodynamic analysis and then utilised a full numerical EHL analysis explicitly for further tribological studies. In their analysis, input shaft speeds of 209 rad/s resulted in much slower entrainment velocities than are applicable for electrified powertrain analyses.

Sopanen and Mikkola [61] modelled the influence of various surface characteristics on bearing dynamics, including contributions from surface waviness, roughness, localised and distributed effects. Their six-DOF model accounts for the Hertzian contact deformation and the EHL film implicitly within the contact. This model was embedded in a multi-body dynamic (MBD) software to utilise its mathematical capabilities. This work does not, however, demonstrate the effect that the EHL film has on bearing stiffness, and the effect on system dynamics using flexible bodies is not analysed [62]. Sawalhi and Randall [63] used a constant preload approach to imitate the stiffening effect of the film. Whilst this effective preload captures the increased contact stiffness due to the presence of the EHL film, the film thickness does not vary based on the contact conditions.

More recently, Liu and Shao [64] investigated the effects of surface waviness, including the effect of the lubricant film using an equivalent stiffness model. Nonato and Cavalca [65] presented a methodology to model EHL contacts using a set of non-linear springs and viscous dampers. Bizarre et al. [58] applied this lubricated non-linear force contact to a five-DOF model of an angular contact ball bearing. This enabled a combined solution scheme for the bearing force equilibrium and the EHL contact. The formulated system of equations was solved, achieving force equilibrium for each rotation of a bearing under constant external load. The authors of this study noted the interest of combining such models within FMBD system level models.

None of the combined models above are embedded within a system level model comprising flexible bodies, and the effect of the change in the contact stiffness due to the lubricant film is not investigated at the system level. Furthermore, the high-speed operation and time-varying loads representative of electrified vehicle transmissions are not considered.

Presented in this chapter, for the first time in the open literature, a coupled simulation approach to combine an implicit lubricated bearing model within a high-speed system level FMBD model. The time-varying system operating conditions reflect that of an electrified powertrain. The kinematic behaviour of a flexible shaft at each time step of a

dynamic simulation is passed to the bearing model. A contact slicing method [14] is employed to calculate the reaction forces of the individual rolling elements based on the roller–race contact deflection [66]. The total deflection is influenced by the thickness of the EHL film within the contact, which is implicitly included within the analysis through an iterative procedure. The resulting race forces are returned to the system level model and the equations of motion are solved at each time step. Comparisons are made between modelling the bearings as dry and lubricated. The dynamic results including acceleration, force magnitudes and stiffness variations have been obtained for realistic loading conditions of a 54 kW electric hub motor up to speeds of 21 000 rpm.

4.3 Methodology

A co-simulation methodology combines a system level model of a flexible shaft and rigid housing, developed in AVL EXCITETM, with component level models of the lubricated bearings, developed in MATLAB and Simulink. Operating conditions such as rotational speed and external forces are defined in the system level model. Time step, iteration accuracy and simulation length are also defined. Material, geometric and rheological properties of the bearings are defined in the component level model. The kinematic conditions from the system level model (i.e., displacements and velocities in all active degrees of freedom) are passed to the component level model at each time step. For each individual rolling element, the non-linear force–deflection relationship is employed in conjunction with the EHL film calculations to compute the contact reaction force between the roller and race. The resultant force on the inner bearing race due to the contact forces and orbital positions of all elements is then returned to the system level model. The equations of motion are then solved, and the time step is advanced once numerical convergence is achieved. A flowchart of these models representing each time step of the simulation is shown in Figure [?].

4.4 System Level Flexible Model

The system level model consists of a flexible shaft, supported by two cylindrical roller bearings in a rigid housing (see Figure 4.2). The shaft is 472.5 mm between bearing centres, with a 50 mm main diameter and 25 mm diameter bearing seats. The cylindrical roller bearings act as interference elements between the shaft and housing. The shaft can exhibit lateral motion in both vertical (z) and horizontal (y) directions and rotation about the x -axis (see Figure 4.2). External load is applied at the shaft centre as a time-varying

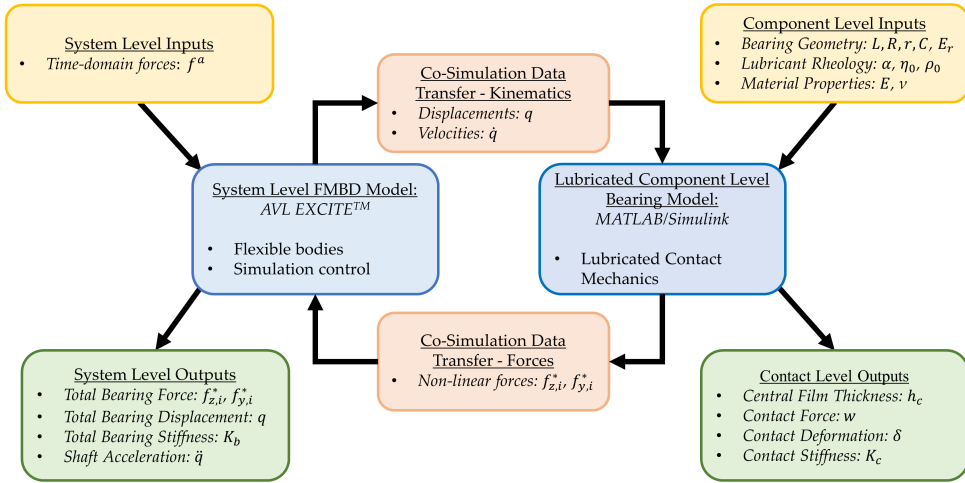


Figure 4.1 Flowchart of models.

input force, to simulate the gear mesh excitation, or as a static load. The rotational speed is input as a boundary condition.

In typical configurations containing flexible structures, it is possible for both the inner and outer races of a rolling element bearing to move when subject to load. For this analysis, however, it is sufficient to fix the outer race in space and consider only the displacement of the inner bearing race [16]. The housing in this study is treated as a rigid body of infinite stiffness; therefore, the race dynamics of the bearing are influenced only by the motion of the flexible shaft in the model. The loading on the inner race is reacted by the rolling elements on the inner raceway; this must therefore be solved to achieve a dynamic equilibrium.

Within the model, the shaft is treated as a body having linear elastic behaviour and the housing is treated as rigid. The bearings are modelled via non-linear contact forces acting between the shaft and housing.

The shaft is represented by a condensed finite element model and is discretised into a sufficiently high number of partial masses [67]. The total elastic deformation of the shaft is represented by translational and rotational displacement components of these individual partial masses. The mathematical modelling used in the FMBD solver is based on Newton's equations of motion and Euler's equation of angular momentum, respectively:

$$m_i \frac{\partial^2 x_i^{Abs}}{\partial t^2} = f_{F,i}^{Abs} \quad (4.1)$$

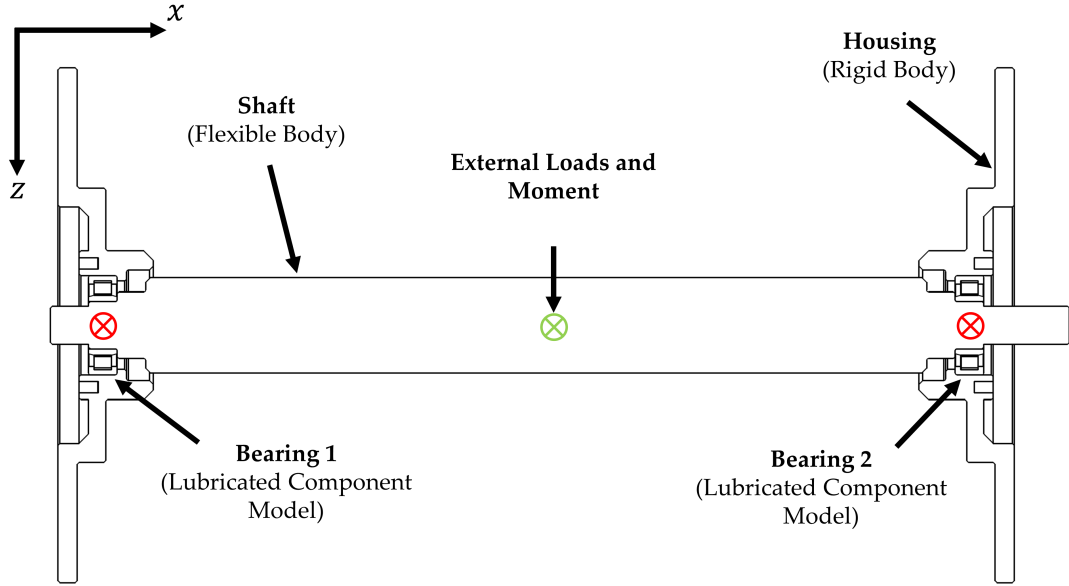


Figure 4.2 System level model schematic.

$$\frac{\partial}{\partial t} \left(I_{C,i}^{Abs} \omega_i^{Abs} \right) = f_{M,i}^{Abs} \quad (4.2)$$

where m_i and $I_{C,i}^{Abs}$ represent the mass and inertia tensors of the partial masses, i . The vectors of displacement and angular velocity are represented by x_i^{Abs} and ω_i^{Abs} respectively and are related to the centre of gravity of each partial mass. The force and moment vectors, $f_{F,i}^{Abs}$ and $f_{M,i}^{Abs}$, must be fulfilled for all partial masses in the shaft.

The combination of displacement and rotations of the shaft takes the form:

$$M\ddot{q} = f \quad (4.3)$$

where M represents the block-diagonal mass matrix of the shaft, consisting of the sub-matrices $M_i, i \in \{1, \dots, n\}$ that make up each partial mass of the full shaft. Acceleration, \ddot{q} , represents the second derivative of the displacement vector of all partial masses, $q = (q_1, q_2, \dots, q_n)^t$. Each element of this vector has 6 elements associated with it that represent the 6 degrees of freedom - 3 rotational and 3 translational ($q_i = (u_{i1}, u_{i2}, u_{i3}, \theta_1, \theta_2, \theta_3)^t$)

The forces and moments acting on each partial mass are contained in sub-vectors of force, $f = (f_1, f_2, \dots, f_n)^t$. These are split into a sum of internal force terms, f_i^{int} , external force terms, f_i^{ext} , and non-linear inertia terms, p^* . As with the partial mass terms, these are made up of six elements, each representing a degree of freedom:

$$f_i^{int} = \begin{pmatrix} f_{i,1}^{int} \\ f_{i,2}^{int} \\ f_{i,3}^{int} \\ f_{i,4}^{int} \\ f_{i,5}^{int} \\ f_{i,6}^{int} \end{pmatrix} \quad (4.4)$$

where each component of force, $f_{i,k}^{int}, k = 1, \dots, 6$ is evaluated using the linear-elastic approach

$$f_{i,k}^{int} = \sum_{j=1}^{6,n} f_{i,j,k}^{int} \quad (4.5)$$

$$f_{i,j,k}^{int} = - (d_{i,j,k} \dot{q}_k + k_{i,j,k} q_k) \quad (4.6)$$

where d and k represent the material damping and stiffness coefficients, respectively.

Grouping the damping and stiffness coefficients into one matrix gives the equation of motion after rearrangement. This equation represents the behaviour of the total system of rigid partial masses that make up the shaft, and considers both general global motion and small body motion (vibrations) [68]:

$$M \ddot{q} + D \cdot \dot{q} + K \cdot q = f^{ext} + p^* \quad (4.7)$$

The vector of external forces and moments, f^{ext} , is the sum of excitation forces, f^* , and external loads, f^a . External loads and moments applied to the shaft, f^a , are determined functions given in time and are input as both time-varying and static loads on the system. The non-linear excitation force term, f^* , represents the reaction forces from the lubricated component level bearing model.

$$f^{ext} = f^* + f^a \quad (4.8)$$

Partial mass displacements (q_i) and velocities (\dot{q}_i) at the bearing locations are output from the dynamic model and used as boundary conditions within the lubricated component level bearing model at each time step of the simulation. This model returns resultant forces and torques on the inner race of each bearing (f_i^*) which are then used to solve the equation of motion (Equation 4.7) within the dynamic model (see Figure 4.1).

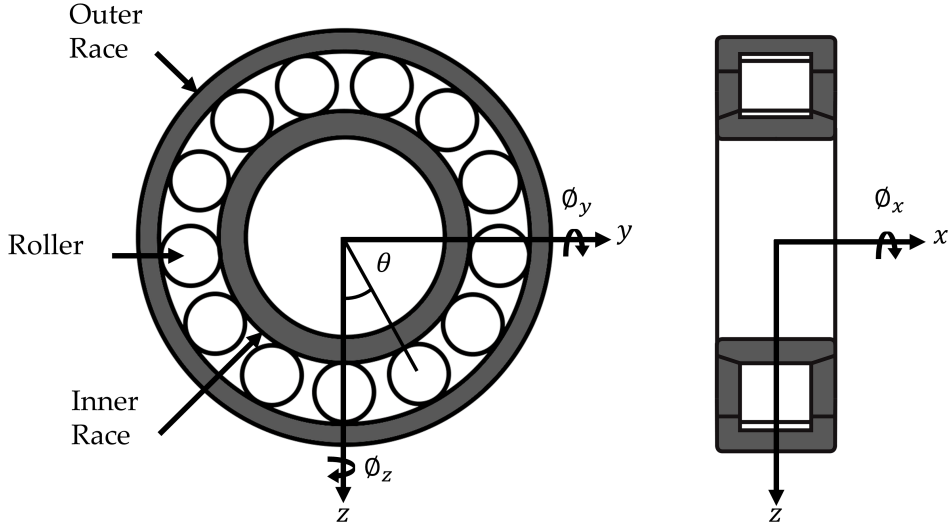


Figure 4.3 Bearing schematic.

4.4.1 Lubricated Component Level Model

The displacement and velocity vectors from each node connecting the shaft to the bearings (q_i and \dot{q}_i respectively) comprise six-DOF. For this lateral DOF model, translations in z and y are considered, as well as angular displacement around the rotational axis, x . A schematic of the bearing is shown in Figure 4.3.

Between the roller and raceways, under sufficient load, the pressures in the non-conformal contact are high enough to cause elastic deformation of the surfaces and a significant increase in lubricant viscosity. This, combined with relative motion between contacting bodies, leads to the generation of an EHL contact. The stiffness of the EHL film is typically 1-2 orders greater than the stiffness of the contacting bodies [57]. In this analysis, the film stiffness was calculated using:

$$K_{EHL} = \frac{dw}{dh_c} \quad (4.9)$$

The lowest average film stiffness was 5.1×10^9 N/m, which is over one order greater than the contacting material stiffness. The material therefore dominates the stiffness of the contact, and the stiffness of the EHL film can be neglected. The film is modelled as a rigid element that is present between the roller and race [69] [31] [32].

The contact deformation (δ) is therefore a function of the displacement of the inner bearing race, angular displacement of the roller about the rotational axis (θ) thickness

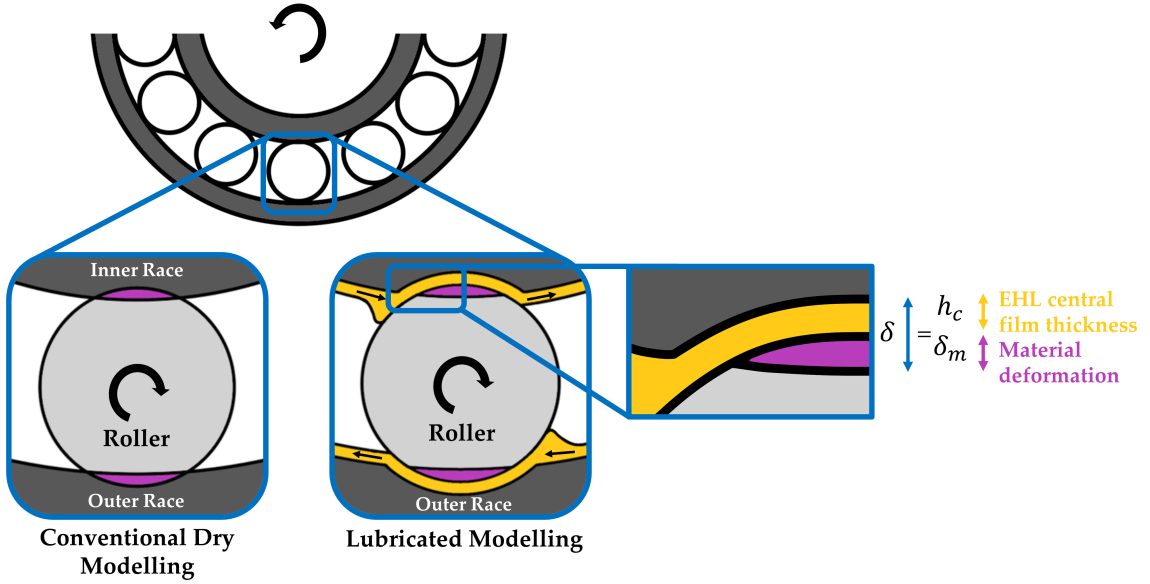


Figure 4.4 Dry vs lubricated roller-race contact.

of the EHL film (h_c) and any clearance or radial preload ($\pm C$) within the bearing [59] [28]:

$$2\delta = 2(h_c - C) + z \cos(\theta) + y \sin(\theta) \quad (4.10)$$

Figure 4.4 demonstrates this more clearly. The total contact deformation is the summation of the central film thickness (h_c) and the material deformation (δ_m) predicted from the dry-Hertzian contact assumption. Conventional dry analysis only accounts for the dry material deformation at the contact.

The extrapolated central film thickness for a line contact, assuming a fully flooded contact inlet, is therefore obtained from [37]:

$$h_c = R_r \left[3.06 G^{*0.56} U^{*0.69} W^{*-0.1} \right] \quad (4.11)$$

where the following dimensionless parameters are used:

$$W^* = \frac{W}{E_r R_r l_a}, U^* = \frac{\eta_0 U}{E_r R_r}, G^* = E_r \alpha \quad (4.12)$$

Comprehensive analytical models [70] [71] account for the tilting and skew of the rolling elements. Skew has the effect of varying the entrainment speed along the length of the roller, and tilt will affect the contact gap. Due to the stiff housing and shaft used in this analysis, the tilt and skew angles are very small. The entraining motion and contact

gap along the contact length can be considered consistent, and a 1-dimensional analysis for EHL film thickness is therefore appropriate [30].

The bearings are modelled with light preload due to mounting interference. In practical applications, preload is applied to prevent skidding and chaotic behaviour due to the emergence of zero stiffness regions [72]. In contrast, excessive preload can lead to frictional power loss and wear. Assuming pure rolling, the speed of entraining motion is given by [73] [74]:

$$u = \frac{R\omega}{r} \left(\frac{(R+2r)}{(R+r)} \right) \quad (4.13)$$

Due to the dependency of load on film thickness, an iterative approach is performed to calculate the contact force. Convergence criteria for the EHL film must be met at each time step of the simulation before the bearing forces are returned to the system level model and the equations of motion are solved:

$$\frac{h_c^m - h_c^{m-1}}{h_c^{m-1}} \leq 0.001 \quad (4.14)$$

where m represents the iteration number.

Individual roller-race contact forces are calculated based on the contact deformation. In the case of a rolling element, a cylindrical body of finite length, the contact problem is non-Hertzian. The surfaces cannot be modelled as locally quadratic due to the presence of crowned (rounded) edges [75]. The most widely used technique to calculate the force-deflection relationship is the contact slicing technique. Whilst this does not reflect edge stress concentrations, these stresses are only distributed over a small area and hence can be neglected for the purpose of force equilibrium [76]. In general, this technique is favoured for its simplicity, speed, and sufficient accuracy. The contact slicing technique employed in this study was developed by Andreason [14] for modelling these non-Hertzian line contacts.

Modelling the roller-race contacts as a line contact between a cylindrical roller and a flat surface, Lundberg's [66] expression between contact force per unit length (w) and deformation (δ) was used.

$$\frac{\delta}{l_a} = \frac{2w}{\pi E_r l_a} \ln \frac{\pi E_r l_a}{w} \quad (4.15)$$

where E_r is the equivalent elastic modulus of the two materials and l_a is the active length of the roller. This assumes that the pressure distribution is uniform along the length of the contact, and elliptical across it. This neglects side leakage along the contact

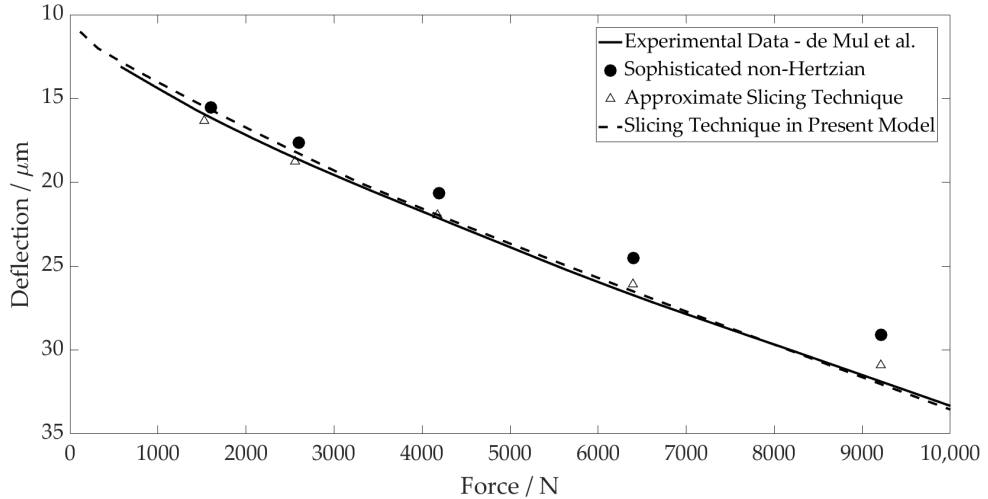


Figure 4.5 Contact level validation.

(x_c) due to the contact dimensions in this direction being much larger than dimensions across it (y_c). This is valid apart from the small regions at the edges of the contact.

From Equation 4.15, contact forces per unit length of an individual slice along the roller-race contact can be calculated. This is valid if there is no separation of the bodies, i.e., the contact deformation does not become negative ($\delta_k > 0$).

$$w_s = \pi E_r l_s \left(\frac{0.5 \delta_s}{7.358 l_s} \right)^{1.11} \quad (4.16)$$

where s represents the slice number, and l represents the slice length.

The application of the slicing technique was validated against open literature. de Mul et al. [16] compared results obtained from an experimental rig with numerical results calculated using both the approximate slicing technique and the sophisticated non-Hertzian technique [77]. By replicating the geometry of the test bearing used in their analysis, the application of Andreadson's slicing technique used for this analysis was validated with good agreement (see Figure 4.5). This method is a much faster way of calculating contact load and moment than more sophisticated methods by de Mul, yet still maintains high accuracy.

The total contact load W and moment T are obtained by summing the contributions from all loaded slices:

$$W = \sum_s w_s l_s \quad (4.17)$$

$$T = \sum_s w_s l_s x_{c,s} \quad (4.18)$$

with $x_{c,s}$ being the distance to the centre of each slice in the conjunction coordinate system. It is assumed that total contact deflection is shared equally between the inner and outer races despite slight differences in contact geometry. The entrainment velocity is equal at each contact, which is the governing parameter for the lubricated contact force differences.

Experimental measurements show that the damping of a rolling element bearing arises from multiple sources [57], including:

1. Lubricant film damping at the contacts.
2. Material damping due to Hertzian deformations.
3. Interface damping between assembled components

These measurements show that damping decreases with rotational speed, tending towards a constant value. Sopanen and Mikkola [61] summarize the findings of Mitsuya et al. [78] and Aini et al. [60], concluding that the film damping is moderate. The linearized viscous damping method adopted in their study is therefore also adopted here. The damping force for each roller is obtained as a factor of the contact stiffness and contact penetration velocity [79]. This is defined as:

$$|F_d| = -f_{\text{damp}} K_c \dot{q} \quad (4.19)$$

where K_c is the contact stiffness, and the damping factor, f_{damp} , is in the range of $(0.25 - 2.5) \times 10^{-5}$ as reported by [79].

At each time step of the analysis, these calculations are performed for each individual roller in the complement. The total bearing force acting on the inner race is solved by splitting the total contact force on each roller into its components and summing their contributions.

$$f_{z,i}^* = \sum_N W \cos(\theta) - \sum_N F_d \cos(\theta) \quad (4.20)$$

$$f_{y,i}^* = \sum_N W \sin(\theta) - \sum_N F_d \sin(\theta) \quad (4.21)$$

Due to the bearing preload, contact is maintained throughout the rollers' orbit; hence no emerging clearances are modelled in the lubricated analysis. The contact separation is also unaffected by rolling element centrifugal forces, which are negligible when compared to the contribution of the dynamic load and the EHL film in this study. These have therefore been neglected.

Table 4.1 Cylindrical Roller Bearing Specification

Parameter	Value
Inner race bore diameter	25 mm
Pitch diameter	60 mm
Roller diameter	8.8 mm
Roller length	15 mm
Number of rollers	17
Radial interference	2 μm

Table 4.2 Bearing Rheological Properties

Parameter	Value
Pressure Viscosity Coefficient (α)	$2.1 \times 10^{-8} \text{ Pa}^{-1}$
Atmospheric lubricant dynamic viscosity	0.08 Pa.s
Lubricant inlet density (ρ_0)	833.8 $\text{kg} \cdot \text{m}^{-3}$
Modulus of elasticity of contacting solids	210 GPa
Poisson's ratio of contacting solids	0.3

Surface measurements of the rollers used in this analysis were taken using an Alicona InfiniteFocus Variation Microscope. The composite surface roughness value of a roller and inner race was calculated to be 91.3 nm. This gives a lambda value of 5.88 for the thinnest EHL film at 1000 rpm. Asperity interaction is not considered as the EHL film fully supports the load. Due to the pure rolling and zero sliding assumption, friction at the contacts is therefore neglected and the analysis is performed under isothermal conditions.

The bearing geometry is detailed in Table 4.1. Rheological and material properties are detailed in Table 4.2, representing ambient operating conditions in an individual hub-motor transmission.

4.4.2 Representative Excitation Methodology

The system level model is decomposed, with excitation forces calculated externally before application within the model. A separate electrified transmission model is used

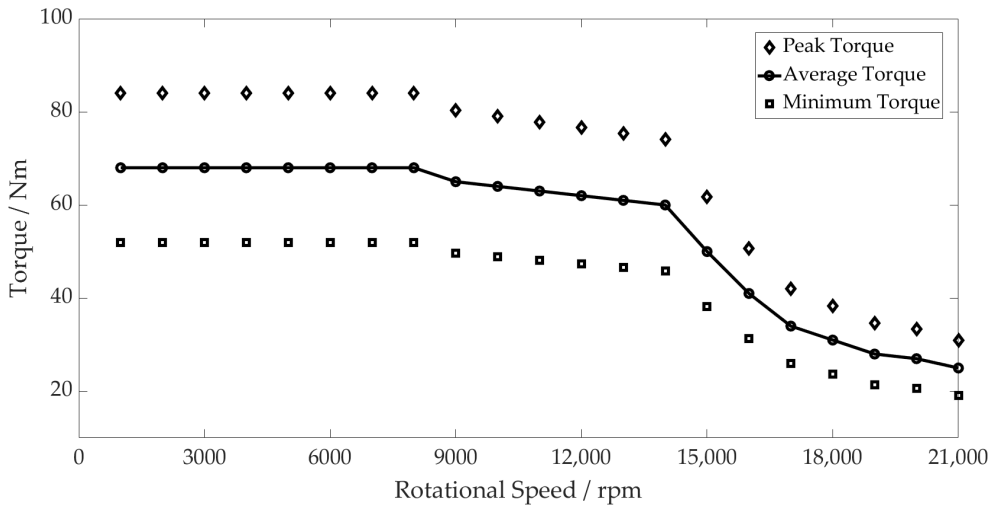


Figure 4.6 PMSM torque profile and maximum and minimum torque fluctuation.

to generate realistic excitation forces and torques from a spur gear pair and a permanent magnetic synchronous motor (PMSM). This system represents the first stage of an electric hub motor used in automotive applications.

Radial and tangential gear pair forces at the pinion centre, as well as torque fluctuations of the electric motor are extracted to be used as inputs to the system level model. These are applied as external forces to the shaft, f^a , from Equation 4.8. All bodies in this separate system were modelled as rigid, so that structural excitation forces did not contribute to the resultant forces at the pinion.

The motor has a peak torque of 68 Nm, and a maximum operating speed of 21 000 rpm. The torque transfer through the gear pair reduces as the speed increases due to the torque profile of the PMSM, as shown in Figure 4.6. Stator tooth forces from the PMSM are neglected in the model due to their minimal contribution to lateral forces once resolved. For input to the model, the radial and normal forces are simplified by adopting sinusoidal inputs of the same magnitude and frequency of the gear pair at different speeds. The torque ripple from the motor is simplified using the same method.

4.5 Results and Discussion

A quasi-dynamic speed sweep has been performed from 1000 to 21 000 rpm. The simulations are performed every 1000 rpm, refined to 250 rpm intervals throughout a period of system resonance between 12 000 rpm and 14 000 rpm. The operating envelopes are generated by plotting the maximum and minimum values from the steady-state signals at each speed interval. The conjunction level results are obtained from an

Table 4.3 Pinion Geometry

Parameter	Value
Number of teeth 17	
Normal module	0.004 <i>m</i>
Normal pressure angle	20 °
Helix angle at pitch circle	0 °
Active tip diameter	0.076 <i>m</i>
Active root diameter	0.065 <i>m</i>
Width	0.035 <i>m</i>

Table 4.4 Gear Geometry

Parameter	Value
Number of teeth	51
Normal module	0.004 <i>m</i>
Normal pressure angle	20 °
Helix angle at pitch circle	0 °
Active tip diameter	0.212 <i>m</i>
Active root diameter	0.202 <i>m</i>
Width	0.030 <i>m</i>

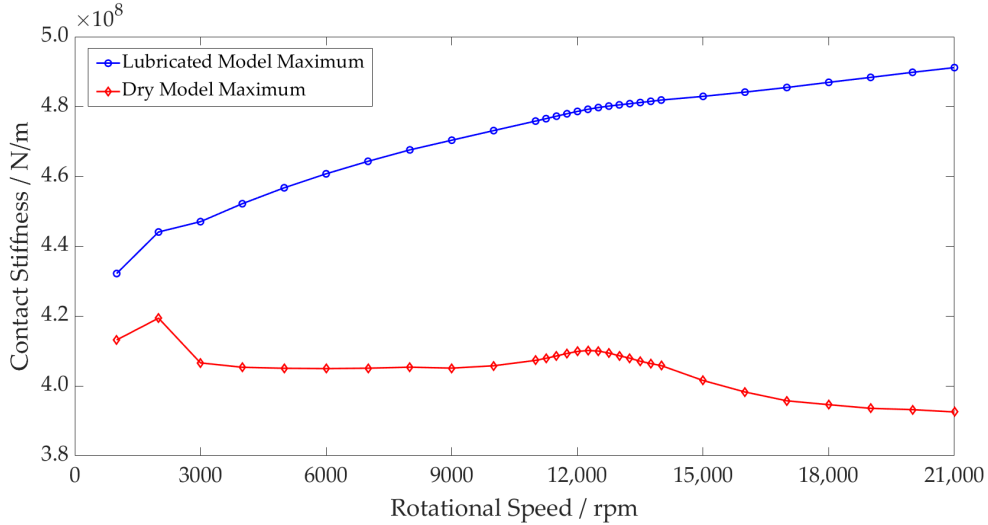


Figure 4.7 Rolling element contact stiffness - Dry vs lubricated maximum values.

individual roller and its contact with the inner raceway. The component and system level results are taken from the geometric centre of the inner bearing race, corresponding to the bearing seat on the shaft. The following figures represent results in the y-direction, the largest component of excitation due to the tangential force from the gear meshing.

The contact level results (Figure 4.7) show a difference in the contact stiffness between the dry and lubricated models. The dry model follows the torque profile of the motor, with stiffness decreasing as the contact forces reduce. The period of resonance leads to the larger amplitude excitation of the shaft, resulting in an increase in the contact stiffness due to the force-deflection non-linearity. The lubricated model, however, shows an increase in the contact stiffness throughout the speed sweep. This is due to the higher levels of deformation at the contact as the lubricant is entrained, which increases with the shaft rotational velocity. This behaviour was experimentally observed by Dietl, concluding that the oil-wedge between the rolling elements and raceways reduces the internal clearance of the bearing and increases its stiffness [57]. The contact stiffness in the lubricated bearing model under the same operating conditions is therefore 24.9% greater at 21 000 rpm.

The peak contact force has been compared between both models. The percentage increase between the dry and lubricated models is shown in Figure 4.8. This more clearly shows the disparity between both models at the contact, with the largest difference being 9.6 times at maximum speed. During resonance, the inner race force reaches a peak of 1514 N, resulting in surface deformation magnitudes of 0.92 μm and 3.81 μm at the dry and lubricated conjunctions, respectively. As noted in previous works [15], higher loads lead to a greater surface deformation to the film thickness ratio, causing the percentage

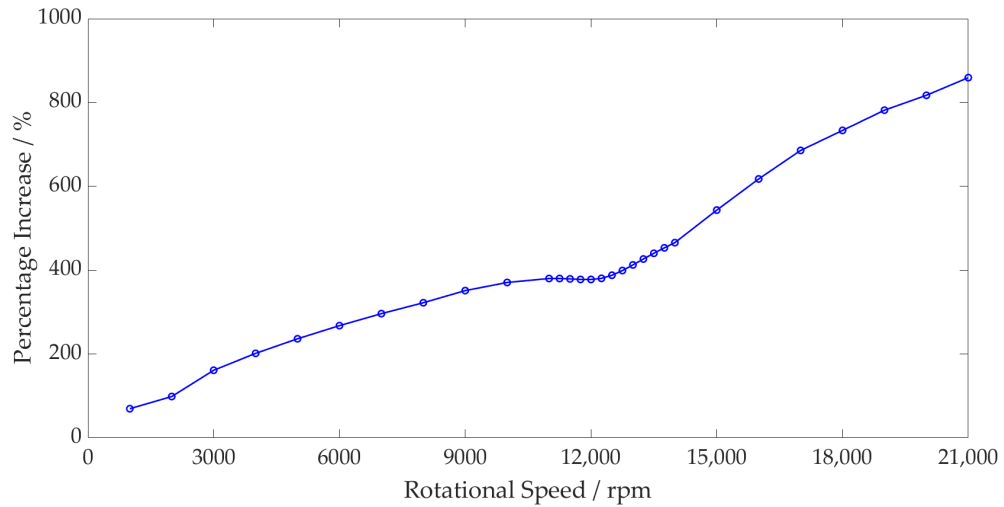


Figure 4.8 Rolling element contact force - Dry vs lubricated percentage increase.

difference between the dry and lubricated models to reduce. Once the loads reduce as the speed increases, the percentage increase continues to rise.

The total bearing stiffness is a combination of all contact stiffnesses between the elements and raceways. These contact stiffnesses vary non-linearly with force, resulting in the total bearing stiffness varying accordingly. For the dry model, this is clearly demonstrated, with the greater total bearing stiffness at the peak of the resonance due to the greater bearing forces (see Figure 4.9). This does not, however, capture the change of the total bearing stiffness with speed; the average bearing stiffness does not change. The lubricated bearing is not only stiffer than the dry bearing, but this stiffness also increases with speed. This is shown in Figure 4.9 by the non-linear increase in the average lubricated bearing stiffness values compared to the constant values for the dry model. The combination of these two factors leads to the lubricated model having a 16.6% greater maximum total bearing stiffness at 21 000 rpm than the dry model.

Due to the greater total stiffness of the bearing, the shaft displacement of the lubricated model is lower both on average and peak to peak for the same applied force in comparison to the dry model (see Figure 4.10). Through the period of resonance, the large inner race forces result in the roller–race separation of the unloaded rollers within the dry model. This leads to greater shaft displacement as the inner race moves into this region of zero stiffness until roller–race contact is made, and a reaction force is established.

Figure 4.11 shows that the acceleration peak of the system resonance occurs at 12 500 rpm (3542 Hz) for the lubricated model as opposed to 12 250 rpm (3470 Hz) for the dry model. This shift in natural frequency indicates a stiffer overall system. The

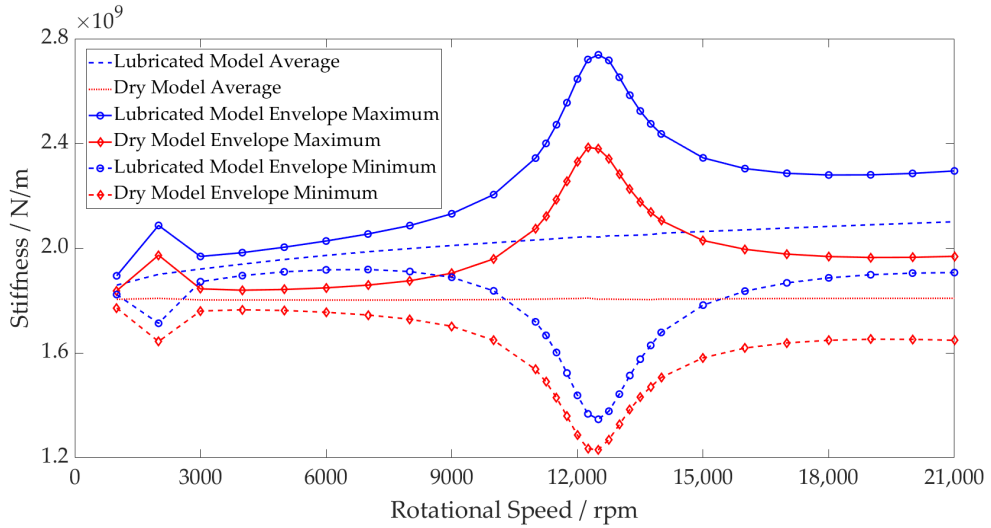


Figure 4.9 Inner race stiffness - Dry vs lubricated operating envelope.

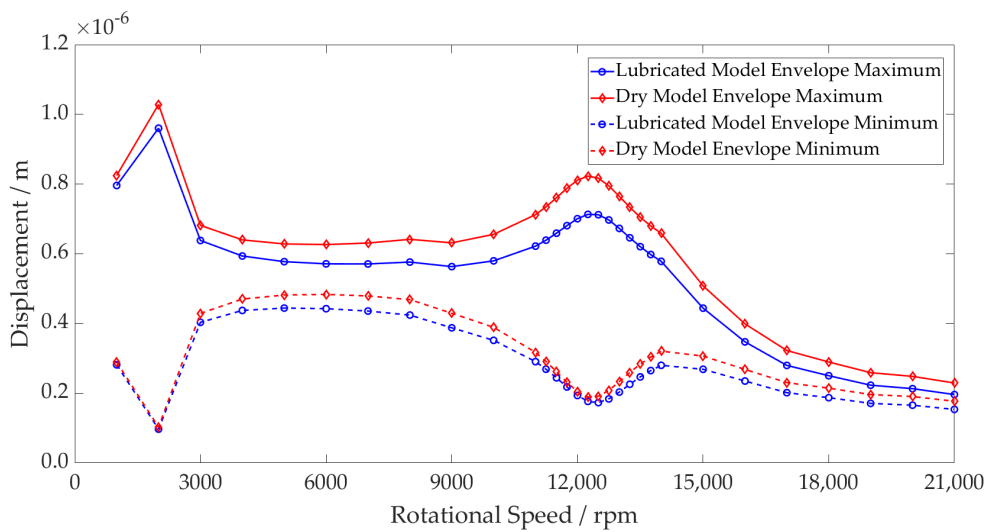


Figure 4.10 Inner race displacement - Dry vs lubricated operating envelope.

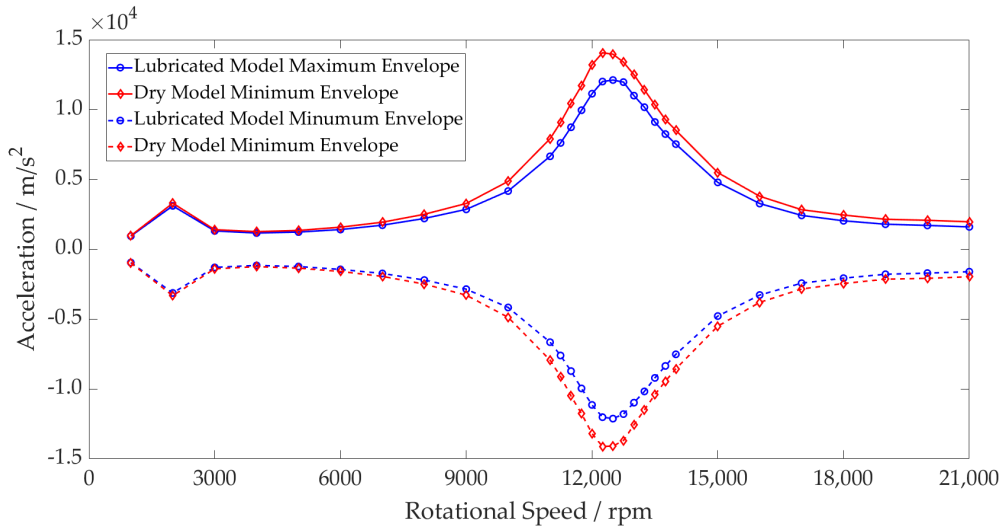


Figure 4.11 Inner race acceleration - Dry vs lubricated operating envelope.

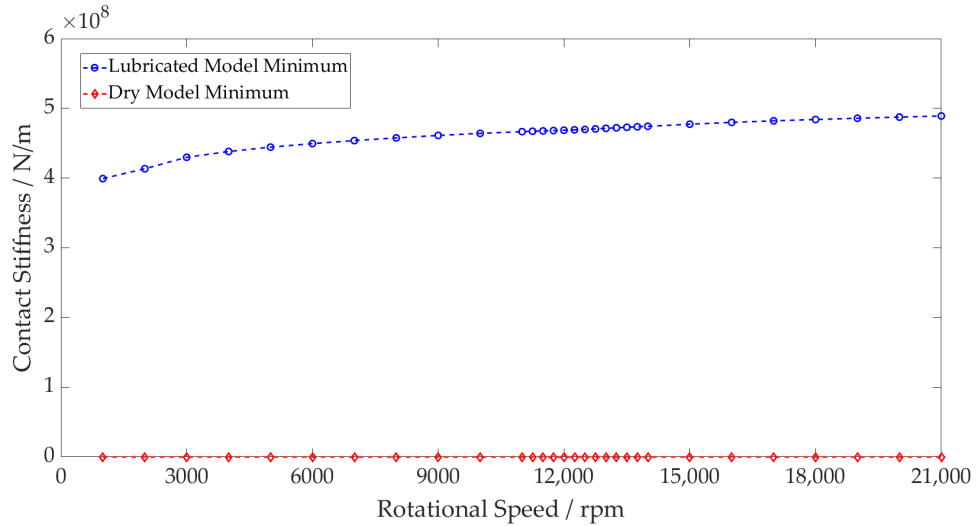


Figure 4.12 Rolling element contact stiffness - Dry vs lubricated minimum values.

magnitude difference between the dry and lubricated models can also be attributed to the unloaded regions of the dry bearing. The contact deformation arising from the loading of the inner race is sufficient to cause the rollers geometrically opposite to become separated from their contacts. Contact is lost between the roller and raceway, leading to zero contact stiffness. The inner race moves into this region until it is reacted by a contact force once again. These regions of zero stiffness are shown in Figure 4.12, where the minimum stiffness of an individual rolling element and raceway contact in the dry model drops to zero due to separation. For the lubricated model, contact is maintained throughout.

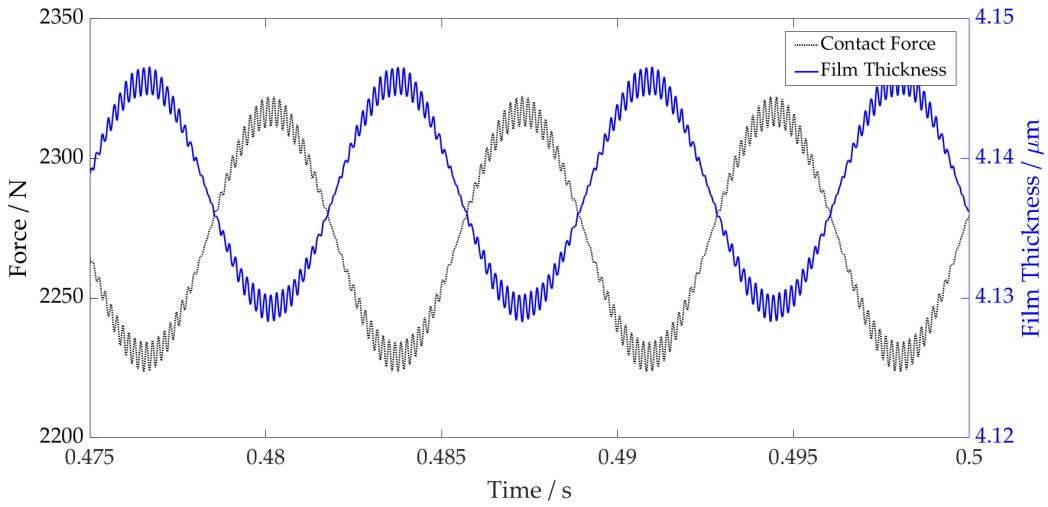


Figure 4.13 Film thickness vs contact force 21 000 rpm.

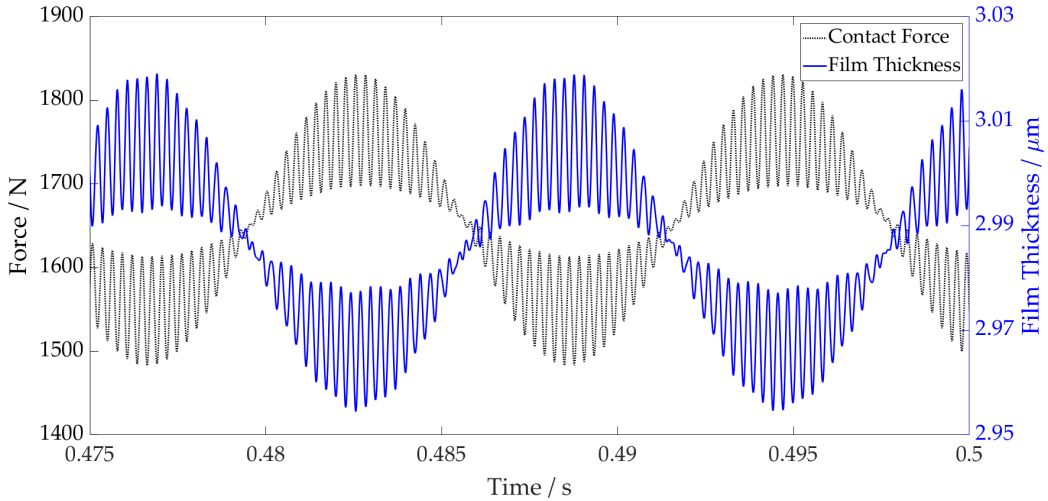


Figure 4.14 Film thickness vs contact force 12 500 rpm.

Analysing the conjunction level results from the lubricated model, the contact force due to the gear mesh frequency is shown superimposed on the ball pass frequency as an individual element passes through the loaded region of the bearings (Figures 4.13 and 4.14). The higher contact forces result in a reduction in the central film thickness, also shown when observing the variation in film thickness for both plots. At 12 500 rpm, the force and film thickness fluctuations are much larger due to the high excitation levels of the shaft during resonance. At 21 000 rpm, even with a much lower torque transfer through the gear pair, the contact forces are greater than at 12 500 rpm. This is due to the contribution of the film enhancing the total contact deflection and hence increasing the contact force.

4.5.1 Conclusions

The new methodology presented has been developed to implement a lubricated bearing model within a flexible system level model. The model implicitly includes the lubricant film at the roller–race contact within the bearing; this is something that has not, to the authors’ knowledge, been reported previously in the open literature. Simulations have been performed up to 21 000 rpm with realistic excitation forces from a first stage reduction gear pair and electric motor. The conjunction level and system level results have been analysed to compare the lubricated and conventional dry-bearing modelling techniques in a flexible multi-body dynamic (FMBD) environment.

Results show that the film thickness reaches $4.1521 \mu\text{m}$ at 21 000 rpm. This leads to 9.6 times greater contact forces and hence 24.9% greater contact stiffness between the dry and lubricated models due to the lubricant entrainment and non-linear Hertzian force–deflection relationship. The contribution of all the rolling elements leads to the lubricated model having a 16.6% greater maximum total bearing stiffness at 21 000 rpm than the dry model. Moreover, this stiffness is shown to increase with speed due to the film thickness increasing with the entrainment velocity; this is something that dry models do not account for.

This increase in the total bearing stiffness leads to a change in the stiffness of the total system. By modelling the shaft as a flexible body, the influence on the natural frequency of the system is seen. The resonant peak at 12 500 rpm shifts 250 rpm higher in the lubricated model, which coincides with the higher frequency excitation from the gear meshing.

Understanding the influence of the roller bearings on the transmission stiffness is of particular importance in automotive applications, and this change shows the effect of the lubricant film on the already complex contact phenomena. Neglecting the effect of the lubricant film can lead to an underestimation of the bearing stiffness, impacting the accuracy of dynamic analyses such as noise, vibration and harshness (NVH) prediction. As transmissions operate at higher speeds with more complex interconnected structures and noise paths, it is important that these behaviours are modelled accurately. Furthermore, underestimation of the contact forces will also lead to a miscalculation of contact pressures, impacting future sub-surface stress and wear analyses for the life predictions of these crucial critical machine elements.

Further developments of this work aim to include more complex rheological phenomena, accounting for thermal and starvation effects at high speeds. Computational efficiency must also be maintained when embedding these models within FMBD environments, due to the iterative nature of the EHL solution.

The presented work establishes the necessity of a multi-physics approach to model the tribology and dynamics of high-speed rolling element bearings. This is essential for future powertrain modelling to ensure accurate component and system level behaviour.

Chapter 5

Artificial Neural Networks for EHL Film Thickness Predictions

5.1 Abstract

Tribodynamic modelling generally employs analytical equations for the prediction of film thickness in elastohydrodynamic contacts; chosen due to their timely solution. Whilst computationally efficient, these do not achieve the accuracy of the full numerical solution outside the bounds of the data used to generate the analytical equations. In the context of dynamic simulation, a full numerical solution at each time step of a system level model would, however, yield excessive computation time. This has led to the emerging use of data driven solutions, such as machine learning, in the field of tribology. These can achieve accuracy much closer to the numerical solution, whilst significantly improving computational time.

This chapter details the development of an ANN for prediction of central film thickness at the roller-race conjunction. ANNs are trained using data generated by numerical solution, with the data set constrained to realistic operating conditions using the Greenwood regimes of lubrication. Multiple ANNs are compared to find the optimum structure, accounting for training time and accuracy.

This workflow introduces the application of Artificial Neural Networks (ANNs) a form of Machine Learning (ML) algorithm, to predict the central film thickness at the roller-race conjunction. The performance of ANNs will be compared with analytical equations and numerical solutions, assessing the suitability of its implicit application within FMBD environments. The aim is to improve the accuracy of the central film thickness estimation, whilst maintaining a timely solution in the context of a full dynamic solution.

5.2 Introduction

Two main approaches exist for determination of the complex non-linear problem of film thickness in lubricated contacts. The first approach involves employing numerical methods [80], where systems of partial differential equations are formulated to describe the state of the contact and then solved iteratively [81]. While this method yields accurate results and is applicable to a wide range of operating conditions, it is computationally intensive due to its iterative nature. The second approach involves developing regressed analytical equations from experimental or numerical studies which can be used for specific lubrication regimes. These equations offer quick estimates of key parameters, such as central [37] and minimum film thickness [82]. However, whilst more computationally efficient than full numerical solutions, this approach has limitations. The applicability of regressed equations is often limited to the range of data used for their development, resulting in reduced accuracy due to simplification. There is also a requirement for extensive effort in collecting experimental or numerical data to develop them. The implementation of ANNs within tribology is one Although ANNs lack the physical understanding provided by numerical solutions, they offer nearly real-time performance comparable to analytical solutions while benefiting from the accuracy of numerical methods [83]. To ensure the validity of the ANN, a methodology is suggested for training it within a range consistent with the numerical solver.

The most common ML algorithm used in tribological applications are ANNs. The first utilization of these were in the 1990s [84]. Ezugwu et al. implemented and ANN for wear rate and hence life predictions of ceramic cutting tools [85]. Their model had an 80% success rate in predicting the failure mechanism of the tools. Rutherford et al. [86] and Jones et al. [87] developed on this success, focussing on wear rate predictions for coating materials and mechanical systems respectively. Jones et al. were able to achieve 90% wear rate prediction accuracy by optimising their ANN architecture using R^2 coefficients as a performance indicator. Similar studies were then conducted in the domain of friction and wear rate of composite materials [88] [89] [90], as well as tools steels [91].

Whilst the friction in the aforementioned studies was modelled under dry conditions, friction in lubricated contacts has also been modelled using ANNs. Bhaumik et al. [92] used ANNs to develop a new lubricant with multiple friction modifiers (FM), considering load, speed and FM concentration as input variables, with the target output being coefficient of friction. A similar methodology was employed to develop biodegradable oils [92], validating both sets of studies using pin-on-disc friction measurements. Traction coefficients under various thermal-elastohydrodynamic operating conditions have also

been investigated [83], with the authors noting fast predictions of results with excellent accuracy (lower than 3% error in most cases). Further lubricated studies involving relative viscosity predictions [93] [94] have achieved deviation margins of 1.5% and 0.07% respectively, substantially lower than empirical correlations.

Many further studies have been performed in the field of wear in manufacturing processes [95]. Previous studies had multiple input variables to the ANNs (speed, load, temperature, shear rate). For specific manufacturing processes with particular lubricant-surface combinations, the input data array can be drastically reduced to process-specific variables such as load, speed, and vibration. This approach was taken to investigate flank wear in drilling [96] and surface roughness of machined parts [97]. By reducing the number of input parameters, less training data was required to achieve good fits.

The studies referenced ([85] - [97]) all shared a common approach of utilizing experimental data to train the ANNs. Whilst experimental data benefits from the lack of assumptions in numerical models, there is the limitation of high costs and time required for generating large datasets. Consequently, the training datasets for the ANN were limited to approximately one hundred points [90] [89], or fewer [85] [86], with the largest (216 points) utilised by Cavaleri et al. [91]. Since the training process optimizes the ability of the ANN to interpolate between data points for varying input conditions, a greater number of training points is advantageous. It was noted by Ezugwu et al. [85] and Zhang et al. [90] that a significant improvement in ANN fit was achieved with a larger training data set. This is an observation shared across several studies and scientific applications [98].

An alternative method of achieving large data sets without the high financial and time cost of experimentation is to use numerical modelling. Wang et al. [99] identified the need for larger training sets in the field of tribology. Their prediction for maximum Hertzian pressure in thermohydrodynamic contacts utilised a training data set that was generated using Reynolds equation. Whilst limited to the accuracy of the numerical model, the ANN benefits from much faster computation time. It crucially also allows for larger data sets to be generated that can cover a much larger range of input data; a requirement for implementation within dynamic models.

The Reynolds boundary value problem has also been solved using Physics Informed Neural Networks (PINN) by Almqvist [100]. The study was not to improve on the numerical accuracy or efficiency of standard finite-difference based methods, rather to present an application of PINN in the field of tribology. Error analysis showed good agreement with the analytical solution, however further work is needed to improve the solving efficiency. Since the ANN is to be implicitly embedded within a dynamic simulation, efficiency is critical. Data driven solutions are therefore preferable. Marian

et al. [1] demonstrated for the first time the generation of EHL film thickness data using a Finite Element Method (FEM) to train an ANN. The ANNs could predict locally-resolved film thickness across the contact domain 25-times faster than FE-based EHL simulations.

It is now known that data-driven solutions, such as machine learning, can greatly enhance the computational efficiency of tribo-dynamic simulations without sacrificing accuracy. In this study, artificial neural networks (ANNs) were trained using numerical solutions constrained by lubrication regimes to ensure the quality of the training data set.

5.3 Artificial Neural Network Fundamentals

Artificial intelligence (AI) refers to machines that exhibit human cognitive skills. They are a set of algorithms which allow machines to learn and problem solve in a manner inspired by the neurons in the human brain. Machine learning (ML), a subset of AI, allow systems to perform tasks without explicit programming. These algorithms analyse data and autonomously adapt to enhance their task performance, resembling the human ability to learn from experience.

ML encompasses two primary algorithm types: supervised learning and unsupervised learning. In supervised learning, the program receives both input data and target outputs. The programmer guides the algorithm by demonstrating the correct output. The program can then compare its own outputs to the desired ones, refining itself through training. For example, by training on images and corresponding object names, the program can subsequently recognize objects in new images unassisted. Unsupervised learning algorithms operate without target outputs, exploring input data for patterns independently. These algorithms analyse the input's feature space and cluster the data accordingly. When presented with new data, the program assigns it to an existing cluster based on its location in the feature space.

ML algorithms can also be classified based on the type of output they produce. They can be utilized for classification problems, where data points are assigned to discrete categories, or regression problems, involving approximating continuous output functions. Classification tasks can be accomplished through supervised learning algorithms using logistic regression, approximating step functions with discrete outputs. Unsupervised learning algorithms achieve classification through clustering, an example of which being character recognition and speech processing,image and speech processing.

Supervised ML algorithms have the advantage of approximating continuous output functions, making them suitable for complex nonlinear relationships between inputs and outputs. By comparing their outputs with target values during training, they act as

universal function approximators. This characteristic proves particularly valuable for applications such as tribological simulation, where the interaction between contacting surfaces requires efficient solvers. Notably, supervised linear regression ML algorithms offer effective solutions in this domain.

5.3.1 Numerical EHL Methodology

5.3.2 Artificial Neural Network Methodology

An Artificial Neural Network (ANN) is a computational model which is inspired by the neural networks present in the human brain. It is a subset of machine learning.

ANNs are made up of a set of interconnected nodes that have the ability to adapt to input data for the purpose of solving complex non-linear functions. The nodes, known as artificial neurons, are organized into layers. The three main types of layers are shown in FIGURE 1, these are: Input layer; Hidden layer(s) and Output layer. The adaptation is performed using weighted connections, that connect each neuron layer. These weightings can be adapted during the learning process, and determine the strength of the connections between neurons.

The generalized structure of an ANN comprises several layers which contain neurons inside. Equation 5.1 describes the relationship between each neuron, i , of each layer, j ,

$$u_i^{j,k} = f_j \left(\sum_{\forall m} W_i^{j,k} \cdot x_m + b_i^{j,k} \right) \quad (5.1)$$

5.3.3 ANN Training Process

The learning process of an ANN involves training a set of input data which correspond to known output values. A common technique for this is back propagation, where the connection weightings in the network are adjusted such that the error between the predicted and the actual output are minimized. The goal of this training is to minimize the error, and to improve the ability of the network to generalize and make accurate predictions for new, unseen data.

As the structural complexity of ANNs increases, the training time increases due to the greater number of neurons and layers. Implementations of ANN in the field of tribology, specifically film thickness predictions, are typically limited to between one and three hidden layers [101].

MATLAB 2022a was used for the development of the ANNs.

The training data set for the ANN was obtained from numerical models. This decision was made due to the size of the database required for training, and the timely

and relatively low resource-intensive nature to generate this. It is worth noting that training data could also be obtained from experimental work, which further enhances the applicability of this approach for future studies.

The structure of the ANN is described in the following format, as per [90]:

$$N_{in} - [N_{h1} - N_{h2} - N_{h3}]_t - N_{out} \quad (5.2)$$

The number of neurons in each layer is denoted by the symbol N , with the input and output layers indicated by the subscripts *in* and *out*, respectively. Subscripts $h1$, $h2$, and $h3$ denote the hidden layers, with t being the total number of hidden layers.

To evaluate the performance of different ANN structures, a sensitivity study was performed. For this study, the input range for each variation was the same, and the following was varied:

- Number of initial training data points: 600 to 5000.
- Number of hidden layers: 1 to 4
- Number of neurons: 10 to 20
- Type of activation function:
 - Hyperbolic tangent
 - Logistic sigmoid
 - Rectilinear

Selection of the final structure for suitability analysis was based on total training time, coefficient of determination (R^2), and the potential for the ANN to be overtrained. Overtraining is the phenomenon whereby an ANN becomes too specialised at learning the training data, and as a result performs poorly with new, unseen data. This occurs when the network extensively adjusts its internal parameters to fit noise or outliers in the training set.

Numeric Database Construction

Due to the large design space covered by the high number and range of input parameters, a robust sampling technique needs to be chosen to create the training data set. In traditional random sampling, each of the parameters is randomly sampled within its defined range. This may lead to insufficient coverage of the parameter space and simple bias, as this method has no "memory" of points already selected.

The Latin Hypercube Sampling (LHS) method was utilised by Marian et al. [1], and was chosen for this study. LHS is a statistical method commonly used in experimental design and statistical analysis to efficiently sample a high-dimensional parameter space. It generates a near-random sample of parameter values from multi-dimensional distributions. The sample points are distributed such that the design space is filled as evenly as possible, with information from nearly all regions being covered. This ensures lower computational effort required for ANN training, despite the high number of input variables and value ranges.

LHS is based on the concept of Latin hypercube design (LHD). In LHD, the parameter space is divided into equal intervals along each dimension. Each interval is then randomly assigned to a unique position within its corresponding dimension. The process results in a matrix, where each row represents a combination of parameter values. Contrary to the random sampling method, LHD guarantees that only one sample is taken from each row, ensuring a diverse and representative set of samples.

The LHD is a $n_s \times n_f$ matrix, where n_s and n_f represent the number of simulations the number of factors respectively. LHS enhances LHD by introducing a randomization component. The randomly selected samples within each interval are shuffled, ensuring that samples are not biased by the order of selection.

LHS elements are generated by subtracting a random number between zero and one $Z_r[0, 1]$ from each LHD element $x_{ij,LHD}$. This is then divided by the number of test points [102]:

$$x_{ij,LHS} = \frac{x_{ij,LHD} - Z_r[0, 1]}{n_s} \quad (5.3)$$

This equation rescales the LHD values to a range between 0 and 1. By subtracting a random number between 0 and 1 and dividing by the total number of sample points, the resulting Latin hypercube samples are spread evenly across the interval (0,1) for each parameter. This is important, because it allows the Latin hypercube samples to be easily transformed to any desired range or distribution.

The quality of the test field (freedom of correlation and uniform distribution) can be assessed based on the distances between data points [103]. The MaxiMin criterion in MATLAB's Statistics and Machine Learning toolbox was used to optimise the LHS. This maximises the the minimum distance between individual test points such that the LHS test field is uniformly distributed:

$$\text{MaxiMin} = \left[\sum_{1 \leq i < j \leq n_1} d(x_i, x_j)^{-\xi} \right]^{-\frac{1}{\xi}} \quad (5.4)$$

where d represents all distances in the test field, and subscripts i and j are indexes for the parameter and sample point respectively. ξ represents the application dependant factor which determines the degree of importance assigned to the distances [102].

5.4 Machine Learning Methodologies

Various ML regression methods exists, including Support Vector Machines (SVM), Gaussian Process Regression (GPR), and Artificial Neural Networks (ANNs). To select an appropriate method for EHL film thickness predictions, a literature study on the merits of each methodology was conducted.

1. SVM: Used for both classification and regression tasks. The main aim SVM is to find a hyperplane that separates different classes, or approximates a regression function while maximising the margin between the data points and the decision boundary. SVM uses a kernel function to map the input data into a high-dimensional feature space. Support vector regression (SVR) is based on the principles of SVM. SVR aims to find a regression function that maximises the margin between the predicted out puts and a specified error threshold.

Advantages

- It is robust against overfitting due to the use of the margin-maximisation principle.
- Different kernel functions can be used to obtain good results with both linearly separable and non-linearly separable data.
- Handles datasets with high dimensionality

Disadvantages

- Can be computationally expensive for large data sets
- Careful tuning is required for the choice of kernel function and its parameters.
- Interpretation of the SVM model is often challenging as underlying relationships between input variables and the output are not explicitly identified.

2. GPR

3. ANN

Marian et. al conducted a study for film thickness distribution

SECTION ON LHS AND PARAMETER STUDY COMPARISON (ANI)

The performance of ANNs is heavily reliant upon the quality of the data set provided for training. To construct a training database, Marian et al. [1] utilised a Finite Element Method (FEM) solver. The database covered a very large range of lubricant and material properties for relatively low entrainment speed conditions ($< 0.4 \text{ m/s}$ for the 2D line contact studies). The resulting contact conditions when some combinations of these parameters were used, exceeded realistic conditions within common machine elements, including bearings. Since the film thickness evaluation is required for the EHL contact of roller bearings, the input data set for this study requires constraining to improve validity.

A method to constrain the input parameter combination to realistic machine element operating points was devised. The Greenwood Regime chart [104] was used for this purpose. The regions of the chart, as shown in Fig.XXXX, are:

- Isoviscous Rigid (IR)
- Isoviscous Elastic (IE)
- Piezoviscous Rigid (PR)
- Piezoviscous Elastic (PE)

The bounds indicate the transition between the lubrication regimes, which are classified based on material, rheological and geometric properties. To find which regime a contact is operating within, the dimensionless elasticity (G_e) and viscosity (G_v) parameters can be calculated:

$$G_e = \left(\frac{\alpha^2 W_i^3}{\eta_0 u R_r^2} \right)^{\frac{1}{2}} \quad (5.5)$$

$$G_v = \left(\frac{W_i^2}{\eta_0 u E_r R_r} \right)^{\frac{1}{2}} \quad (5.6)$$

The PE region signifies contact pressures high enough to elastically deform the material and increase the viscosity of the lubricant; hence an EHL contact. The IR region relates to the hydrodynamic regime of lubrication, where the contact is lightly loaded and the surfaces do not deform and viscosity does not increase. Since these investigations are focussed on improving the EHL film thickness solution, the training data set was required to fall within the PE region of the Greenwood plot. The initial range of each parameter is shown in Table 5.1. The training data set was then generated

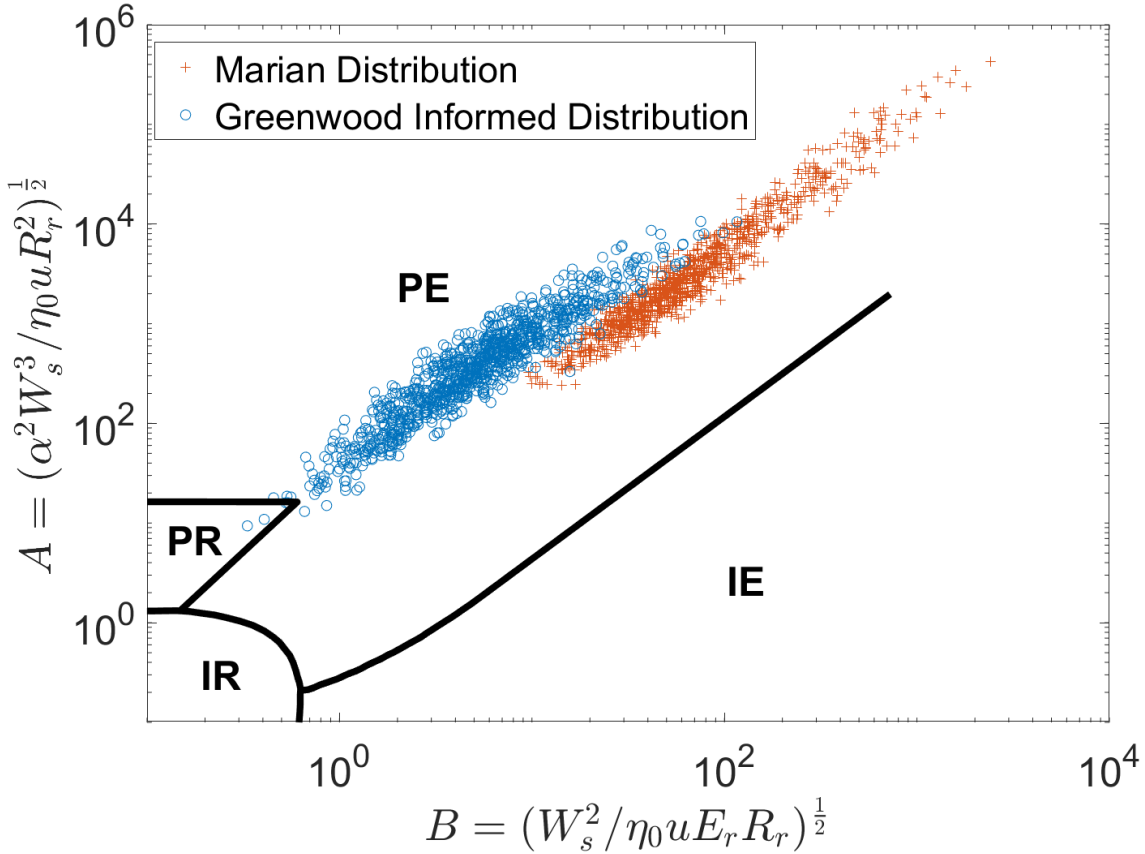


Figure 5.1 Greenwood informed training data vs Marian et al. [1].

using these limits. The input data was then constrained further to ensure Hertzian pressures fell between 300 MPa and below 3.5 GPa, as well as redistributing any points that fell outside of the PE and PR regions. HOW IS THIS DONE. SHOW BEFORE AND AFTER PLOTS AND INFLUENCE ON TRAINING QUALITY?

CHECK THIS The numerical solution database can also benefit from explicit parallelisation ie. use of multiple computational cores of the CPU. When using MBD solvers implicitly it is not possible to use explicit parallelisation since a particular time step is dependent on the present timestep as well as on data of the same timestep. The ANN functionality in turn can be embedded with an implicit MBD computation environment to significantly improve the computation times without the need of explicit parallelisation despite benefitting from it indirectly.

ANN Structure

Normalization of the input and target parameters is first performed using min-max normalisation function:

Table 5.1 Range of ANN film thickness calculation parameters

Parameter	Unit	Minimum	Maximum
Load	N	150	5000
Entraining Velocity	m/s	0.6	30
Reduced Radius	m	0.0001	0.02
Reduced Elastic Modulus	GPa	200	250
Pressure-Viscosity Coefficient	GPa ⁻¹	10	30
Reference Viscosity	Pa.s	0.0005	0.1
Maximum Density	kg/m ³	7750	8050
Poisson's Ratio	—	0.3	0.35
Contact Length	m	0.001	0.050

$$\tilde{x} = \frac{x - x_{\min}}{x_{\max} - x_{\min}}(u - l) + u \quad (5.7)$$

Where u , and l represent the upper and lower normalized unit values of 1 , and -1 respectively. The dimensional target input value is denoted by x , and the final normalised input or output parameter of the ANN is denoted by \tilde{x} . In order to dimensionalise the output layer, x_{\max}, x_{\min} must be stored as a variable.

The dataset is divided into three sets: the training set, the validation set, and the test set, each containing 70 %, 15 % and 15 % of the training data respectively:

1. Training Set: The training set is the portion of the dataset used to train the ANN, containing the input data and the corresponding output data. As aforementioned, the ANN adjusts the internal parameters based on this data to learn the underlying patterns and relationships.
2. Validation Set: The validation set is used to tune the performance of the ANN during the training process. It is an independent dataset that the network has not seen before, allowing for the evaluation of its generalization capabilities. The network's performance on the validation set is monitored during training to make decisions on adjusting hyperparameters (number of hidden layers, neurons per hidden layer, activation functions etc.) or stopping the training process to prevent overfitting.

3. Test Set: The test set is a completely independent dataset that is not used during training or validation. It is used to assess the final performance and generalization ability of the trained ANN. By evaluating the network on unseen data, the test set provides an unbiased estimate of the model's performance in actual use.

A limit of 1000 epochs was also implemented. This limits the ANN to 1000 full iterations through the entire training set during training. This was found to be sufficient to improve accuracy whilst preventing overfitting of the data.

During back propagation of the ANN, the Mean Squared Error (MSE) was used to evaluate the network's performance:

$$MSE = \frac{1}{N} \sum_{i=1}^N (t_i - y_i)^2 \quad (5.8)$$

The total number of training points being trained, validated or tested is denoted by N .

To assess the goodness of fit of the ANN, the statistical metric R^2 known as the coefficient of determination was used. This measured the proportion of variance in the dependant variable (output film thickness) that is predictable from the input variables (Table 5.1) in the model. This value ranges from 0 to 1, with a higher value indicating the best fit of the model to the data. This was post-processed after training and is calculated as follows [1]:

$$R^2 = 1 - \frac{\sum_{i=1}^N (t_i - y_i)^2}{\sum_{i=1}^N (y_i - \bar{y})^2} \quad (5.9)$$

where t_i and y_i are the target and predicted value respectively. \bar{y} is the mean of the target sample. The numerator of the fraction is the sum of the squares of residuals, which represents that variation in target variable that is not explained by the model. The denominator is the total sum of squares and represents the total variation in the target variable.

Activation functions:

Activation functions are mathematical functions that are applied to the output of each neuron in a layer of the neural network. These introduce non-linearity which allow the network to learn complex input-output relationships. Activation functions help determine the output of a neuron based on the weighted sum of its inputs.

As suggested per [1], suitable activation functions for the hidden layers are as follows:

- Sigmoid (logistic): This function transforms the input values into a range between 0 and 1. It has continuously differentiable smooth S-shaped curve and is given by the following formula [105]:

$$\text{log sig}(x) = \frac{1}{1 + e^{-x}} \quad (5.10)$$

Sigmoid functions are commonly used in the hidden layers of ANNs, however may suffer from the "vanishing gradient" problem where the partial derivative reaches zero [106], leading to slower convergence during training.

- ReLU (Rectified Linear Unit): This function is the most commonly used activation function. It outputs the input value directly if it is positive, and zero otherwise. The mathematical definition is:

$$\text{ReLU} = \begin{cases} x, & x \geq 0 \\ 0, & x \leq 0 \end{cases} \quad (5.11)$$

The gradient is 1 when the neuron is activated, and zero when it is deactivated. This function is computationally efficient and addresses the vanishing gradient problem to an extent [106].

- Tanh (Hyperbolic Tangent): The hyperbolic tangent or tanh function is also commonly used. It is defined as:

$$\tanh(x) = \frac{2}{1 + e^{-2x}} - 1 \quad (5.12)$$

The formulation and behaviour is very similar to sigmoid. It produces values which range from -1 to 1, having a centred mean around zero. Like sigmoid, this also experiences vanishing gradients.

A simple linear activation was used on the output.

The training data size was varied (600, 1000, 2000 and 5000) to observe its effect on the quality of the prediction.

Early stopping and regularisation was used to prevent statistical overfitting during training. Early stopping halts the training process before the model reaches the maximum number of epochs. This is done by monitoring the performance (MSE (Equation 5.8)) of the network against the validation set during training. Once the performance reaches a plateau, or begins to degrade, the training is stopped early. Regularisation adds additional constraints to the learning process. It modifies the performance criteria by accounting

Table 5.2 Roller Bearing Parameters

Parameter	Value
Inner race diameter	31.5 mm
Roller diameter	7.5 mm
Roller length	15 mm
Number of rollers	12
Radial interference	5 μm
Young's modulus	218 GPa
Poisson's ratio	0.3

Table 5.3 Operating Conditions

Parameter	Value
Radial force	2500 N
Rotational velocity	10 000 rpm

for the change in mean square of the network weights and biases (MSW (Eq. 5.13)). By applying an adjustment factor, denoted as γ' , the weights and biases can be reduced during propagation (Eq. 5.14), thus mitigating the risk of overfitting and improving the network's generalization capability.

$$MSW = \frac{1}{N} \sum_{j=1}^N w_j^2 \quad (5.13)$$

$$MSE_{reg} = \gamma' * MSW + (1 - \gamma') * MSE \quad (5.14)$$

Explicit Roller Bearing Implementation

The same FMBD model used in Chapter 4 was used for this study. The shaft was modelled as a rigid body, and loading was purely static in one radial direction to remove the influence of dynamic effects. The shaft is constrained to one rotational and two lateral degrees of freedom. Bearing properties and operating conditions are shown in Table 5.2 and Table 5.3 respectively.

The dynamic model was run explicitly as a dry model, without the influence of the EHL film at the roller-race contacts. The kinematic and dynamic results required for input to the ANN are then extracted at each time step. Results were generated for an individual element completing one complete orbit around the bearing. Extracted results include roller load per unit length, reduced radius of the contact between the roller and inner-race, and the contact entrainment velocity.

The loading pattern is cyclic in nature as the roller enters and exits the most highly loaded region of the bearing, corresponding to the force vector applied to the inner race. Sufficient preload ensures constant contact between elements and raceways so that the regime does not deviate from EHL. The contact reduced radius and entrainment speed do not change throughout the orbit as they are a function of bearing geometry and constant operating speed.

5.5 Results and Discussion

The following data was obtained using consumer grade hardware with the following specifications: Intel® Core™ i7-9750H CPU 6 cores @ 2.60GHz, 32GB RAM; GPU: NVIDIA GeForce GTX 1650.

The same hardware was used for both the full numerical and the ANN solutions to provide performance comparisons and assess the suitability of ANNs for film thickness calculations in FMBD solvers.

ANN Structure and Performance

The 1D EHL model presented in Section 3.2 was used to generate the numerical database for training the ANN. Each numerical solution and hence training point took an average of 5.88 *s*. The construction of the entire database on a single core therefore has a wall time of between 58.8 *min* and 489 *min* for 600 and 5000 points respectively. This wall time is purely for baseline comparisons, and can be significantly improved using parallelisation across multiple cores.

A parameter study was conducted to determine the optimal structure for the ANN. Over 500 different structures were tested using the same input data. This involved varying the hyperparameters: the number of hidden layers varied from one to four, and the number of neurons from ten to twenty. The three aforementioned activation functions were explored in different hidden layer configurations. This included a combination of hyperbolic tangent in the hidden layers, with the final layer utilizing a logistic tangent

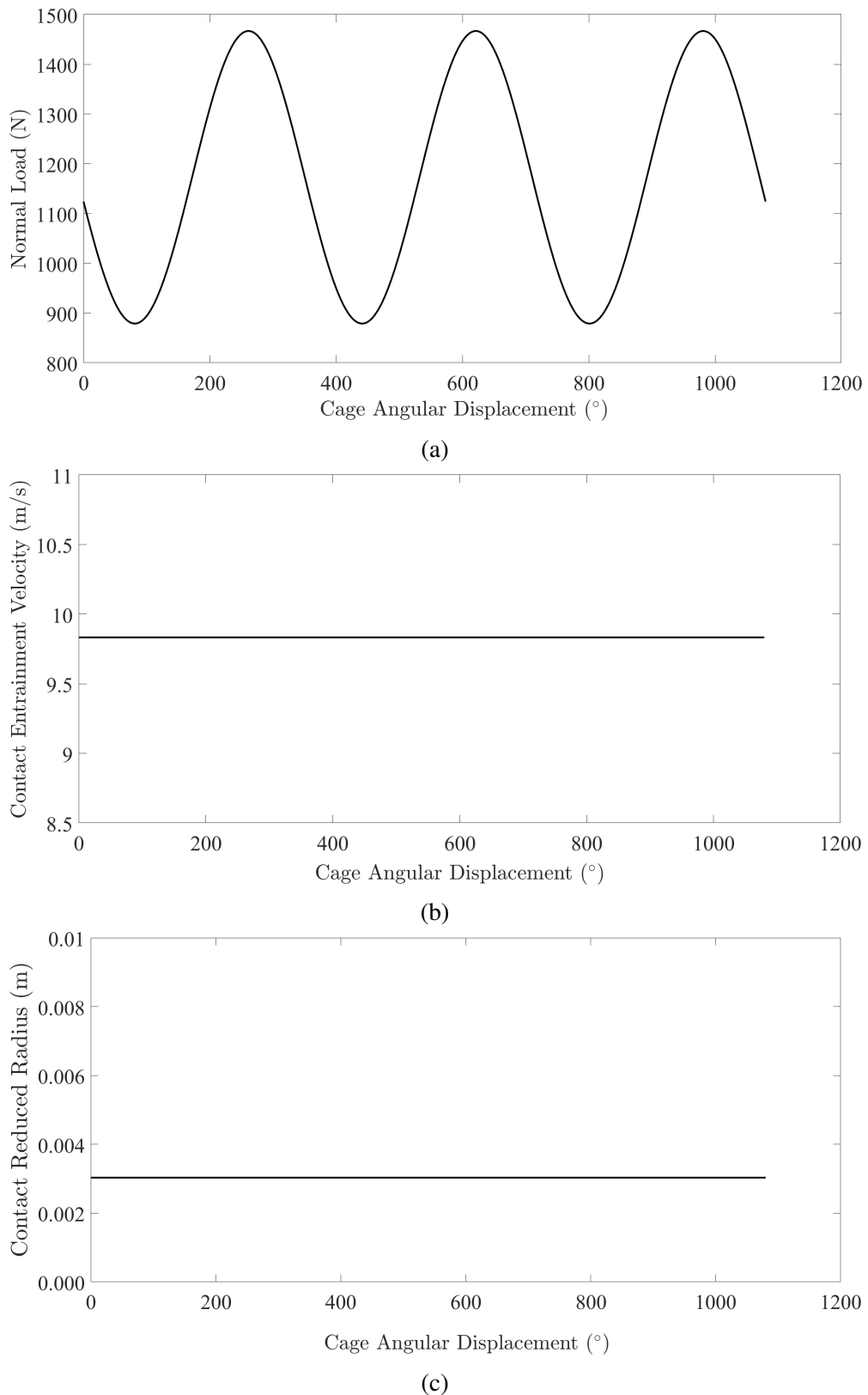


Figure 5.2 Individual rolling element input values to ANN : a) Contact load, b) Contact entrainment velocity, c) Contact reduced radius

Table 5.4 R^2 performance of ANN structures using 600 data points and a LogSig activation function

Activation Function: LogSig												
R^2		Number of Neurons										
		10	11	12	13	14	15	16	17	18	19	20
Number of Layers	1	0.997	0.995	0.998	0.998	0.999	0.999	0.999	0.998	0.998	0.995	0.999
	2	0.999	0.999	0.999	0.997	1.000	0.996	0.998	0.998	0.997	0.997	0.995
	3	1.000	0.998	0.998	0.999	0.997	0.997	0.997	0.998	0.993	0.995	0.996
	4	0.997	0.999	0.997	0.997	0.999	0.998	0.993	0.989	0.989	0.975	0.990

Table 5.5 R^2 performance of ANN structures using 600 data points and a Tanh activation function

Activation Function: Tanh												
R^2		Number of Neurons										
		10	11	12	13	14	15	16	17	18	19	20
Number of Layers	1	0.998	0.999	0.995	0.998	0.998	0.994	0.998	0.999	0.998	0.998	0.998
	2	0.999	0.998	0.998	0.999	0.996	0.998	0.996	0.996	0.996	0.993	0.994
	3	0.999	0.992	0.996	0.995	0.992	0.989	0.989	0.985	0.994	0.970	0.984
	4	0.997	0.997	0.992	0.994	0.991	0.983	0.982	0.978	0.990	0.989	0.983

function. For each configuration, the values of R^2 (coefficient of determination) and the training completion time were carefully documented.

Tables 5.4-5.10 present the R^2 values obtained from 600 data points, considering different activation functions, number of layers, and neurons. Among the activation functions tested, the ReLU function consistently underperformed when compared to the logistic sigmoid and hyperbolic tangent functions across all network structures. It is important to acknowledge that there is a slight variability in the performance of the network with each new training session. However, it is worth noting that the optimum number of layers, similar to tribological applications of ANNs [101], was found to be between two and three.

Bearing Film Thickness Predictions

After identifying suitable data set size and ANN structure, the ANN could then be compared to the analytical (Eq. 4.11) and numerical (Section 3.2) methods of obtaining central film thickness at the roller-race contact. The operating conditions of the bearing were within the range of validity of the training data set. This is demonstrated in Figure

Table 5.6 R^2 performance of ANN structures using 600 data points and a Tanh activation function

Activation Function: ReLU												
R^2		Number of Neurons										
		10	11	12	13	14	15	16	17	18	19	20
Number of Layers	1	0.985	0.991	0.994	0.993	0.993	0.994	0.992	0.994	0.995	0.987	0.990
	2	0.993	0.996	0.995	0.993	0.992	0.984	0.989	0.993	0.992	0.993	0.992
	3	0.986	0.983	0.996	0.988	0.984	0.980	0.992	0.992	0.988	0.986	0.988
	4	0.981	0.990	0.975	0.928	0.951	0.986	0.985	0.986	0.986	0.982	0.985

Table 5.7 Training time of ANN structures with LogSig activation function and 600 data points

600 Data Points, Activation Function: LogSig												
Training Time [s]		Number of Neurons										
		10	11	12	13	14	15	16	17	18	19	20
Number of Layers	1	0.76	0.96	1.16	1.01	1.49	1.30	1.41	1.72	1.12	0.90	1.13
	2	1.01	2.93	1.94	1.43	1.88	1.80	1.56	1.80	1.33	2.51	1.77
	3	2.81	1.29	2.58	2.22	2.27	1.52	1.67	2.26	2.06	1.94	3.57
	4	1.64	5.97	2.21	2.79	6.70	2.66	4.36	2.51	2.76	2.61	2.90

Key
Time [s]
0.00
10.00
100.00
600.00

Table 5.8 Training time of ANN structures with LogSig activation function and 1000 data points

1000 Data Points, Activation Function: LogSig												
Training Time [s]		Number of Neurons										
		10	11	12	13	14	15	16	17	18	19	20
Number of Layers	1	1.00	1.10	1.36	1.11	1.89	2.20	2.09	1.01	1.58	2.83	1.10
	2	3.25	1.66	2.33	2.72	4.00	3.07	2.35	2.81	5.35	1.97	3.77
	3	2.74	6.35	4.76	5.58	4.17	2.36	4.88	7.56	7.18	6.55	5.18
	4	2.59	2.29	8.12	6.47	7.17	3.81	7.70	11.46	19.01	12.14	8.92

Key
Time [s]
0.00
10.00
100.00
600.00

Table 5.9 Training time of ANN structures with LogSig activation function and 2000 data points

2000 Data Points, Activation Function: LogSig												
Training Time [s]		Number of Neurons										
		10	11	12	13	14	15	16	17	18	19	20
Number of Layers	1	0.90	2.47	1.70	1.74	4.38	2.61	2.49	1.81	4.54	2.58	2.67
	2	6.06	7.19	10.66	13.38	6.20	6.54	6.76	14.61	16.32	7.86	20.32
	3	18.72	13.45	4.55	5.19	21.54	23.88	26.00	25.44	27.50	11.66	19.71
	4	11.49	18.79	16.06	6.69	41.55	30.72	28.04	67.86	14.78	62.17	57.13

Key
Time [s]
0.00
10.00
100.00
600.00

Table 5.10 Training time of ANN structures with LogSig activation function and 5000 data points

5000 Data Points, Activation Function: LogSig												
Training Time [s]		Number of Neurons										
		10	11	12	13	14	15	16	17	18	19	20
Number of Layers	1	1.74	4.06	3.12	3.24	3.82	3.78	2.11	11.73	3.45	14.25	12.07
	2	10.86	22.86	37.50	30.99	20.02	19.95	38.09	11.02	48.89	134.95	37.88
	3	14.53	33.38	34.62	116.81	61.86	57.12	140.49	124.75	228.28	71.22	85.55
	4	94.66	36.71	139.61	70.20	13.33	229.45	88.24	155.37	217.48	500.54	600.01

Key
Time [s]
0.00
10.00
100.00
600.00

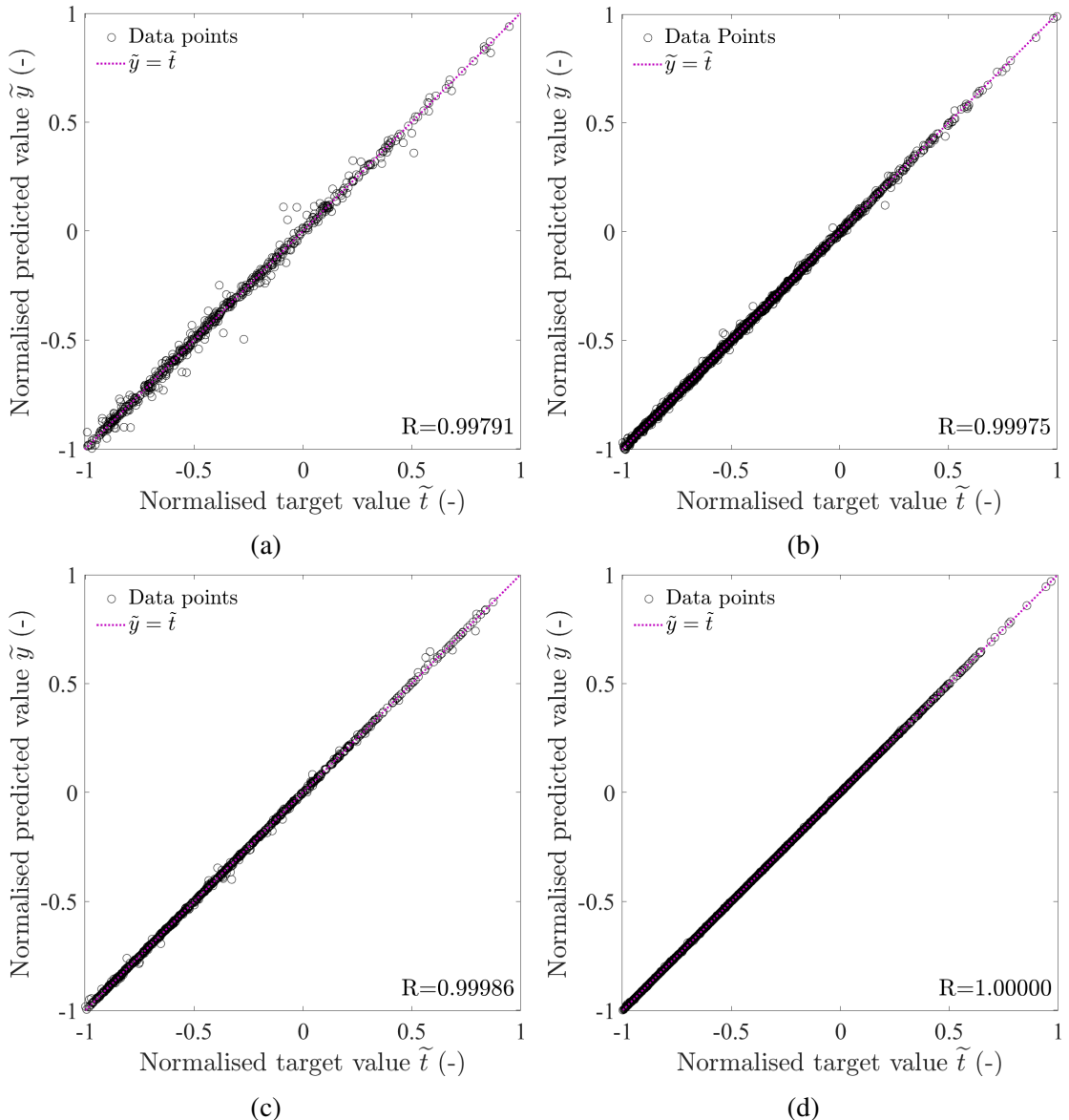


Figure 5.3 10 – $[14 - 14 - 14]_3 - 1$ using Hyperbolic Tangent activation function : a) 600 points, b) 1000 points, c) 2000 points, d) 5000 points

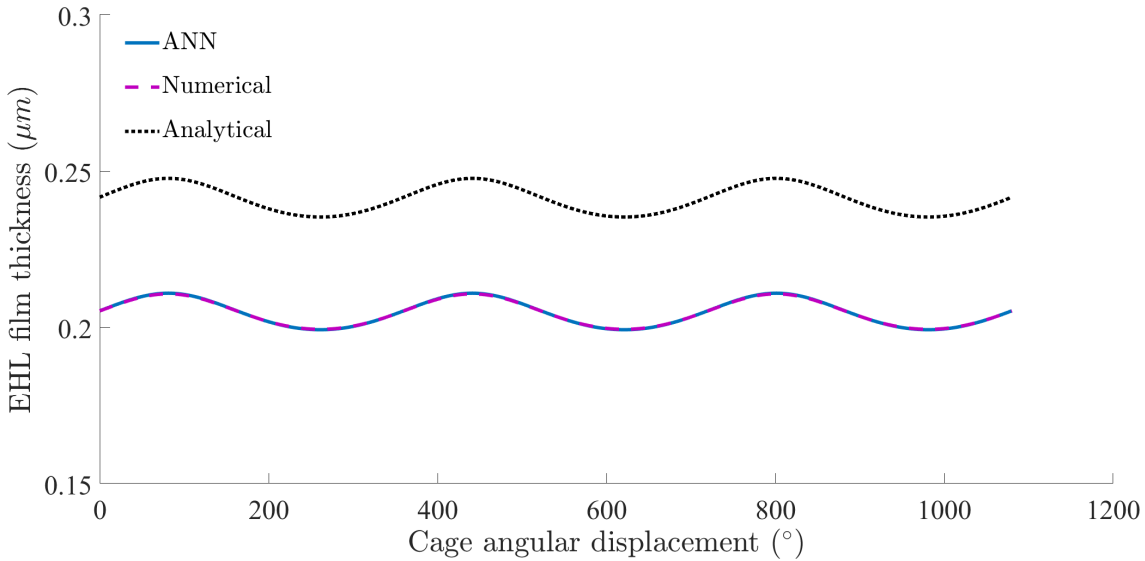


Figure 5.4 ANN, numerical and analytical central film thickness comparisons.

??hereby the Greenwood parameters for the bearing operating points are overlayed on the training cloud.

Figure

Three different methods of obtaining the EHL film thickness were tested

Method	Bearing	
	Time per point	MSE
	[s]	[μm]
Numerical	4.87E + 00	-
Analytical	4.43E - 05	1.32E - 3
ANN	3.33E - 03	1.46E - 8

5.6 Conclusions

5.7 Conclusions

Roller bearings are only one application of these ANNs. The use cases extend far beyond roller bearings, to key components in automotive, machining and other industrial applications where interactions between contiguous surfaces exist. Film thickness is a critical parameter in the determination of NVH, friction and wear.

Full numerical solution can account for film thickness profile and pressure distribution across the contact. Furthermore,

Echávarri et al. [83] comment on the "black box" nature of ANNs. Results from intermediate calculations are lost, which is often of interest for more in-depth analysis of contact condition; film thickness and pressure distributions and temperature for example.

Chapter 6

Implicit Bearing EHL Film Thickness Predictions Using an Artificial Neural Network at System Level

Refer to literature that suggests inclusion of ANN in multibody dynamics (Marian, Walker)

- Explain findings of previous chapter
- Different viscosities and operating points
- Higher speeds
- Comparisons with analytical equations
- Operating points to test:
 - 21 000 rpm
 - low viscosity
 - difference in stiffness
 - timing of each run for 2 cycles in steady state region
 - artificial damper in model to calm numerics?

Chapter 7

Conclusions

References

- [1] M. Marian, J. Mursak, M. Bartz, F. J. Profito, A. Rosenkranz, and S. Wartzack, “Predicting ehl film thickness parameters by machine learning approaches,” *Friction*, 6 2022. [Online]. Available: <https://link.springer.com/10.1007/s40544-022-0641-6>
- [2] X. Mosquet, H. Zablit, A. Dinger, G. Xu, M. Andersen, and K. Tominaga, “The electric car tipping point,” pp. 1–22, 2018.
- [3] J. A. Wensing, “The dynamics of ball bearings,” *Wear*, vol. 19, p. 360, 3 1972. [Online]. Available: <https://linkinghub.elsevier.com/retrieve/pii/0043164872901652>
- [4] O. Reynolds, “On the theory of lubrication and its application to mr. lowe’s experiments,” *Philosophical Transactions of the Royal Society of London*, vol. 177, pp. 157–234, 1886. [Online]. Available: https://scholar.google.com/scholar?q=related:zTMHxIMaYncJ:scholar.google.com/&hl=en&as_sdt=0,39&as_ylo=1886&as_yhi=1886#0
- [5] R. Gohar, *Elastohydrodynamics*. Imperial College Press, 1988.
- [6] K. A. Hoffmann and S. T. Chiang, *Computational Fluid Dynamics*, 4th ed. Engineering Education System, 2000.
- [7] R. Stribeck, “Ball bearings for various loads,” *Trans. ASME*, vol. 29, pp. 420–463, 1907.
- [8] G. Lundberg and A. Palmgren, “Dynamic capacity of roller bearings,” *Acta Polytechnica; Mechanical Engineering Series, Royal Swedish Academy of Engineering Sciences*, vol. 2, pp. 96–127, 1952.
- [9] A. Palmgren, “Ball and roller bearing engineering,” 1959.

- [10] A. B. Jones, “A general theory for elastically constrained ball and radial roller bearings under arbitrary load and speed conditions,” *Journal of Fluids Engineering, Transactions of the ASME*, vol. 82, pp. 309–320, 1960.
- [11] T. Harris, *Roller Bearing Analysis*, 3rd ed. John Wiley and Sons, 1984.
- [12] H. Sjovall, “The load distribution within ball and roller bearings under given external radial and axial load,” *Teknisk Tidskrift, Mek.*, vol. 9, 1933.
- [13] J. Rumbarger, “Thurst bearings with eccentric loads,” *Mach des.*, pp. 172–179, 1962.
- [14] S. Andréason, “Load distribution in a taper roller bearing arrangement considering misalignment,” *Tribology*, vol. 6, pp. 84–92, 6 1973. [Online]. Available: <https://linkinghub.elsevier.com/retrieve/pii/0041267873902418>
- [15] J. Y. Liu, “Analysis of tapered roller bearings considering high speed and combined loading.” *American Society of Mechanical Engineers (Paper)*, pp. 564–572, 1976.
- [16] J. M. de Mul, J. M. Vree, and D. A. Maas, “Equilibrium and associated load distribution in ball and roller bearings loaded in five degrees of freedom while neglecting friction—part ii: Application to roller bearings and experimental verification,” *Journal of Tribology*, vol. 111, pp. 149–155, 1 1989. [Online]. Available: <https://asmedigitalcollection.asme.org/tribology/article/111/1/149/432349/Equilibrium-and-Associated-Load-Distribution-in>
- [17] B. R. Jorgensen and Y. C. Shin, “Dynamics of machine tool spindle/bearing systems under thermal growth,” *Journal of Tribology*, vol. 119, pp. 875–882, 1997.
- [18] ———, “Dynamics of spindle-bearing systems at high speeds including cutting load effects,” *Journal of Manufacturing Science and Engineering, Transactions of the ASME*, vol. 120, pp. 387–394, 1998.
- [19] S. Kabus, M. R. Hansen, and O. Mouritsen, “A new quasi-static cylindrical roller bearing model to accurately consider non-hertzian contact pressure in time domain simulations,” *Journal of Tribology*, vol. 134, pp. 1–10, 2012.
- [20] R. Teutsch and B. Sauer, “An alternative slicing technique to consider pressure concentrations in non-hertzian line contacts,” *Journal of Tribology*, vol. 126, pp. 436–442, 2004.

- [21] T. A. Harris and M. N. Kotzalas, *Essential Concepts of Bearing Technology*, 5th ed. Taylor and Francis Group, 2007.
- [22] L. D. Meyer, F. F. Ahlgren, and B. Weichbrodt, “An analytic model for ball bearing vibrations to predict vibration response to distributed defects,” *Journal of Mechanical Design*, vol. 102, pp. 205–210, 4 1980. [Online]. Available: <https://asmedigitalcollection.asme.org/mechanicaldesign/article/102/2/205/430940/An-Analytic-Model-for-Ball-Bearing-Vibrations-to>
- [23] M. Matsubara, H. Rahnejat, and R. Gohar, “Computational modelling of precision spindles supported by ball bearings,” *International Journal of Machine Tools and Manufacture*, vol. 28, pp. 429–442, 1988. [Online]. Available: [http://dx.doi.org/10.1016/0890-6955\(88\)90056-9](http://dx.doi.org/10.1016/0890-6955(88)90056-9)
- [24] F. Wang, M. Jing, J. Yi, G. Dong, H. Liu, and B. Ji, “Dynamic modelling for vibration analysis of a cylindrical roller bearing due to localized defects on raceways,” *Proceedings of the Institution of Mechanical Engineers, Part K: Journal of Multi-body Dynamics*, vol. 229, pp. 39–64, 2015.
- [25] J. Liu, Z. Shi, and Y. Shao, “An analytical model to predict vibrations of a cylindrical roller bearing with a localized surface defect,” *Nonlinear Dynamics*, vol. 89, pp. 2085–2102, 2017.
- [26] Y. Guo and J. Keller, “Validation of combined analytical methods to predict slip in cylindrical roller bearings,” *Tribology International*, vol. 148, p. 106347, 2020. [Online]. Available: <https://doi.org/10.1016/j.triboint.2020.106347>
- [27] A. N. Grubin, *Fundamentals of the Hydrodynamic Theory of Lubrication of Heavily Loaded Cylindrical Surfaces*, book no. 3 ed. Central Scientific Research Institute for Technology and Mechanical Engineering, 1949.
- [28] M. Mohammadpour, P. Johns-Rahnejat, and H. Rahnejat, “Roller bearing dynamics under transient thermal-mixed non-newtonian elastohydrodynamic regime of lubrication,” *Proceedings of the Institution of Mechanical Engineers, Part K: Journal of Multi-body Dynamics*, vol. 229, pp. 407–423, 12 2015. [Online]. Available: <https://doi.org/10.1177/1464419315569621http://journals.sagepub.com/doi/10.1177/1464419315569621>
- [29] M. Denni, N. Biboulet, V. Abousleiman, and A. A. Lubrecht, “Dynamic study of a roller bearing in a planetary application considering the hydrodynamic

- lubrication of the roller/cage contact,” *Tribology International*, vol. 149, p. 105696, 2019. [Online]. Available: <https://doi.org/10.1016/j.triboint.2019.03.054>
- [30] P. K. Gupta, “Dynamics of rolling-element bearings—part i: Cylindrical roller bearing analysis,” *Journal of Lubrication Technology*, vol. 101, pp. 293–302, 7 1979. [Online]. Available: <https://asmedigitalcollection.asme.org/tribology/article/101/3/305/410221/Dynamics-of-RollingElement-BearingsPart-IIhttps://asmedigitalcollection.asme.org/tribology/article/101/3/293/410262/Dynamics-of-RollingElement-BearingsPart-I>
- [31] D. W. Daring and K. L. Johnson, “Fluid film damping of rolling contact vibrations,” *Journal of Mechanical Engineering Science*, vol. 17, pp. 214–218, 8 1975. [Online]. Available: http://journals.sagepub.com/doi/10.1243/JMES_JOUR_1975_017_031_02
- [32] H. Mehdigoli, H. Rahnejat, and R. Gohar, “Vibration response of wavy surfaced disc in elastohydrodynamic rolling contact,” *Wear*, vol. 139, pp. 1–15, 1990.
- [33] J. Walker, H. Questa, S. R. Bewsher, C. Schweiger, and M. Sopouch, “Experimental design for characterization of force transmissibility through bearings in electric machines and transmissions,” 2018, pp. 1–6.
- [34] R. Takeda, G. Lisco, T. Fujisawa, L. Gastaldi, H. Tohyama, and S. Tadano, “Drift removal for improving the accuracy of gait parameters using wearable sensor systems,” *Sensors*, vol. 14, pp. 23 230–23 247, 12 2014. [Online]. Available: <http://www.mdpi.com/1424-8220/14/12/23230>
- [35] B. J. Hamrock and D. Dowson, *Ball Bearing Lubrication: The Elastohydrodynamics of Elliptical Contacts*. John Wiley and Sons, 1981.
- [36] H. Rahnejat, “Influence of vibration on the oil film in concentrated contacts,” 1984.
- [37] D. Dowson and S. Toyoda, “A central film thickness formula for elastohydrodynamic line,” *Proceedings of the Fifth Leeds-Lyon Symposium on Tribology, Mechanical Engineering Publications*, pp. 60–65, 1979.
- [38] J. A. Greenwood and J. H. Tripp, “The contact of two nominally flat rough surfaces,” *Proceedings of the Institution of Mechanical Engineers*, vol. 185, pp. 625–633, 1970.

- [39] C. R. Evans and K. L. Johnson, “Regimes of traction in elastohydrodynamic lubrication,” *Proceedings of the Institution of Mechanical Engineers, Part C: Journal of Mechanical Engineering Science*, vol. 200, p. 313–324, 1986.
- [40] C. Barus, “Isothermals isopietics and isometrics in relationship to viscosity,” *American Journal of Science 3rd Series*, vol. 45, pp. 87–96, 1893.
- [41] R. Gohar and H. Rahnejat, *Fundamentals of Tribology*, 3rd ed. World Scientific Publishing Europe Ltd., 2019.
- [42] C. Roelands, “Correlational aspects of the viscosity-temperature-pressure relationship of lubricating oils,” 1966.
- [43] L. Houpert, “New results of traction force calculations in elastohydrodynamic contacts.” vol. 107, pp. 241–245, 1984.
- [44] D. Dowson and G. Higginson, *Elasto-hydrodynamic lubrication*, si ed. Pergamon Press, 1977.
- [45] R. F. Crouch and A. Cameron, “Viscosity-temperature equations for lubricants,” *J. Inst. Petroleum*, vol. 47, pp. 307–313, 1961.
- [46] H. Okamura, *A contribution to the numerical analysis of isothermal elastohydrodynamic lubrication*. Elsevier, 1983, pp. 313–320.
- [47] M. Masjedi and M. M. Khonsari, “Film thickness and asperity load formulas for line-contact elastohydrodynamic lubrication with provision for surface roughness,” *Journal of Tribology*, vol. 134, 1 2012. [Online]. Available: <https://asmedigitalcollection.asme.org/tribology/article/doi/10.1115/1.4005514/439343/Film-Thickness-and-Asperity-Load-Formulas-for>
- [48] R. G. Budynas and J. K. Nisbett, *Shigley’s Mechanical Engineering Design*, 9th ed. McGraw-Hill, 2011.
- [49] B. J. Hamrock, “Film thickness for different regimes of fluid-film lubrication,” pp. 1–14, 1980.
- [50] W. Cai, X. Wu, M. Zhou, Y. Liang, and Y. Wang, “Review and development of electric motor systems and electric powertrains for new energy vehicles,” *Automotive Innovation*, vol. 4, pp. 3–22, 2021. [Online]. Available: <https://doi.org/10.1007/s42154-021-00139-z>

- [51] J. M. de Mul, J. M. Vree, and D. A. Maas, “Equilibrium and associated load distribution in ball and roller bearings loaded in five degrees of freedom while neglecting friction—part i: General theory and application to ball bearings,” *Journal of Tribology*, vol. 111, pp. 142–148, 1 1989. [Online]. Available: <https://asmedigitalcollection.asme.org/tribology/article/111/1/142/432329/Equilibrium-and-Associated-Load-Distribution-in>
- [52] C. T. Walters, “The dynamics of ball bearings,” *Journal of Tribology*, vol. 93, pp. 1–10, 1971.
- [53] C. S. Sunnersjö, “Varying compliance vibrations of rolling bearings,” *Journal of Sound and Vibration*, vol. 58, pp. 363–373, 1978.
- [54] H. Rahnejat and S. Rothberg, *Mulit-body dynamics: Monitoring and simulation techniques III*, 1st ed. Wiley, 2004.
- [55] H. Questa, M. Mohammadpour, S. Theodossiades, C. Garner, S. Bewsher, and G. Offner, “Tribo-dynamic analysis of high-speed roller bearings for electrified vehicle powertrains,” *Tribology International*, vol. 154, p. 106675, 2 2021. [Online]. Available: <https://linkinghub.elsevier.com/retrieve/pii/S0301679X20305004>
- [56] B. J. Stone, “The state of the art in the measurement of the stiffness and damping of rolling element bearings,” *CIRP Annals - Manufacturing Technology*, vol. 31, pp. 529–538, 1982.
- [57] P. Dietl, “Damping and stiffness characteristics of rolling element bearings-theory and experiment,” 1997.
- [58] L. Bizarre, F. Nonato, and K. Cavalca, “Formulation of five degrees of freedom ball bearing model accounting for the nonlinear stiffness and damping of elastohydrodynamic point contacts,” *Mechanism and Machine Theory*, vol. 124, pp. 179–196, 6 2018. [Online]. Available: <https://linkinghub.elsevier.com/retrieve/pii/S0094114X1830106X>
- [59] H. Rahnejat and R. Gohar, “The vibrations of radial ball bearings,” *Proceedings of the Institution of Mechanical Engineers, Part C: Journal of Mechanical Engineering Science*, vol. 199, pp. 181–193, 1985.
- [60] R. Aini, H. Rahnejat, and R. Gohar, “Vibration modeling of rotating spindles supported by lubricated bearings,” *Journal of Tribology*, vol. 124, pp. 158–165, 2002.

- [61] J. Sopanen and A. Mikkola, “Dynamic model of a deep-groove ball bearing including localized and distributed defects. part 1: Theory,” *Proceedings of the Institution of Mechanical Engineers, Part K: Journal of Multi-body Dynamics*, vol. 217, pp. 201–211, 9 2003. [Online]. Available: <http://journals.sagepub.com/doi/10.1243/14644190360713551>
- [62] ——, “Dynamic model of a deep-groove ball bearing including localized and distributed defects. part 2: Implementation and results,” *Proceedings of the Institution of Mechanical Engineers, Part K: Journal of Multi-body Dynamics*, vol. 217, pp. 213–223, 9 2003. [Online]. Available: <http://journals.sagepub.com/doi/10.1243/14644190360713560>
- [63] N. Sawalhi and R. B. Randall, “Simulating gear and bearing interactions in the presence of faults. part i. the combined gear bearing dynamic model and the simulation of localised bearing faults,” *Mechanical Systems and Signal Processing*, vol. 22, pp. 1924–1951, 2008.
- [64] J. Liu and Y. Shao, “Vibration modelling of nonuniform surface waviness in a lubricated roller bearing,” *JVC/Journal of Vibration and Control*, vol. 23, pp. 1115–1132, 2017.
- [65] F. Nonato and K. L. Cavalca, “An approach for including the stiffness and damping of elastohydrodynamic point contacts in deep groove ball bearing equilibrium models,” *Journal of Sound and Vibration*, vol. 333, pp. 6960–6978, 2014. [Online]. Available: <http://dx.doi.org/10.1016/j.jsv.2014.08.011>
- [66] G. Lundberg and E. Yhland, “Cylinder compressed between two plane bodies,” *SKF*, 1949.
- [67] T. Parikyan, T. Resch, and H. H. Priebsch, “Structured model of crankshaft in the simulation of engine dynamics with avl/excite,” vol. 67. American Society of Mechanical Engineers, 9 2001, pp. 105–114. [Online]. Available: <https://asmedigitalcollection.asme.org/ICEF/proceedings/ICEF2001/80159/105/1081821>
- [68] G. Offner, “Modelling of condensed flexible bodies considering non-linear inertia effects resulting from gross motions,” *Proceedings of the Institution of Mechanical Engineers, Part K: Journal of Multi-body Dynamics*, vol. 225, pp. 204–219, 2011.
- [69] T. L. H. Walford and B. J. Stone, “The sources of damping in rolling element bearings under oscillating conditions,” *Proceedings of*

- the Institution of Mechanical Engineers, Part C: Journal of Mechanical Engineering Science*, vol. 197, pp. 225–232, 10 1983. [Online]. Available: http://journals.sagepub.com/doi/10.1243/PIME_PROC_1983_197_102_02
- [70] D. Nelia, I. Bercea, and V. Paleu, “Prediction of roller skewing in tapered roller bearings,” *Tribology Transactions*, vol. 51, pp. 128–139, 2008.
- [71] F. Majdoub, L. Saunier, C. Sidoroff-coicaud, and B. Mevel, “Tribology international experimental and numerical roller skew in tapered roller bearings,” *Tribology International*, vol. 145, p. 106142, 2020. [Online]. Available: <https://doi.org/10.1016/j.triboint.2019.106142>
- [72] B. Mevel and J. L. Guyader, “Routes to chaos in ball bearings,” pp. 471–487, 1993.
- [73] H. Spikes, “Basics of ehl for practical application,” *Lubrication Science*, vol. 27, pp. 45–67, 2015.
- [74] X. Shi and L. Wang, “Tehl analysis of high-speed and heavy-load roller bearing with quasi-dynamic characteristics,” *Chinese Journal of Aeronautics*, vol. 28, pp. 1296–1304, 8 2015. [Online]. Available: <http://dx.doi.org/10.1016/j.cja.2015.06.013>
<https://linkinghub.elsevier.com/retrieve/pii/S1000936115001181>
- [75] K. P. Singh and B. Paul, “Numerical solution of non-hertzian elastic contact problems,” *Journal of Applied Mechanics*, vol. 41, pp. 484–490, 6 1974. [Online]. Available: <https://asmedigitalcollection.asme.org/appliedmechanics/article/41/2/484/422784/Numerical-Solution-of-NonHertzian-Elastic-Contact>
- [76] T. A. Harris and M. N. Kotzales, *Advanced Concepts of Bearing Technology*, 5th ed. Taylor and Francis Group, 2007.
- [77] J. M. de Mul, J. J. Kalker, and B. Fredriksson, “The contact between arbitrarily curved bodies of finite dimensions,” *Journal of Tribology*, vol. 108, pp. 140–148, 1 1986. [Online]. Available: <https://asmedigitalcollection.asme.org/tribology/article/108/1/140/418690/The-Contact-Between-Arbitrarily-Curved-Bodies-of>
- [78] Y. Mitsuya, H. Sawai, M. Shimizu, and Y. Aono, “Damping in vibration transfer through deep-groove ball bearings,” *Transactions of the Japan Society of Mechanical Engineers Series C*, vol. 58, pp. 3714–3721, 1992.
- [79] E. Krämer, *Dynamics of Rotors and Foundations*. Springer Berlin Heidelberg, 1993. [Online]. Available: <http://link.springer.com/10.1007/978-3-662-02798-1>

- [80] D. Dowson and G. R. Higginson, “A numerical solution to the elasto-hydrodynamic problem,” *Journal of Mechanical Engineering Science*, vol. 1, pp. 6–15, 1959.
- [81] R. Gohar and H. Rahnejat, *Fundamentals of Tribology*. WORLD SCIENTIFIC (EUROPE), 9 2018. [Online]. Available: <https://www.worldscientific.com/worldscibooks/10.1142/q0152>
- [82] D. Dowson, “Paper 10: Elastohydrodynamics,” *Proceedings of the Institution of Mechanical Engineers, Conference Proceedings*, 1967.
- [83] J. E. Otero, E. de la Guerra Ochoa, E. C. Tanarro, P. L. Morgado, A. D. Lantada, J. M. Munoz-Guijosa, and J. L. M. Sanz, “Artificial neural network approach to predict the lubricated friction coefficient,” *Lubrication Science*, vol. 26, pp. 141–162, 4 2014. [Online]. Available: <https://onlinelibrary.wiley.com/doi/10.1002/ls.1238>
- [84] I. Argatov, “Artificial neural networks (anns) as a novel modeling technique in tribology,” *Frontiers in Mechanical Engineering*, vol. 5, pp. 1–9, 2019.
- [85] E. O. Ezugwu, S. J. Arthur, and E. L. Hines, “Tool-wear prediction using artificial neural networks,” *Journal of Materials Processing Tech.*, vol. 49, pp. 255–264, 1995.
- [86] K. L. Rutherford, P. W. Hatto, C. Davies, and I. M. Hutchings, “Abrasive wear resistance of tin/nbn multi-layers: Measurement and neural network modelling,” *Surface and Coatings Technology*, vol. 86-87, pp. 472–479, 1996.
- [87] S. P. Jones, R. Jansen, and R. L. Fusaro, “Preliminary investigation of neural network techniques to predict tribological properties,” *Tribology Transactions*, vol. 40, pp. 312–320, 1997.
- [88] K. Genel, S. C. Kurnaz, and M. Durman, “Modeling of tribological properties of alumina fiber reinforced zinc-aluminum composites using artificial neural network,” *Materials Science and Engineering A*, vol. 363, pp. 203–210, 2003.
- [89] M. Hayajneh, A. M. Hassan, A. Alrashdan, and A. T. Mayyas, “Prediction of tribological behavior of aluminum-copper based composite using artificial neural network,” *Journal of Alloys and Compounds*, vol. 470, pp. 584–588, 2009.
- [90] Z. Zhang, K. Friedrich, and K. Velten, “Prediction on tribological properties of short fibre composites using artificial neural networks,” *Wear*, vol. 252, pp. 668–675, 2002.

- [91] L. Cavaleri, P. G. Asteris, P. P. Psyllaki, M. G. Douvika, A. D. Skentou, and N. M. Vaxevanidis, “Prediction of surface treatment effects on the tribological performance of tool steels using artificial neural networks,” *Applied Sciences (Switzerland)*, vol. 9, 2019.
- [92] S. Bhaumik, S. D. Pathak, S. Dey, and S. Datta, “Artificial intelligence based design of multiple friction modifiers dispersed castor oil and evaluating its tribological properties,” *Tribology International*, vol. 140, p. 105813, 2019.
- [93] M. Afrand, K. N. Najafabadi, N. Sina, M. R. Safaei, A. Kherbeet, S. Wongwises, and M. Dahari, “Prediction of dynamic viscosity of a hybrid nano-lubricant by an optimal artificial neural network,” *International Communications in Heat and Mass Transfer*, vol. 76, pp. 209–214, 8 2016. [Online]. Available: <https://linkinghub.elsevier.com/retrieve/pii/S0735193316301610>
- [94] M. H. Esfe, H. Rostamian, S. Esfandeh, and M. Afrand, “Modeling and prediction of rheological behavior of al₂o₃-mwcnt/5w50 hybrid nano-lubricant by artificial neural network using experimental data,” *Physica A: Statistical Mechanics and its Applications*, vol. 510, pp. 625–634, 2018.
- [95] M. Ripa and L. Frangu, “A survey of artificial neural networks applications in wear and manufacturing processes,” *Journal of Tribology*, pp. 35–42, 2004.
- [96] S. Panda, D. Chakraborty, and S. Pal, “Flank wear prediction in drilling using back propagation neural network and radial basis function network,” *Applied Soft Computing*, vol. 8, pp. 858–871, 3 2008. [Online]. Available: <https://linkinghub.elsevier.com/retrieve/pii/S1568494607000762>
- [97] I. Asiltürk and M. Çunkaş, “Modeling and prediction of surface roughness in turning operations using artificial neural network and multiple regression method,” *Expert Systems with Applications*, vol. 38, pp. 5826–5832, 2011.
- [98] J. G. A. Barbedo, “Impact of dataset size and variety on the effectiveness of deep learning and transfer learning for plant disease classification,” *Computers and Electronics in Agriculture*, vol. 153, pp. 46–53, 10 2018. [Online]. Available: <https://linkinghub.elsevier.com/retrieve/pii/S0168169918304617>
- [99] N. Wang and C. M. Tsai, “Assessment of artificial neural network for thermohydrodynamic lubrication analysis,” *Industrial Lubrication and Tribology*, vol. 72, pp. 1233–1238, 2020.

- [100] A. Almqvist, “Fundamentals of physics-informed neural networks applied to solve the reynolds boundary value problem,” *Lubricants*, vol. 9, p. 82, 8 2021. [Online]. Available: <https://www.mdpi.com/2075-4442/9/8/82>
- [101] M. Marian and S. Tremmel, “Current trends and applications of machine learning in tribology—a review,” *Lubricants*, vol. 9, p. 86, 9 2021. [Online]. Available: <https://www.mdpi.com/2075-4442/9/9/86>
- [102] K. Siebertz, T. Hochkirchen, and D. van Bebber, *Statistische versuchsplanung*. Springer, 2010.
- [103] M. E. Johnson, L. M. Moore, and D. Ylvisaker, “Minimax and maximin distance designs,” pp. 131–148, 1990.
- [104] K. L. Johnson, “Regimes of elastohydrodynamic lubrication,” *Journal of Mechanical Engineering Science*, vol. 12, pp. 9–16, 2 1970. [Online]. Available: http://journals.sagepub.com/doi/10.1243/JMES_JOUR_1970_012_004_02
- [105] J. Han and C. Moraga, *The influence of the sigmoid function parameters on the speed of backpropagation learning*, 1995, pp. 195–201. [Online]. Available: http://link.springer.com/10.1007/3-540-59497-3_175
- [106] S. Sharma, S. Sharma, and A. Athaiya, “Activation functions in neural networks,” *International Journal of Engineering Applied Sciences and Technology*, vol. 4, pp. 310–316, 2020. [Online]. Available: <http://www.ijeast.com>

Appendix A

MFEIT Reconstruction Images